The following changes were made to the manuscript after the original submission.

On page 78 after equation (4.20) replace the paragraph with the following text

At the NATRE site k was of the order of 100 m^{-1} implying that vertical velocities were of the order of $w' = 10^{-4}$ m s^{-1}. Inertial waves provide the dominant shear in the ocean but as these waves have a corkscrew velocity profile,with shear magnitude invariant in depth and time, they will not cause any flux divergence. A spatially varying shear can also be produced by intrusions from collapsing turbulent events and internal waves. Measurements of finestructure at the NATRE site by Polzin *et al.* (2001) found that both turbulent patches and internal waves had typical vertical wavelengths of D = 1-10 m. After a turbulent event, partially mixed patches collapse with a Richardson number of the order of 1, implying that the maximum shear is $\Delta U/D = N$. Typical values of N at the NATRE site were of the order of $N = 10^{-5}$ s^{-1}, so that maximum horizontal velocities of the collapsing patches would be of the order of $\Delta U = 10^{-4} - 10^{-5}$ m s^{-1}. If we assume that the maximum shear in internal waves also occurs when $Ri \approx 1$ then the maximum horizontal velocities will be the same as those due to collapsing turbulent patches. The ratio of maximum horizontal velocities to maximum vertical fingervelocities is then of order Θ = 0.1–1, which from figure4.1 implies that $0.1 < f(\Theta) < 0.25$. The timescale for the formation of significantdensity structure by (4.17) is then of the order of Δt = $10^3 - 10^4$ s, when either collapsing turbulent patches or internal waves are driving a spatially varying shear.

On page 86 equation 5.8 should be corrected to the following.

$$R_{\rho\ initial} \leq \frac{1-\gamma M}{1-M}.$$

Convection, turbulent mixing and salt fingers

Mathew Graeme Wells

A thesis submitted for the degree of

Doctor of Philosophy at

The Australian National University

March 2001

Typeset in Times by TEX and LATEX 2ε.

Except where otherwise indicated, this thesis is my own original work.

Mathew Graeme Wells

16 March 2001

I would like to thank my supervisor Ross Griffiths, and my advisors Graham Hughes, John Taylor and Stewart Turner for their advice and guidance throughout this study. It was a pleasure to collaborate with Brad Sherman and I learnt a lot about trying to transfer ideas from the lab to the ”real world”. Andrew Kiss, Ross Kerr and David Osmond also contributed by always being available to listen and comment to many ideas I had. Tony Beasley, Derek Corrigan and Ross Wylde-Brown provided a great deal of technical assistance in the laboratory.

I would also like to thank Ann Gargett, Greg Ivey, Eric Kunze, Paul Linden, Trevor McDougall, Bill Merryfield, Francesco Papperella, Ray Schmitt and Colin Shen for useful conversations and correspondence during the last 3 years.

Finally a big thank you to my family, flatmates and friends for their love and support.

Abstract

In this thesis I address several topics concerning the interaction of convection and density stratification in oceans and lakes. I present experimental and theoretical investigations of the interaction between a localized buoyancy source and a heat flux through a horizontal boundary, and of the interactions between salt fingers and intermittent turbulence or shear.

An extensive series of laboratory experiments were used to quantify the stratification and circulation that result from the combined presence of a localized buoyancy source and a heat flux through a horizontal boundary. Previous studies found that convection in the form of a turbulent buoyant plume tends to produce a stable density stratification, whereas the distributed flux from a horizontal boundary tends to force vigorous overturning and to produce well-mixed layers. A new result of this thesis is that a steady density profile, consisting of a mixed layer and a stratified layer, can exist when the plume buoyancy flux is greater than the distributed flux. When the two fluxes originate from the same boundary, the steady state involves a balance between the rate at which the mixed layer deepens due to entrainment on the one hand and vertical advection of the stratified water far from the plume (due to the volume flux acquired by entrainment) on the other hand. There is a monotonic relationship between the normalized mixed layer depth and flux ratio R (boundary flux/plume flux) for $0 < R < 1$, and the whole tank overturns for $R > 1$. The stable density gradient in the stratified region is primarily due to the buoyancy from the plume and for $R > 0$ there is a small increase in the gradient due to entrainment of buoyancy from the mixed layer. For the case of fluxes from a plume located at one boundary and a uniform heat flux from the opposite boundary the shape of the density profile is that given by Baines & Turner (1969), with the gradient reduced by a factor $(1+R)$ due to the heating. Thus, when $R < -1$ there is no stratified region and the whole water column overturns. When $0 > R > -1$, the constant depth of the convecting layer is determined by the Monin-Obukhov scale in the outflow from the plume.

One application of these laboratory experiments is to surface cooling in lakes and reservoirs that have shallow sidearms. During prolonged periods of atmospheric cooling, gravity

currents can form in these sidearms and as the currents descend into the deeper waters they are analogous to isolated plumes. This can result in stratification at the base of a lake and an upwelling of cold water. Away from the shallow regions, surface cooling leads to a mixed surface layer. The depth of this layer will be steady when the rate of upwelling balances the rate at which the mixed layer deepens by turbulent entrainment. A series of laboratory experiments designed to model the depth distribution of a lake with a shallow sidearm showed that the steady depth of the mixed layer depended on the ratio of the area of the shallow region to the area of the deep region. Significant stratification resulted only when the reservoir had shallow regions that account for more than 50 % of the surface area. The depth of the surface mixed layer also depended on the ratio of the depths of the shallow and deep regions and no significant stratification forms if this ratio is greater than 0.5. These results are in good agreement with observations of circulation and stratification during long periods of winter cooling from Chaffey reservoir, Australia. Theoretical time scales are also developed to predict the minimum duration of atmospheric cooling that can lead the development of stratification.

In the second part of this thesis, I report a series of laboratory experiments which are designed to investigate the fine structure and buoyancy fluxes that result from salt finger convection in the presence of shear and intermittent turbulence. We find that, when salt finger convection in deep linear gradients is superposed with a depth-dependent spatially periodic shear, variations in the density profile develop on the same wavelength as the shear. The laboratory experiments presented in this thesis were carried out in a continuous density gradient with a spatially periodic shear produced by exciting a low-frequency baroclinic mode of vertical wavelength 60 mm. The density gradient consisted of opposing salt and sugar gradients favourable to salt fingers (an analogue to the oceanic heat/salt system). Where the shearing was large the salt finger buoyancy fluxes were small. Changes in salinity gradient due to the resulting flux divergence were self-amplifying until a steady state was reached in which the spatial variations in the ratio of salt and sugar gradients were such that the flux divergence vanished. Thus, along with reducing the mean salt finger buoyancy flux, a spatially varying shear can also lead to the formation of density structure.

In the ocean intermittent turbulence can occur in isolated patches in salt finger-favourable regions. I present new results from laboratory experiments in which a partially mixed patch was produced in deep linear concentration gradients favourable to salt finger convection. Salt

fingers give rise to an "up gradient" flux of buoyancy which can reduce the density gradient in a partially mixed patch. This can then lead to overturning convection of the partially mixed patch if a) the ratio of T and S gradients, $R_\rho = \alpha T_z/\beta S_z$, is near one, b) if turbulence results in a nearly well-mixed patch and c) the patch thickness is large enough that convective eddies are able to transport T and S faster than salt fingers. Once overturning occurs, subsequent turbulent entrainment can lead to growth of the patch thickness. Experimental results agree well with the theoretical prediction that $h = \sqrt{-8\eta\, B/N^2\, t}$, where h is the patch thickness, t is time, η is the mixing efficiency of turbulent entrainment, B is the buoyancy flux of the salt fingers and N is the buoyancy frequency of the ambient gradient region. This thickening is in contrast to the collapse that a partially mixed patch would experience due to lateral intrusion in a very wide tank. In regions of the ocean that contain salt fingers there is the possibility that, after a period of initial collapse, an intrusion could enter a regime where the rate of collapse in the vertical is balanced by the growth rate due to turbulent entrainment from the salt fingers buoyancy flux, thus tending to maintain the rate of lateral spread.

A further series of laboratory experiments quantified the buoyancy fluxes that result from salt fingers and intermittent turbulence. A continuous density gradient, favourable to salt finger convection, was stirred intermittently by an array of vertical rods that move horizontally back and forth along the tank at a constant velocity. Previous experiments had found that continuous turbulence destroys any salt fingers present because the dissipation of turbulent kinetic energy occurs at scales that are generally smaller than salt fingers widths. However, when turbulence is present only intermittently, the salt fingers may have time to grow between turbulent events and so contribute to the vertical diffusivities of heat and salt. We conclude that the vertical buoyancy flux of salt fingers is strongly dependent upon the intermittency of the turbulence, and equilibrium fluxes are only achieved if the time between turbulent events is much greater than the *e*-folding time of the salt fingers. When these results are applied to an oceanographic setting, the effect of intermittent turbulence, occurring more 5% of the time, is to reduce the effective eddy diffusivity due to salt fingers below equilibrium salt finger values, so that at $R_\rho \gg 2$ the eddy diffusivity is due only to turbulence. The time averaged salt fingers fluxes are not significantly reduced by intermittent turbulence when $R_\rho < 2$ or if the intermittence occurs less than 2% of the time, and so may contribute significant diapycnal fluxes in many parts of the ocean.

Contents

List of Figures

Chapter 1

Introduction

The research in this thesis is aimed at understanding some of the important dynamics of convection and turbulent mixing that drive circulation in oceans and other water bodies. The oceans on the whole are stably stratified with warm, light waters overlying cold, dense waters at the bottom. Near the surface, exchanges of heat and freshwater with the atmosphere result in density differences which can drive convection between surface and bottom waters. In regions where there is strong localized cooling, dense surface water can sink to the abyssal plains and force a distributed upwelling in the rest of the ocean. In the sub-tropical regions, solar heating can result in hot, salty water overlying colder, fresher water. In this case *salt finger* convection can occur, which also results in a flux of buoyancy downwards. Turbulent mixing can also occur in the stable density gradients of the ocean from a variety of mechanisms such as flow over topography or interactions between internal waves. Detailed predictions of circulation in oceans and water bodies are sensitive to how these three mechanisms of vertical transport are parameterized, so it is important to understand how the different forms of convection and turbulence interact and under what conditions they will contribute buoyancy fluxes.

In this thesis two fundamental problems involving mixing and stratification in water bodies are addressed. The first concerns the stratification and circulation that result when both distributed and isolated sources of buoyancy are simultaneously applied to a confined volume. This problem is explored using theory and laboratory experiments, and the results are then applied to understand observations from a field study of stratification that developed in a water supply reservoir in response to winter cooling. The second problem addressed in this thesis is the interaction of salt finger convection with shear and intermittent turbulence. This problem is investigated using a series of laboratory experiments and the results have implications for the generation of oceanic fine-structure and for diapycnal fluxes in the thermocline.

In §1.1 we review previous laboratory and field observations on the circulation and stratification that result from distributed and isolated sources of buoyancy. In §1.2 the salt finger instability is introduced and previous theory, laboratory experiments and field observations are discussed. An overview of the experiments and theory in this thesis is presented in §1.3.

1.1 Competition between distributed and isolated sources of buoyancy

1.1.1 Stratification produced by plumes and surface heating in confined volumes

A destabilizing buoyancy flux distributed uniformly over the top or bottom horizontal boundary of a fluid layer drives turbulent convection in the layer when the Rayleigh number is large. The consequent convection maintains a nearly homogeneous layer. A localized source of buoyancy, on the other hand, produces a plume. Baines & Turner (1969) showed that a turbulent plume in a fluid volume of finite vertical and horizontal extent leads to the development of a stable density stratification. Hence if a layer is subjected to both a uniformly distributed boundary flux and an intense, localized flux, there is competition between the tendency for the uniform flux to overturn the layer and the tendency for the turbulent plume to stratify the system.

In a semi-enclosed sea, for example, the heat loss or evaporation from the surface may supply a buoyancy flux broadly over the surface, driving convection in a surface mixed layer. If the surface fluxes are more intense in a relatively small region, deep convection may occur, involving sinking and horizontal entrainment similar to that in the idealized turbulent plume from a small (or even point) source. Stratification may be established by the plume deep in the water column, while the surface flux maintains the upper convecting layer.

Baines & Turner (1969) have analyzed the case of a turbulent plume in detail. The plume rises through its surrounding fluid until it reaches the opposite boundary, where it spreads out in a layer of thickness h, as illustrated in figure 1.1. The first fluid in the plume to reach this boundary is lighter than the surroundings and forms a density step. As the plume flow continues, entrainment of surrounding fluid into the plume assures that the outflow continually

decreases in density while the density step, or "first front", is slowly displaced downward to asymptotically approach the level of the plume source. Thus the tank is slowly filled with a density gradient, the shape of which is controlled by the entrainment into the plume. The resulting density profile is illustrated in figure 1.2.

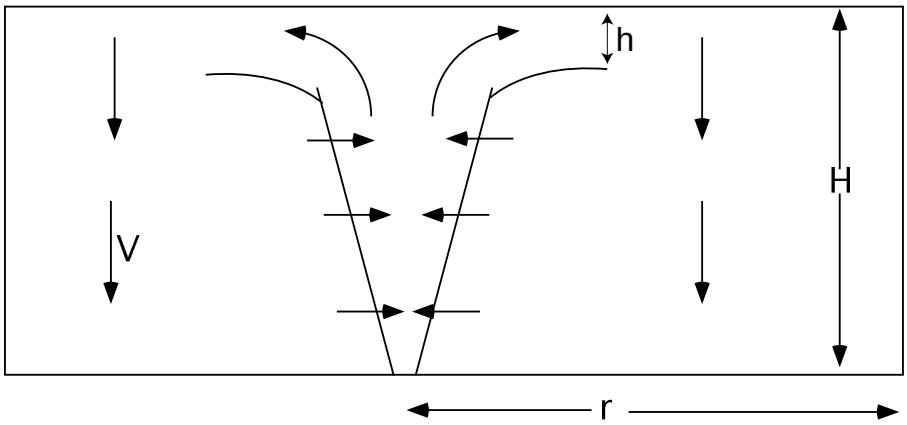

Figure 1.1: A schematic illustration of the "filling box" model of Baines & Turner (1969), showing the entrainment of fluid by the plume and vertical advection v in the tank. This box has radius r and depth H.

Worster and Huppert (1983) approximated the entrainment equations to obtain an analytic solution for the time evolution of the density gradient. They showed that below the first front the density gradient quickly reaches that of the steady state, an observation that agrees well with experiment. Manins (1979) extended the description of the "filling box" model and set limits on the aspect ratio of the box, so that inertial recirculation driven by the momentum of the plume outflow is avoided. For tanks of aspect ratio $H/r \gg 1$ the whole tank is characterized by vertical accelerations comparable to horizontal accelerations and the tank remains mixed. Baines & Turner (1969) and Barnett (1991) both concluded that the outflow depth increases with the aspect ratio, for an aspect ratio $H/r > 1$.

For small aspect ratios (wide basins) Manins (1979) found that the outflow occupies 1/4 of the total depth of the plume fall. However, due to the lack of any strong density gradients in this region, the outflow makes little difference to the asymptotic density gradient. Manins defined a Froude number for the flow and showed that when the outflow thickness is small (as assumed by Baines & Turner, 1969) the flow entrains fluid from above causing the outflow to deepen until it reaches an equilibrium depth.

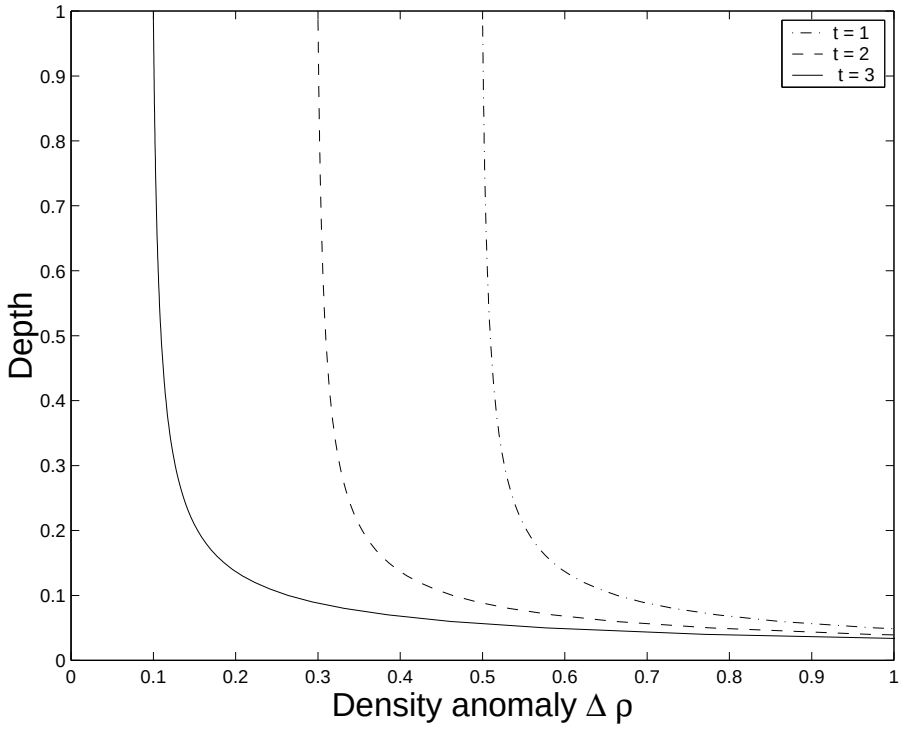

Figure 1.2: The density profiles that result at three successive times. The density profile remains a constant shape while decreasing in density linearly at every point.

Other studies relevant to the present problem have shown that when there is a pre-existing gravitationally stable density gradient in the water and a destabilizing heat flux is imposed at a horizontal boundary, a mixed layer forms and increases in depth with time. This is relevant to, for example, the formation of the surface mixed layer of a lake during nocturnal winter cooling, or the oceanic mixed layer during times of low wind but strong surface cooling. Turner (1973) and Manins & Turner (1977) showed that a balance of the kinetic and potential energy involved in the mixing gave a convecting layer depth with the time evolution $h \propto t^{1/2}$. Deardorf *et al.* (1980) investigated the mechanism of convective mixing as a function of a Richardson number, defined as $Ri = g\Delta\rho h/(w^*)^2$, where g is the acceleration due to gravity, $\Delta\rho$ is the density difference, w^* the r.m.s. eddy velocity of the convective motion in a convecting layer of depth h. When the penetrative eddies reached the base of the mixed layer they penetrated a distance Δh in the underlying stratification. Deardorf *et al.* (1980) found that even for mixed layers with high Ri the normalized interface thickness $\Delta h/h$ was approximately 0.2.

When a layer is subjected to both a destabilizing uniform boundary flux and a localized

flux, competition between overturning and stratification-building is expected to depend on the relative strengths of the two sources and the box aspect ratio. We define R to be the ratio of the total buoyancy flux BA through the base (where B is the buoyancy flux per unit area and A is the base area of the tank) to the total buoyancy flux F from the localized source as

$$R = \frac{BA}{F}, \tag{1.1}$$

and investigate the behaviour of the system as a function of R in the long-time limit. We make use of laboratory experiments in which a basal heat flux is applied to a box of water while the plume is driven by either a small source of dense salt solution at the top or a source of less dense fresh water at the base. Of particular interest is whether a mixed layer of steady depth can exist with a part of the water column well-mixed and a part stratified.

1.1.2 Stratification produced by surface cooling in lakes with significant shallow regions

In many lakes, reservoirs and estuaries the interaction of surface cooling with sloping bathymetry results in the generation of downslope flows of cold dense water that can lead to the formation of stratification. The formation of gravity currents has been observed in field studies by Monismith *et al.* (1990) where differential cooling, due to variations in reservoir bathymetry or surface wind speed, led to strong horizontal circulation in a reservoir. Gravity currents have been observed flowing down topography in Lake Geneva, Switzerland (Fer *et al.*, 2000) and in Lake Tahoe, California, USA (Thompson & Schladow, *pers. comm.*) where they are believed to have filled the deep basin with dense cold water. James & Barko (1991) observed gravity currents transporting significant amounts of phosphorous from the shallow to the deeper regions of Eau Galle reservoir, Wisconsin, USA. Thermistor chain data show the ubiquitous presence of convectively-driven circulation in billabongs (Sherman *et al.*, unpublished data), shallow lakes and wetlands (Arnold & Oldham, 1997). The relationship between the volume flux of a gravity current, the surface cooling rates and the side arm geometry has been studied numerically by Horsch & Stefan (1988) and in the laboratory by Maxworthy (1997), Sturman & Ivey (1999), Sturman *et al.* (1999) and Finnigan & Ivey (1999, 2000) .

Away from shallow regions, surface cooling of a reservoir leads to a well-mixed surface

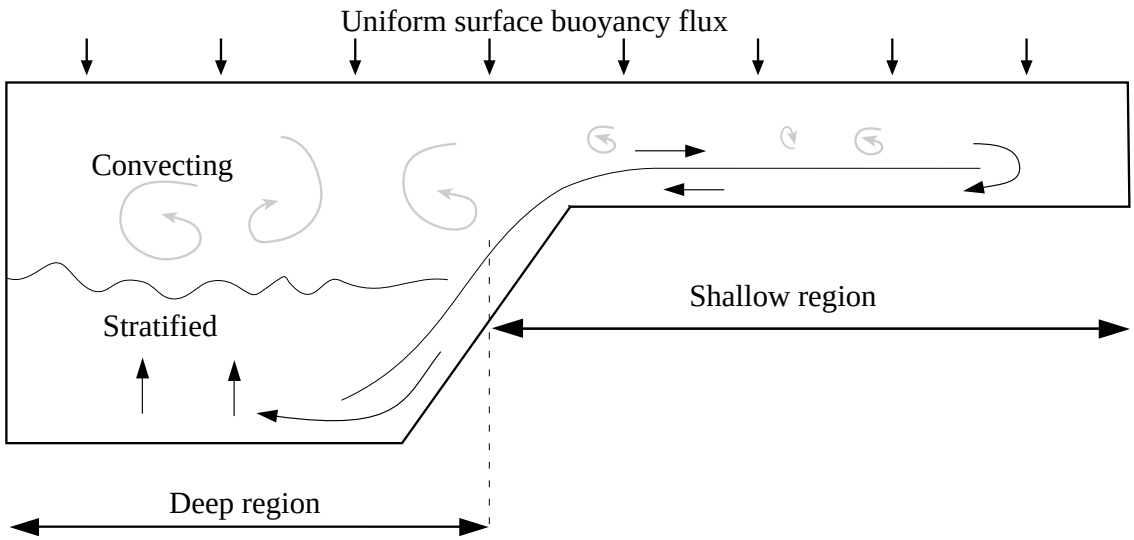

Figure 1.3: A uniform destabilizing buoyancy flux per area is provided to the surface of a reservoir with a deep region which has a shallow side arm. The shallow region cools rapidly and produces a gravity current that fills the deep region with cold dense fluid. This causes a general up-welling of cold fluid. Near the surface of the deep region there is a convecting layer.

layer that can erode the deep cold stratified layer. A surprising new result of this thesis is that if the rate at which cold dense water up-wells, due to continued input by the cold gravity current, balances the rate at which the mixed layer deepens due to entrainment by surface convection, then a steady mixed layer depth may result. This is sketched in figure 1.3. This development of stratification is in contrast to the normal assumption of 'winter overturning' of lakes and reservoirs. During spring and summer many lakes will develop a strong thermocline in response to surface heating. If there is already a strong thermocline present after winter then there will be important economic consequences for maintaining water quality and the prevention of toxic algal blooms.

To determine how the stratification depends upon the reservoir geometry, we conduct a series of laboratory experiments with a geometry similar to figure 1.3, where a destabilizing buoyancy flux is applied to the water column. By systematically varying the lengths and depths of the shallow and deep regions we determine the conditions for persistent stratification to develop. The theory and experimental results are then compared with bathymetry and field measurements of stratification that developed in response to winter cooling from the Chaffey reservoir, Australia, from a three year observation program by Sherman *et al.* (2000). This

reservoir had large shallow sidearms and persistently formed a steady surface mixed layer with a deep cold stratified layer. As the water column was not well-mixed, there were frequent winter blooms of dinoflagellates and buoyant cyanobacteria, that required expensive water treatment before it could be used by the nearby city of Tamworth.

1.2 The interaction between salt fingers, shears and intermittent turbulence

Salt finger instability occurs when relatively hot salty water overlays cooler, fresher water. A small parcel of water displaced downward loses heat faster than salt to the surrounding fresh, cool water, and so becomes denser which accelerates the flow. Similarly if cool, fresh fluid rises it gains heat and so becomes less dense. This results in an instability and a series of counter-flowing plumes as shown in the sketch in figure 1.4. The horizontal wavenumber, k, of the fastest growing perturbation is set by a balance between between thermal diffusion and viscous drag.

1.2.1 Salt finger instability

The opposing gradients of salinity and temperature are sketched in figure 1.5, where the stronger temperature gradient stabilizes the unstable saline gradient. Salt fingers grow most rapidly when the ratio, R_ρ of the mean temperature and salinity gradients, expressed in terms of their contributions to the density gradients

$$R_\rho = \frac{\alpha \overline{T}_Z}{\beta \overline{S}_Z}, \tag{1.2}$$

is close to one. Here $\alpha = -\frac{1}{\rho}(\frac{\partial \rho}{\partial T})_{S,p}$ is the coefficient of thermal expansion at constant pressure and salinity and $\beta = \frac{1}{\rho}(\frac{\partial \rho}{\partial S})_{T,p}$ is the coefficient of saline expansion at constant pressure and temperature. The horizontal over-bar in (1.2) denote that a horizontal average of T and S is used to calculate vertical gradients.

When $R_\rho < 1$ the density gradient is unstable and will overturn. An upper limit on the R_ρ

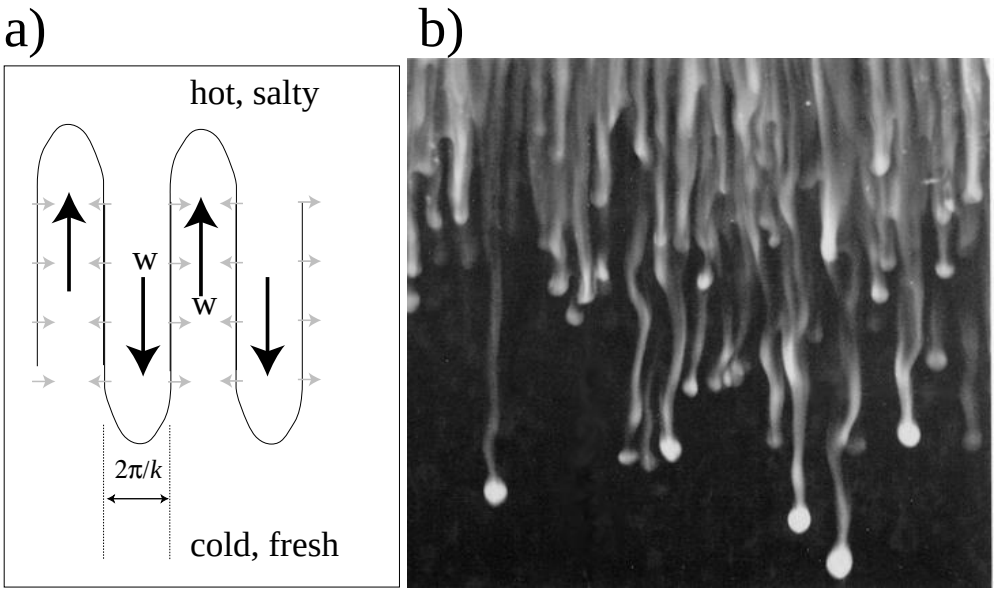

Figure 1.4: (a) A sketch of the salt finger instability. Heat flows rapidly down the temperature gradient (sketched by gray arrows) separating fingers, generating local density anomalies which drive vertical motion with velocity, w, and horizontal wavelength $2\pi/k$, where k is the horizontal wavenumber. (b) A laboratory photograph of salt fingers formed by hot salty water (containing fluorescene dye) overlying cold fresh water, photograph by J. Stewart Turner.

at which salt fingers can form is the ratio of thermal and saline diffusivities

$$\tau = \frac{\kappa_S}{\kappa_T}. \tag{1.3}$$

where $\tau = 0.01$ in sea water. Thus salt fingers can form when $1 \leq R_\rho \leq \tau^{-1}$. While heat and salt are the oceanographically interesting case, the salt finger instability can occur with any two components that have different diffusivities if there is an unstable gradient of the slower diffusing component and a stable gradient of the faster diffusing component (Turner, 1973). It has become standard to refer to the slower diffusing component as S and the faster diffusing component as T. In the laboratory the sugar/salt pair is often used where sugar is the slower diffusing S component and salt the faster diffusing T component, for which $\tau = 1/3$. The sugar/salt system is strictly an analogue to cold/salt rather than heat/salt, as increasing the concentration of T (salt) increases the density of the fluid. Using the sugar/salt system has the advantage that it avoids the problems caused by the difficulty of insulating the tank when there are large vertical temperature gradients. The main problem is that while density and

conductivity are easily measured, the concentration of each component is very time consuming to measure.

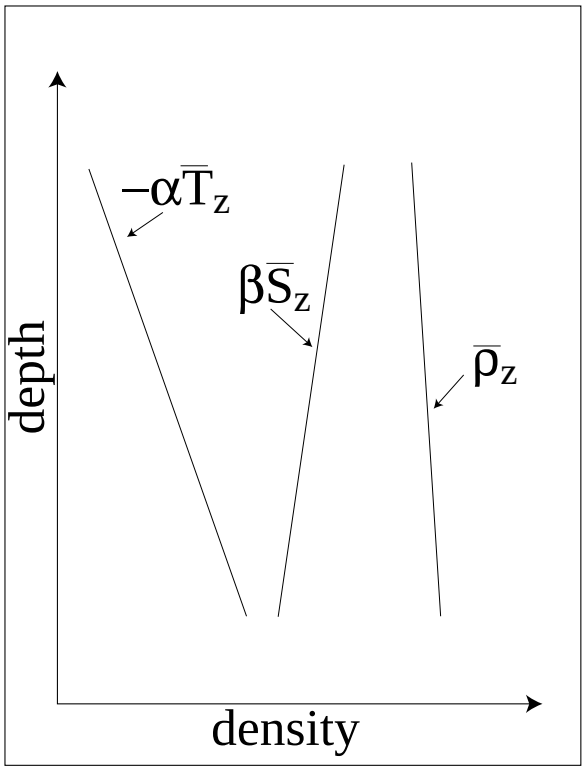

Figure 1.5: A sketch of the horizontally averaged profiles of T, S (in density units) and ρ within a salt finger region, for the heat/salt system.

Another important parameter of salt finger convection is the flux ratio

$$\gamma = \frac{-\alpha F_T}{\beta F_S}. \tag{1.4}$$

Laboratory measurements (Turner, 1967; Schmitt, 1979b; Griffiths & Ruddick, 1980; McDougall & Taylor, 1984) of the heat/salt system indicate $\gamma \approx 0.6$, and for sugar/salt $\gamma \approx 0.9$ for R_ρ near 1. Similar values were obtained in the numerical experiments of Shen (1995), Radko & Stern (1998), Stern & Radko (1999), and Merryfield & Grinder (2001). As $\gamma < 1$ this means that there is a net transport of density 'up gradient' and that the potential energy stored in the unstable S gradient is being released to drive the convection. In contrast, turbulent mixing requires an external input of energy and results in an increase in the potential energy of a density gradient, so it has a 'down gradient' flux of density.

1.2.2 Previous salt finger theory

The equations governing the time evolution of fingers in *deep linear gradients* of T and S were first formulated by Stern (1960) as an equation for the conservation of momentum

$$\frac{\partial w'}{\partial t} - \nu\nabla^2 w' = g(\alpha T' - \beta S') \tag{1.5}$$

and two conservation equations of T and S

$$\frac{\partial T'}{\partial t} - \kappa_T \nabla^2 T' + w' \frac{\partial \overline{T}}{\partial z} = 0 \tag{1.6}$$

$$\frac{\partial S'}{\partial t} - \kappa_S \nabla^2 S' + w' \frac{\partial \overline{S}}{\partial z} = 0, \tag{1.7}$$

where ν is the molecular viscosity, w' is the vertical velocity, S' and T' are the perturbations from the mean $\overline{S}$ and $\overline{T}$ and $\nabla^2 = \frac{\partial^2}{\partial x^2} + \frac{\partial^2}{\partial y^2}$ for tall, narrow fingers where $\frac{\partial^2}{\partial z^2} = 0$. .

One solution to the above system of equations, valid at small times, is to assume that the w T and S anomalies are sinusoidal in the horizontal and that the amplitudes grow exponentially with time.

$$(w', T', S') = (\hat{w}, \hat{T}, \hat{S})\, e^{\lambda t}\, \sin(kx)\, \sin(ky). \tag{1.8}$$

This reduces the system of equations (1.5) to (1.7) to

$$\hat{w}(\lambda - \nu k^2) = g(\hat{T} - \hat{S}) \tag{1.9}$$

$$\hat{T}(\lambda - \kappa_T k^2) + \hat{w}\overline{T}_z = 0 \tag{1.10}$$

$$\hat{S}(\lambda - \kappa_S k^2) + \hat{w}\overline{S}_z = 0. \tag{1.11}$$

Using the above equations, Schmitt (1979a) found the initial exponential growth rate for the fastest growing fingers as a complex function of $R_\rho, \tau = \kappa_S/\kappa_T$ and $Pr = \nu/\kappa_T$. As $\nu \gg \kappa_T \gg \kappa_S$ for the heat/salt case, an approximate solution was found by Kunze (1987) for the

initial exponential growth rate as

$$\lambda = \frac{1}{2}\sqrt{\frac{(\kappa_T - R_\rho \kappa_S) g\beta \overline{S}_Z}{\nu}} \quad \left(\sqrt{R_\rho} - \sqrt{R_\rho - 1}\right), \tag{1.12}$$

and that the wavenumber of the salt fingers is given by

$$k \approx \left(\frac{g\beta \overline{S}_z (R_\rho - 1)}{\nu \kappa_T}\right)^{1/4}. \tag{1.13}$$

This results in finger widths of order several centimeters in the ocean and of order millimeters in typical sugar/salt laboratory experiments.

1.2.3 Salt finger fluxes

The equations (1.9) to (1.11) require additional assumptions to determine the steady fluxes of T and S. In the following we discuss the way in which salt finger fluxes scale with the S gradients and differences between the fluxes through thin interfaces and deep linear gradients.

1.2.3.1 Thin interfaces

Most of the previous laboratory experiments on salt fingers have concentrated on the case where there is a well-mixed layer of hot salty water overlying colder, fresher water. Salt fingers can form at the interface between the two layers when $1 < \alpha\Delta T/\beta\Delta S < \tau^{-1}$, where $\alpha\Delta T$ and $\beta\Delta S$ are the respective T and S difference between the two well-mixed reservoirs, and α and β are the T and S expansion co-efficients.

For interfaces the dimensionless T flux, Nu, must be a function of the following variables

$$Nu = \frac{F_T}{\kappa_T \Delta T/d} \sim f\left(g\beta\Delta S, g\alpha\Delta T, d, \nu, \kappa_S, \kappa_T\right), \tag{1.14}$$

where d is the convective layer depth, g the acceleration due to gravity, κ_S and κ_T the respective molecular diffusivities of S and T, and ν is the viscosity of the fluid. These variables can be formed into of the non-dimensional parameters

$$Pr = \frac{\nu}{\kappa_T},\ \tau = \frac{\kappa_S}{\kappa_T},\ Ra = \frac{g\alpha\Delta T d^3}{\nu\kappa_T},\ Ra_S = \frac{g\beta\Delta S d^3}{\nu\kappa_T}, \tag{1.15}$$

giving $Nu \sim f(Ra, Ra_S, Pr, \tau)$. Turner (1967) assumed that the buoyancy flux only depended upon the properties of a thin boundary layer at the edge of the convecting region and did not depend upon the convective layer depth d or the Prandtl number, Pr. It then follows from the definition of Ra and Nu that

$$Nu = f\left(\frac{\beta\Delta S}{\alpha\Delta T}, \tau\right) Ra^{1/3}. \tag{1.16}$$

since this is the only form that removes the dependence of F_T on d. Using the definition of the Nusselt number (1.14), and the Rayleigh number (1.15), Turner (1967) then showed that

$$\beta F_T = f(R_\rho, \tau)\ (\beta\Delta S)^{4/3}. \tag{1.17}$$

The value of $f(R_\rho, \tau)$ was measured by Stern & Turner (1969) as $f(R_\rho, \tau) = 10^{-2}$ cm s^{-1} in sugar/salt experiments. Similar experiments by Lambert & Demenkow (1972) at lower values of R_ρ, found values of $f(R_\rho, \tau)$ in the range of 0.5×10^{-3} to 0.75×10^{-3} cm s^{-1}. Part of the reason for the difference between these results was explained by Griffiths & Ruddick (1980) who measured the dependence of $f(R_\rho, \tau)$ upon R_ρ and found that $f(R_\rho, \tau) \sim R_\rho^{-6}$. Recent numerical simulations of the salt finger fluxes across thin interfaces by Radko & Stern (2000) have also verified the functional form of (1.17).

1.2.3.2 Deep linear gradients

An interface between two well-mixed regions is no longer 'thin' when the thickness is much larger than the intrinsic finger length scale and the fingers are no longer connected to both of the well-mixed reservoirs. This occurs as salt fingers are not infinitely long (as assumed in 1.8) but rather have aspect ratio ratio of two or three, for $R_\rho < 2$ (Taylor, 1993; Shen, 1995). For salt fingers in deep 'crossed' gradients of S and T, the result of (1.17) does not apply. The extensive parameters which govern the dynamics of the salt fingers in deep linear gradients are $g\beta S_z, g\alpha T_z, \nu, \kappa_S, \kappa_T$, and there is no externally imposed length scale. These variables can be expressed in terms of the non-dimensional parameters

$$Pr = \frac{\nu}{\kappa_T},\ \tau = \frac{\kappa_S}{\kappa_T},\ R_\rho = \frac{\alpha T_z}{\beta S_z}. \tag{1.18}$$

and there is no Rayleigh number. The Nusselt number in this case is defined in terms of the gradients as

$$Nu = \frac{F_T}{\kappa_T T_z} \sim f_1(R_\rho, Pr, \tau). \tag{1.19}$$

For a given fluid, Pr and τ will be constant. Using the definition (1.19) leads to

$$F_T = f_2\left(R_\rho\right)\ \kappa_T \frac{\partial T}{\partial z}, \tag{1.20}$$

and for a given R_ρ the flux of T is linearly proportional to the gradient of T.

The equation (1.20) does not give the magnitude of the T fluxes or their dependence upon R_ρ. Various theoretical mechanisms have been proposed by which salt finger fluxes in deep gradients are limited. The initial growth of fingers is exponential, with growth rate (1.12), up to the point where shear instability of the fingers (described by a Froude or Reynolds number criterion) sets in (Kunze, 1987) and steady fluxes are then reached. Holyer (1984,1985) and Taylor & Veronis (1986) have identified vertical disturbances that grow at a wavelength comparable with the finger width, consistent with observations of Taylor (1993) that salt fingers with $1 < R_\rho < 5$ broke down into 'blobs' of aspect ratio of two. Direct numerical simulations of salt fingers in deep linear gradients have been used to parameterize the magnitude of the fluxes. In 2D and 3D numerical experiments of salt fingers in linear T and S gradients, Shen (1995), Radko & Stern (1998,2000), Stern & Radko (1999) and Merryfield (2001) developed scaling for the resulting non-dimensional T and S fluxes in terms of R_ρ.

1.2.4 Eddy diffusivity parameterization

Given the linear dependence of flux on gradient in (1.20), the fluxes can be written in the form of an eddy diffusivity as

$$F_T = -K_T(R_\rho)\ \frac{\partial T}{\partial z}. \tag{1.21}$$

Salt fingers are strictly a convective process but their fluxes in deep gradients can be modeled in the form of an eddy diffusivity. This assumption has been used by other authors such as Schmitt (1981), Walsh & Ruddick (1995, 1998) and Zhang *et al.* (1998) when studying vertical length scales much larger than the finger scale. For R_ρ close to one, salt fingers have aspect ratio near

2 (Taylor 1993) and hence the assumption of an eddy diffusivity is reasonable for modeling transport through distances much larger than the finger width.

The conservation equations governing the evolution of horizontally-averaged T and S within a deep field of salt fingers (Stern 1969) are simply written as

$$\frac{\partial S}{\partial t} = -\frac{\partial F_S}{\partial z}, \tag{1.22}$$

$$\frac{\partial T}{\partial t} = -\frac{\partial F_T}{\partial z}. \tag{1.23}$$

The fluxes of T and S are then

$$F_S = -K_S\left(R_\rho\right)\frac{\partial S}{\partial z}, \tag{1.24}$$

$$\alpha F_T = \gamma\,\beta F_S, \tag{1.25}$$

where γ is the ratio of T and S buoyancy fluxes due to salt fingers. Salt fingers transport S most efficiently, ($\gamma < 1$) and there is a net flux of density 'up gradient'.

Combining equations (1.22) and (1.24) gives the familiar Fickian 'diffusion' equation

$$\frac{\partial S}{\partial t} = K_S\frac{\partial^2 S}{\partial z^2}. \tag{1.26}$$

If one considers an S gradient composed of a steady part $\overline{S}$, with a small perturbation $\tilde{S}$

$$\frac{\partial S}{\partial z} = \frac{\partial \overline{S}}{\partial z} + \frac{\partial \tilde{S}}{\partial z}, \tag{1.27}$$

then the action of the salt fingers is to 'diffuse' away the $\tilde{S}$ perturbation, with an exponential decay rate given by

$$\lambda = \frac{K_S}{l^2}, \tag{1.28}$$

where l is the wavelength of the perturbation. This decay rate (1.28) is independent of both $\overline{S}_z$ and $\tilde{S}_z$.

Salt fingers cause an 'up gradient' flux of density, which is consistent with a negative

diffusivity of density, K_ρ. Mathematically modeling in terms of the diffusion equation for density with a negative diffusivity would imply that the amplitude of any density perturbations will *increase* exponentially with time. The exponential grow rate would be

$$\lambda = \frac{-K_\rho}{l^2}, \tag{1.29}$$

and the smallest scales would grow most rapidly. However the effective T and S diffusivities, K_S and K_T, are positive and it is only due to the coupling of T and S fluxes, by (1.25), that there is an 'up gradient' flux of density. The time evolution of S anomalies is simply one of enhanced 'diffusion'. Thus great care must be exercised in the use of the negative diffusivity for density and it will generally be essential to use explicitly the flux equations for both T and S. The coupling of fluxes in (1.25) means that the rate of change of $\tilde{T}$ is less than that of $\tilde{S}$ by a factor γ. An implication of this is that when salt fingers are dominant $\tilde{S}$ can 'diffuse' away, while changes in $\tilde{T}$ generally will be slower. The effects this has on density anomalies will be discussed in chapters 4 and 5. This approach is different to the model of Merryfield (2000), who considered the evolution of perturbations in a density gradient by 'up gradient' salt finger fluxes using a negative diffusivity of density.

Salt fingers in the ocean are usually present in a background of turbulence and it has not been clear whether the equilibrium fluxes predicted from numerical results will actually be realized. The effect of turbulence and shear on salt fingers has been studied in the context of eddies produced by an oscillating grid and impinging upon a density step, where salt fingers were growing (Linden, 1971; Altman & Gargett, 1987). In these studies the turbulence and salt fingers were spatially separated with turbulent entrainment occurring at the edges of the interface. When the turbulence was weak the turbulent eddies provided a shearing motion that limited the salt finger fluxes. When turbulence was strong the salt finger fluxes were totally disrupted. In the ocean turbulence is present only intermittently, so that fingers may have time to grow and reach their equilibrium fluxes between turbulent events and hence contribute significantly to diapycnal fluxes. In laboratory experiments (Taylor 1991) salt finger microstructure has been observed to rapidly re-emerge from a decaying turbulent event at $Nt \approx 10$ and then reach equilibrium structures after 5 to 10 e-folding periods. Related experiments by Turner & Chen (1974) found that when turbulence was spatially isolated in crossed linear

gradients of T and S, that a small mixing event could result in a breakdown to a well-mixed patch for active fingers (density ratio R_ρ near one), but at large R_ρ even vigorous initial mixing did not lead to any permanent well-mixed patches.

1.2.5 Salt fingers in oceanography

When first described by Stommel, Aarons & Blanchard (1956) salt fingers were termed an "oceanographic curiosity" but advances in observational technology meant that, by the time of the review by Schmitt (1994), it was thought that "the ocean is strongly unstable to double diffusive processes and profoundly influenced by their presence". Salt fingering-favourable gradients occur in much of the world ocean's mid-latitude thermocline, with much of the main thermocline having $R_\rho < 2$ (Figueroa, 1996). However, a difficulty in understanding the implications of salt fingers for ocean circulation arises because fingers are present in a background of internal waves, density fine-structure and intermittent turbulence. Hence it has been difficult to transfer many of the ideas developed in laboratory experiments to the complicated oceanographic environment in order to estimate fluxes, or even to unequivocally attribute fine-structure to salt fingering.

An important result from laboratory experiments has been that, when a stable linear T gradient is subjected to an imposed S flux at the vertical boundaries, a series of well-mixed convecting layers can form (Turner, 1973) separated by sharp steps in T and S. Observations of these "staircase structures" in the oceans can easily be made using the common CTD (conductivity - temperature - depth) probe because the vertical scale between the steps is of the order of several tens of meters. A probe only need have resolution of 1m to be able to detect this fine-scale structure. The first such observations were made under the Mediterranean outflow (Elliot, Howe & Tait 1974), in the Tyrrhenian sea (Molcard & Tait 1977) and in the Caribbean (Lambert & Sturges 1977). A first step in verifying that these $T-S$ staircases are caused by salt finger convection requires that the characteristic small scales, or micro-structure, of fingers can be distinguished from other processes such as turbulent mixing. A direct observation of salt fingers in the Caribbean $T-S$ staircases was first achieved by Williams (1975) who used an optical device to record photographs of thin vertical laminae with a wavelength of order several centimeters. The characteristic spectral signal of salt fingers was also observed in oceanographic measurements by Magnell (1976) and Gargett & Schmitt (1982) using towed

micro-structure recorders. The first large scale field program to investigate salt fingers was conducted in the Caribbean in 1985 over an area of 1 million km^2 (Schmitt *et al.* 1987). The C-SALT (Caribbean Sheets and Layers Transect) experiment made extensive fine-scale and micro-structure observations of a series of strong T and S steps in the main thermocline that had strong horizontal coherence for hundreds of kilometers. A significant result was that fluxes infered from micro-structure measurements were a factor of 10 lower than predicted by (1.17), using the salinity contrasts across the interfaces. The salt fingers were also observed to interact strongly with inertial shear (Kunze *et al.*, 1987) and turbulence was also found to be important in determining the vertical fluxes (Marmorino 1990).

While the C-SALT experiments found that salt fingers were present in the Caribbean $T-S$ staircases, these fine-scale layers are relatively rare in the ocean even though much of the main thermocline is favourable to the formation of salt fingers. This is thought to be due to the occurrence of turbulence disrupting salt finger fluxes, as had been observed in laboratory experiments of Linden (1971). The recent NATRE (North Atlantic Tracer Release Experiment) field program was conducted in a region of the north Atlantic where gradients are largely favourable to the salt fingers but without any strong fine-scale structure like the $T-S$ staircases such as those observed in the C-SALT experiments. Ruddick, Walsh & Oakey (1998) and St. Laurent & Schmitt (1999) were able to compare a direct measurement of diapycnal diffusivity made from the rate of spread of a passive dye tracer with measurements of micro-structure. By calculating the dissapation rates of thermal variance and kinetic energy, St.Laurent & Schmitt (1999) were able to determine the relative contribution of salt-fingers or turbulence as a function of Richardson number (Ri) and density ratio (R_ρ). The non-dimensional ratio of dissipation rates of thermal variance and turbulent kinetic energy, Γ, is theoretically predicted to vary for turbulence (Oakey, 1985) and salt fingers (McDougall & Ruddick, 1992). In regions of high shear, where $Ri < 1$ the model for turbulence described most of the observed Γ and when $Ri > 1$ most of the observed Γ was best described as being due to salt-fingers as a function of R_ρ. This led to estimates of diffusivity of heat and salt of $K_T = 0.08 \pm 0.01$ cm^2 s^{-1} and $K_S = 0.13 \pm 0.01$ cm^2 s^{-1}. St. Laurent & Schmitt (1999) found this agreed well with independent measurements of the tracer inferred mixing rates by Ledwell *et al.* (1993). Because $K_S > K_T$ they inferred that the contribution of salt fingers was significant. This suggests that salt fingers can be important in determining vertical T and S fluxes without necessarily forming easily

observed staircase structures, and so may be significant for vertical fluxes in the large regions of the ocean thermocline where $1 < R_\rho < 2$. A difficulty in generalizing the results of St Laurent & Schmitt (1999) is that while there are many large scale measurements of S and T gradients in the oceanic thermocline (Levitus, 1987), the frequency, variability and strength of turbulent events over the oceanic thermocline is not well known. Turbulence in the stable oceanic thermocline is generated by a variety of mechanisms (Gregg 1987) and measurements from NATRE by Polzin *et al.,* (2001) indicate that at any time about 5% of the water column is actively overturning due to turbulent events. This raises the question of the mechanisms by which the intermittent turbulence interacts with salt finger convection to determine diapycnal fluxes and whether the fluxes are linearly additive and what possible fine-scale structure may emerge.

The first evidence for the wide spread oceanographic influence of salt fingers was found by Schmitt (1981), who showed that the T-S curves in central waters of the north Atlantic were well described by curves of constant R_ρ rather than the straight lines one would expect from turbulent mixing between two different water bodies. By parameterizing the eddy diffusivities, K_S and K_T, as decreasing functions of R_ρ he found that any anomalies in R_ρ would decay to produce T-S curves of constant R_ρ. The potential influence of salt fingers on ocean circulation was investigated by Gargett & Holloway (1992) who examined the sensitivity of the GFDL ocean model to changes in the ratio of of K_T/K_S. They found that the circulation from the pole to the equator was very sensitive to choice of this ratio rather than the magnitude of K_T or K_S. To understand the dynamics of this complex model Gargett & Ferron (1996) carried out a simple four box model of thermohaline circulation to model the meridional overturning cell. With ratios of K_T/K_S from 0.5 to 2, they found that multiple equilibria in the form of the circulation could exist. Zhang *et al.* (1998) carried out a similar numerical experiment to Gargett & Holloway (1992) but used a parameterization of K_S and K_T similar to that of Schmitt (1981). They found that there were widespread regions of $1 < R_\rho < 2$ in most of their experiments and these led to a reduction of 8% in the pole-ward transport of heat and a 22% reduction in the meridional overturning rate compared to the case where heat and salt have the same diffusivities. Merryfield *et al.* (1999) also used the parameterization of Schmitt (1981) in the GFDL ocean model and found that it greatly improved the T-S relationships in the deep ocean. All these studies provide strong evidence that the influence of salt fingers is

significant in the thermohaline circulation. However as the results are all based on the *ad hoc* parameterization of Schmitt (1981), it is important to investigate in greater detail how effective diffusivities due to salt fingers are affected by inertial waves, shear and intermittent turbulence.

1.3 Thesis overview

In chapter 2 the circulation and stratification in a confined environment is systematically investigated when distributed and localized buoyancy fluxes are released from the same horizontal boundary and when they are released from opposite boundaries. The experiments are described and experimental results are compared with theoretical hypotheses. Particular attention is given to the final equilibrium depth of the convective layer.

In chapter 3 a geometry similar to that sketched in figure 1.3 is used to model the effect of winter cooling in a reservoir when a large fraction of the surface area is composed of shallow side arms. The formation of gravity currents in these regions is analogous to the buoyant plume sketched in figure 1.1 and similar stratification and circulation to that discussed in chapter 2 is expected. The ratio of the areas and the ratio of depths of the shallow to deep regions (as sketched in figure 1.3) are systematically varied and the resulting mixed layer depth is compared with theory. Results from laboratory experiments and theoryare then compared with field observations of winter stratification that developed in the Chaffey reservoir, Australia. The field data were obtained from a 3 year observation program run by Dr Brad Sherman of the Commonwealth Scientific and Industrial Research Organization (CSIRO), Division of Land and Water.

In chapter 4 the interaction of salt fingers with a spatially varying shear is examined. Strong shear reduces the vertical T and S fluxes as the fingers become bent over. Hence a spatially varying shear leads to flux divergences and could result in the generation of fine-scale structure in the ocean. By using theory and laboratory experiments the magnitude and timescales of the resulting density fine-structure are discussed along with an estimation of the timescales for the formation of fine-scale structure in an oceanographic setting.

In chapter 5 a theoretical and laboratory model is developed to study the interaction between isolated turbulent patches and deep salt finger favourable gradients. A turbulent patch will partially mix a density gradient and so leave a characteristic fine-scale signature. Once salt

finger convection has re-established after the turbulent event, the density structure will change due to divergences in the 'up gradient' buoyancy flux. These flux divergences weaken the density gradient in the partially mixed patch and can lead to overturning. Turbulent entrainment may then become important and the patch may deepen with time, as predicted by Stern & Turner (1969).

Chapter 6 discusses a laboratory experiment designed to measure the buoyancy fluxes that result from intermittent turbulence (generated by periodically towed grid) and deep linear salt finger favourable gradients. A theory is developed in terms of the *e*-folding periods of salt fingers relative to the time between turbulent events. Using typical oceanic values of turbulent intermittencies and the parameterization of Merryfield & Grinder (2001) to describe the eddy diffusivities of salt fingers, a parameterization of the time averaged salt finger diffusivities of T and S is suggested for use in large scale oceanographic modeling. This parameterization is compared to the *ad hoc* parameterization of Schmitt (1981).

The main conclusions of this thesis are summarised in chapter 7 and suggestions are made for future work.

Much of the research presented here has either been published or is under review. The material of chapter 2 is found in Wells, Griffiths & Turner (1999), chapter 3 is reproduced from Wells & Sherman (2001) and the study in chapter 4 forms the basis for Wells, Griffiths & Turner (2001).

Chapter 2

Competition between distributed and localized buoyancy fluxes in a confined volume

In this chapter we investigate the stratification and circulation that result when a distributed source and an isolated source of buoyancy are simultaneously present in a confined region. In §2.1 we examine the behaviour when fluxes are released from the same horizontal boundary and, in §2.2, when they are released from opposite boundaries. The experiments are described in §2.3 and experimental results are compared with theoretical hypotheses in §2.4. A discussion of geophysical applications is presented in §2.5.

2.1 Fluxes from the same boundary

The interaction of flows produced by two buoyancy sources released at the same lower boundary, is shown diagrammatically in figure 2.1 (a). Upon reaching the top of the layer, the plume generates an outflow that forces a general downwelling of water. The downwelling and entrainment of this water back into the plume produces a stable stratification. However, the density gradient produced by the plume, if it were not continuously replenished, would be overturned by the basal heating at a rate that can be calculated by applying the theory developed by Manins & Turner (1977). In the present situation we hypothesize that a constant convecting layer depth (less than the total depth of water) can exist. This occurs when the rate at which the top of the convecting layer is advected downwards by the plume-induced circulation, is equal to the rate of deepening of the convecting layer by bottom heating. If there exists such

a balance, the system will consist of a well-mixed layer of depth h and an overlying density profile similar to that sketched in figure 2.1 (b). Since the two buoyancy sources provide a non-zero net flux into the chamber the density everywhere must decrease linearly with time.

2.1.1 Entrainment - advection balance

If the convecting layer depth h is to be constant, then the rate of convective deepening, $U = dh/dt$, of the mixed layer must be equal and opposite to the downwelling velocity, v, of the stratified interior. Entrainment will tend to increase the mixed layer thickness while the filling box advection tends to decrease it. When these processes are not in balance, due to either a small perturbation or initial conditions, the unequal advection and entrainment will act to return the interface towards the steady position.

We can determine U from Manins & Turner (1977), who derived a result for the time evolution of h for a convectively mixed layer beneath a constant density gradient as

$$h = \sqrt{6E^*}\, B^{1/2}\, N^{-1}\, t^{1/2}, \tag{2.1}$$

where $N = (-g/\rho\ d\rho/dz)^{1/2}$ is the buoyancy frequency. The value of the mixing efficiency constant, E^*, is related to the fraction of the kinetic energy of the convecting layer which is converted into potential energy by mixing less dense overlying water downward in to the mixed layer. If there is extensive penetrative convection and entrainment creating a sharp density step at the top of the convecting layer, then all the deepening is due to working of the convective motions against buoyancy forces and $E^* = 1$. On the other hand, if convection is less vigorous and the density profile remains continuous, mixed-layer deepening is by "encroachment" only (heating of the mixed layer), and $E^* = 1/3$. We allow N to be a function of depth in (2.1) and eliminating t gives

$$U = 3E^*\, B\, N(z)^{-2}\, h^{-1}, \tag{2.2}$$

where $N(z)$ is now the depth-dependent buoyancy frequency at depth h.

Changes of the density in the filling-box stratification are due only to vertical advection (Baines & Turner 1969) so that

a)

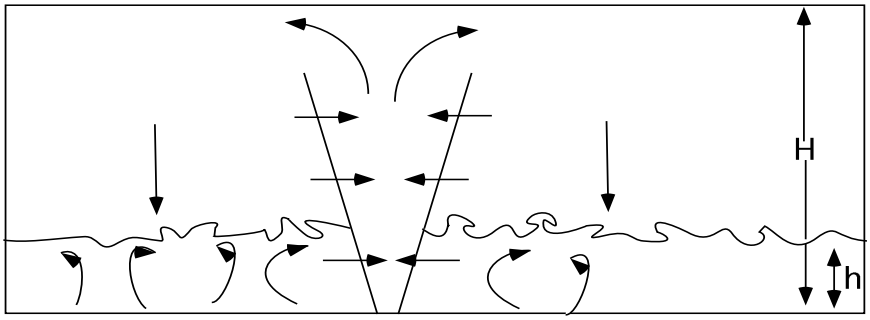

b)

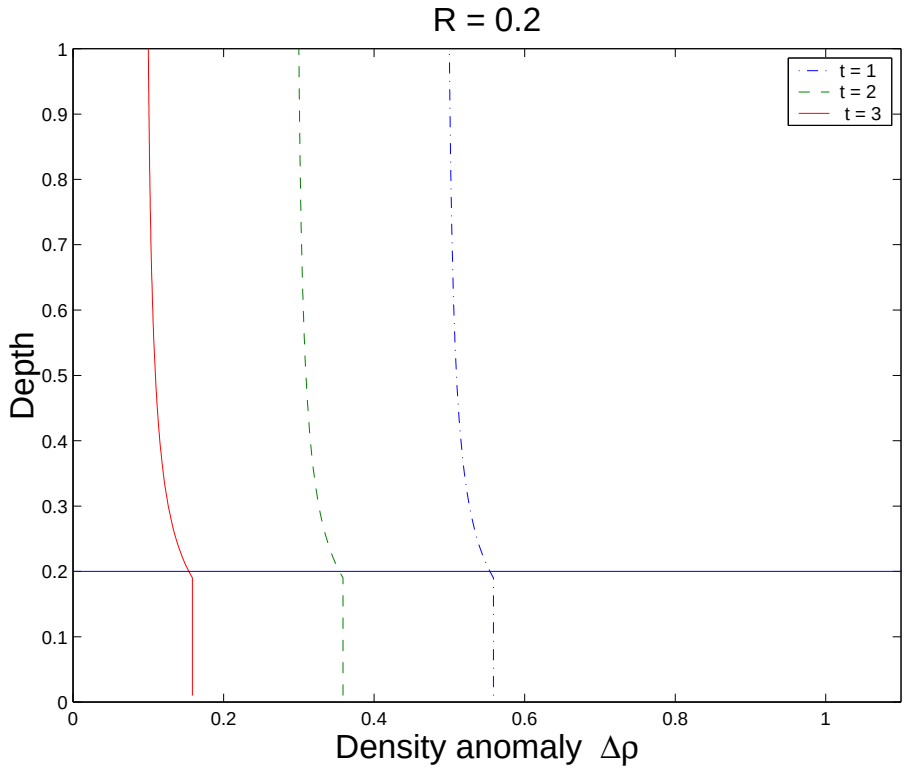

Figure 2.1: (a) A diagrammatic illustration of the expected flow pattern, with a mixed layer depth h and (b) density profiles that result at three successive times, for heating from the bottom boundary and a relatively fresh-water plume source at the base. Here $R = 0.2$ and the horizontal line shows the expected depth to which there is mixing due to convection from the base.

$$\frac{\partial \rho}{\partial t} = -v\frac{\partial \rho}{\partial z}. \tag{2.3}$$

Since the density profile has a constant shape at large times the density changes with time everywhere at the same rate. The rate of density change at all levels in the tank will simply be given by the total input of buoyancy into the tank,

$$\frac{d\rho}{dt} = \frac{\rho F(1+R)}{AHg}. \tag{2.4}$$

The density profile is uniform in the mixed layer and of the form given by Baines & Turner (1969) in the stratified region. Using (2.3) and (2.4) the downwelling velocity v is

$$v = -\frac{\rho F(1+R)}{AHg}\left(\frac{\partial \rho}{\partial z}\right)^{-1}. \tag{2.5}$$

Setting $U = -v$ for a steady mixed layer depth gives

$$\zeta_{mixed} = \frac{R}{1+R}3E^*. \tag{2.6}$$

where $\zeta_{mixed} = h/H$ the normalized mixed depth. If mixing into the convecting layer is due to encroachment alone we have $E^* = 1/3$ (Manins & Turner, 1977) and $\zeta_{mixed} = R/(1+R)$. The relationship between E^* and η (the ratio of the downward buoyancy flux due to entrainment B_e relative to the buoyancy flux from the boundary B), was found by Manins & Turner (1977) to be

$$E^* = \frac{1}{3}(2\eta+1). \tag{2.7}$$

The ratio η has been found (Denton & Wood, 1981) to empirically depend upon the Richardson number and Peclet number as

$$\eta = \frac{0.20\,Ri}{1+0.41\,Ri^{3/2}} + \frac{0.18\,Ri}{Pe}. \tag{2.8}$$

There is a maximum value of $\eta = 0.2$ when $Ri \approx 1$ for high Pe. For large Ri, η approaches zero. Using the result of (2.7) and (2.8) we see that E^* is a function of Richardson number and varies between $E^* = 1/3$ for high Ri to a maximum of $E^* = 0.46$ for low Ri when the interface is entraining. The result of (2.6) is a general result for any plume source in a confined region

-the exact form of the plume is important only in terms of evaluating the exact density gradient to determine E^*.

Using the idea of the entrainment - advection balance we can also determine a characteristic time taken for the system to converge from initial conditions to the steady mixed depth. If the system starts from a configuration where convection initially dominates then when the plume is started a front will develop that is advected downwards until the steady depth h is reached. From Baines & Turner (1969) the time it takes the position of the first front to reach a distance $\zeta = z/H$ from the opposite boundary for a point source plume is given as

$$t = \frac{5}{4\alpha}\left(\frac{5\pi}{18\alpha}\right)^{1/3} r^2 H^{-3/2} F^{-1/3}\left[(1-\zeta)^{-2/3} - 1\right], \tag{2.9}$$

where α is an experimentally determined entrainment constant equal to 0.1 and r is the effective tank radius. Substituting the value of ζ appropriate for the steady mixed depth at a particular value of R gives a timescale on which the system converges to the steady mixed depth. Similarly if the plume was started before the basal heating, the tank would be stratified and the system would converge to the steady mixed depth on a timescale determined from (2.1) where $N(z)^2$ is the stratification produced by the filling box process, given by (2.14) below.

2.1.2 Interface thickness

At the interface between the convectively mixed layer and the stably stratified region there must be a transition region in which convective elements have penetrated and partially mixed the density gradient. The thickness of this interface, Δh, is a function of Richardson number and adds to the apparent depth of the convecting layer when it is viewed in terms of convective motion or small-scale refractive index gradients. Hence (2.6) under-estimates the total depth of the mixed layer. In order to estimate the thickness of the interface we consider the average kinetic energy of heated convective elements in the turbulent mixed layer. Experimental studies (Deardorf *et al.*, 1980) indicate that at low Ri the empirical relationship is

$$\frac{\Delta h}{h} = 0.21 + 1.31 Ri^{-1}, \tag{2.10}$$

derived as a curve fit to experimental data, valid for the range $5 < Ri < 40$.

This means that the observed mixed depth ζ will be greater than that given by (2.6) by

$$\zeta_{mixed} = \left(1.21 + 1.31Ri^{-1}\right) 3E^{*} \frac{R}{1+R}. \tag{2.11}$$

In our experiments, a gradient form of the Richardson number can be defined as

$$Ri_g = \frac{N^2 h \Delta h}{w_*^2}, \tag{2.12}$$

with w_* the root-mean-square velocity of the convective turbulent motions. As the experiments of Deardorf *et al.* (1980) used a linear density gradient their values of *Ri* would be the same as if they had used Ri_g, allowing a meaningful comparison to be made between results. Experimental and theoretical work of Adrian *et al.* (1986) has determined that

$$w_* = 0.6(Bh)^{\frac{1}{3}}. \tag{2.13}$$

The buoyancy frequency is taken from the filling box solution of Baines & Turner (1969) and can be expressed as

$$N^2 = 1/4(\pi)^{-2/3} F^{2/3} \alpha^{-4/3} H^{-5/3} \frac{\partial f_o}{\partial \zeta}, \tag{2.14}$$

where α is the entrainment coefficient and f_o is the non-dimensional density gradient in the "filling box" as defined in Baines & Turner (1969). If we assume that $\Delta h \approx 0.2h$ and $R = \zeta/(1-\zeta)$ then the gradient Richardson number (2.12) can then be written as

$$Ri_g \approx 0.69\pi^{2/3}(1-\zeta)^{2/3}(r/H)^{4/3}\alpha^{-4/3}\frac{\partial f_o(\zeta)}{\partial \zeta}, \tag{2.15}$$

which is a weak function of the aspect ratio H/r, but a strong function of the convecting layer depth, partially due to the form of $f_o(\zeta)$. For large values of ζ, Ri_g is small (~ 5) and we see a significant interface thickness.

2.2 Fluxes from opposite boundaries

2.2.1 Qualitative description of the flow

When the plume source is at the top boundary and heating is again at the base, the plume outflow spreads along the base, where it heats up. Thus the total buoyancy flux supplied to the water at the base of the tank is reduced by the basal buoyancy flux. When the magnitude of the base buoyancy flux BA is greater than that from the plume source F then $R < -1$, and a stable density gradient cannot develop and the whole water column overturns. When the magnitude of the distributed boundary flux is less than that of the plume flux ($R > -1$), a stable gradient similar to that in the "filling box" solution may develop (in at least some of the water depth), but the density gradient will be reduced by the factor $1 + R$ below the strength of the gradient that would be produced by the plume alone. Since the plume buoyancy flux at each depth within the upper stratified region is unchanged, the entrainment and plume volume fluxes, and hence the vertical advection velocity and shape of the density gradient, are also unchanged. This result can also be derived using the equations of Baines & Turner (1969) modified for the effect of the additional buoyancy into the outflow layer.

We predict that for $0 > R > -1$ an asymptotic state can be achieved in which the density profile has two distinct regions, a stably stratified region overlying a well-mixed layer of depth h, as illustrated in figure 2.2. The uniform mixed layer is maintained by the turbulence generated by shear in the plume outflow. However the advective balance that can maintain a steady mixed-layer depth in our previous case of buoyancy sources on the same boundary (§2.1) is no longer possible - both plume filling of the interior and mixing by convection in this case act to deepen the mixed layer. In the present case we recall the mechanism which limits the depth of the turbulent outflow layer of the plume when $B = 0$. Here the turbulent kinetic energy of the outflow must do work against buoyancy, and the extent of mixing is limited. When $B > 0$ the density gradient is reduced by a factor of $(1 + R)$ by the bottom heating, but the available kinetic energy in the plume outflow is dependent only upon F. The density gradient is reduced by the heating from the base so the mixed depth will increase with R until, at $R < -1$, there is no stabilizing density gradient and the whole tank becomes well mixed.

a)

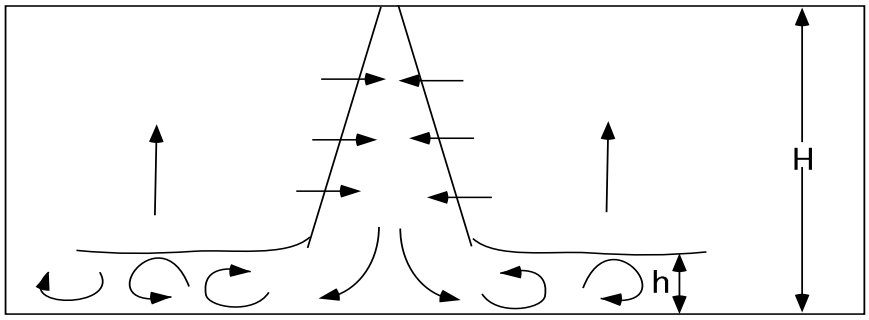

b)

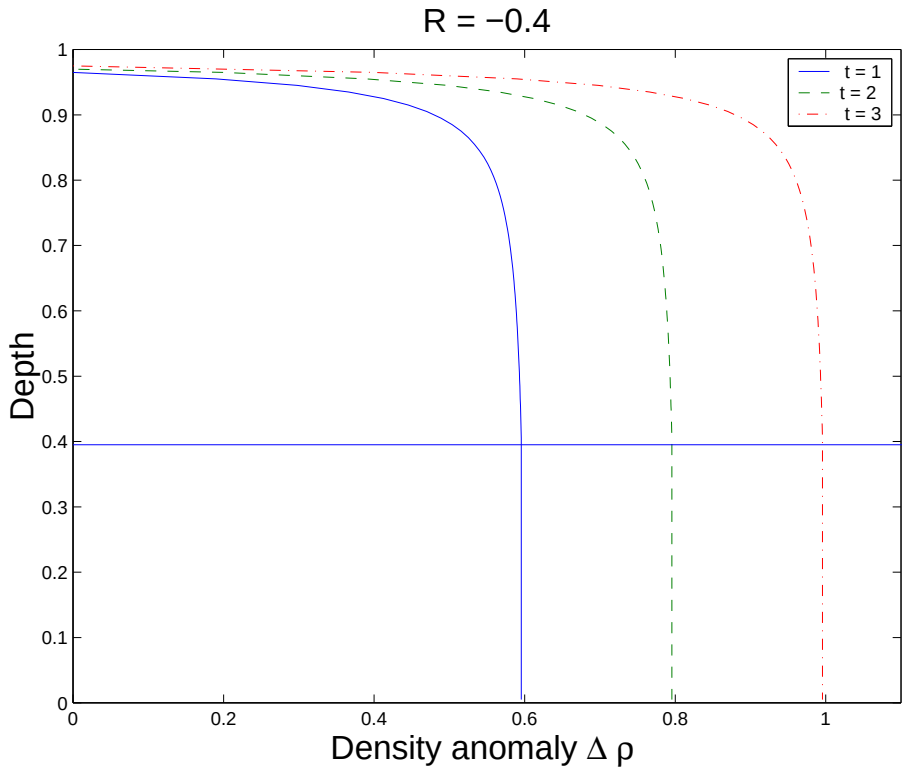

Figure 2.2: (a) A diagrammatic illustration of the flow pattern with a mixed layer depth h. (b) The expected density profiles at three successive times for the case of a plume source at the top and heating from the bottom boundary. As the plume source is in the opposite sense to figure (2.1) the density increases with time and the maximum density gradient is near the top of the tank. Here $R = -0.4$ and the horizontal line shows the depth to which the plume's turbulent outflow mixes the overlying stratification.

2.2.2 The shear generated turbulent mixed layer

The depth of the turbulent outflow from an axisymmetric plume was found experimentally to be $\zeta \approx 0.25$ (Manins, 1979). With the addition of heating at the base, the turbulent kinetic energy in the outflow will be the same, controlled only by the plume buoyancy flux and the depth of water. Thus we expect that the mixed depth, ζ_m, increases monotonically from the value of $\zeta_m \approx 0.25$ at $R = 0$ to $\zeta_m = 1$ (mixing through the whole depth) when $R = -1$. Aspect ratios larger than 1 (deep, narrow boxes) are expected to lead to full mixing also at some $R > -1$ due to creation of a vortex recirculation at the tank wall.

The mixed depth in this case can be predicted from the total buoyancy flux per area $B+F/A$ and the mean outflow velocity u of the turbulent outflow layer. These provide a length scale physically analogous to the Monin-Obukhov scale (Turner 1973, 1986) as

$$L \sim \frac{-u^3}{B+F/A}. \tag{2.16}$$

When L is positive a relatively dense bottom mixed layer will form and when L is negative the heat input will be gravitationally unstable and a deeper mixed layer will form. As the volume flux is conserved at the base of the plume, the initial outflow velocity of the layer will be directly proportional to that of the plume, hence $u^3 \propto -F/H$. If we assume that the mixed depth scales as L in (2.16), then

$$\zeta_m \sim L/H \sim \frac{c}{1+R}, \tag{2.17}$$

where the constant of proportionality c is taken to be 0.25 to agree with observations and theory of Manins (1979) for $R = 0$. For larger basal fluxes $|R|$ is larger and the shear mixed layer is deeper. For $R < -1$ the total buoyancy flux is destabilizing and the whole tank will overturn. It is expected that this relationship will only be valid for small R. As the magnitude of R increases, the effects of penetrative convection and the radial dependence of the outflow velocity and heating will modify (2.17). The decreasing radial velocity as the plume spreads out will be compensated by a greater uptake of heat by the slower flow, so that initially ζ_m would not change as rapidly with R as (2.17) suggests and complete overturning ($\zeta_m = 1$) will occur closer to $R = -1$.

2.3 Experimental design

Experiments were carried out in a square Perspex tank with 50 cm $\times$ 50 cm, filled with water to a depth of 15 or 35 cm. Base heating was provided by an electrical heating mat capable of running at powers of up to 2kW. This was insulated from below to ensure that most of the power dissipated in the mat was transfered to the water, and overlaid by a 4mm sheet of copper to ensure a uniform heat flux. The Perspex walls and a floating foam roof provided sufficient insulation of the water against heat loss from the water to the room. The two different water depths gave aspect ratios of approximately 0.5 and 1.

Plumes were produced either by releasing very small volume fluxes of dense salt solution at the top of the fresh water column (the opposite boundary from the heat flux) or by using a strong salt solution in the tank and releasing fresh water from a source through the centre of the base. In each case the release was at a constant rate and from tubes 7mm in diameter. The buoyancy flux of the plume is given by

$$F = g\frac{\Delta\rho}{\rho_o}Q, \tag{2.18}$$

where Q is the volume flux and $\Delta\rho$ is the density difference between the incoming fluid and the reference density, ρ_o, of the water in the tank. Source density differences of $\Delta\rho/\rho_o = 0.13$ to 0.18 were used, and buoyancy fluxes were typically $F = 20$ to 40 cm^4 s^{-3}. The volume fluxes, measured using a Gapmeter flow meter, were sufficiently small that both the mass and momentum fluxes from the sources could be neglected. To ensure that the flow became fully turbulent when it left the nozzle, we either placed cross-hairs inside the end of the tube or used a mechanical vibrator on the pipe. Experiments of Bloomfield & Kerr (1998) used very similar volume fluxes and tube diameters to generate plumes and jets, and they found over a comparable range of conditions that the virtual point plume source was less than 1cm inside the tube. This small correction changes the effective depth H by less than 5%.

The integrated buoyancy flux BA from the base is given by

$$BA = g\frac{\alpha_T J}{\rho c_p}, \tag{2.19}$$

where J is the total heat flux, α_T is the coefficient of thermal expansion of the water or salt

solution (taken from data in the CRC Handbook 1985) and c_p is the specific heat of the water at constant pressure (taken from data in Kaye & Laby 1973). The heat flux J was determined from both a direct measurement of the rate at which the temperature in the tank increased while it was stirred and from a measurement of the power dissipated in the heating mat. The two methods agreed well, indicating that at most 5% of the input heat was lost to the surroundings through the top, walls or base. Changes in salinity of the water within an experiment were very small, whereas changes in temperature of the order of 10°C were common. Hence the average value of α could change by a factor of 2 and the buoyancy flux was no longer constant for a fixed heat flux. Thus no truly steady mixed layer depth was achieved. Instead, the system reached a quasi-steady state in which the depth of the mixed layer increased as B (and $|R|$) slowly increased with time. The ratio of fluxes, R, was adjusted by changing the base heat flux.

Shadowgraph techniques were used since the sharp changes in refractive index gradient at the boundary of the turbulent region offered an easy means to measure the outflow thickness of the plume and the depth of active convection. Passive dye tracers and time lapse video recording also proved helpful in determining the mixed layer thickness by revealing regions of rapid mixing. The conductivity and temperature were measured as functions of depth (Head Precision Engineering model 5021) and the salinity and density profiles were calculated from these using the polynomials of Ruddick & Shirtcliffe (1979). Profiles were taken halfway between the plume and the tank wall and it was assumed that the structure far from the plume was independent of horizontal position. Each experiment was run until the mixing depth ζ and the shape of the T and S profiles were in a quasi-steady state. As a guide it was assumed that the quasi-steady mixed depth was approached once the first front produced by the plume had been advected through 80% of the depth of the tank (Worster & Huppert 1983). This was typically 30 - 45 minutes after the plume was turned on, and we ran the experiments for 60 - 90 minutes. The majority of experiments were started with the plume and heating turned on simultaneously. Some experiments were started with one source on much earlier than the other, but the same steady mixed depth resulted after a time period that was well described by either the advection of the first front or convective entrainment into the stratified layer above. This indicated that in the long time limit there was no dependence upon initial conditions.

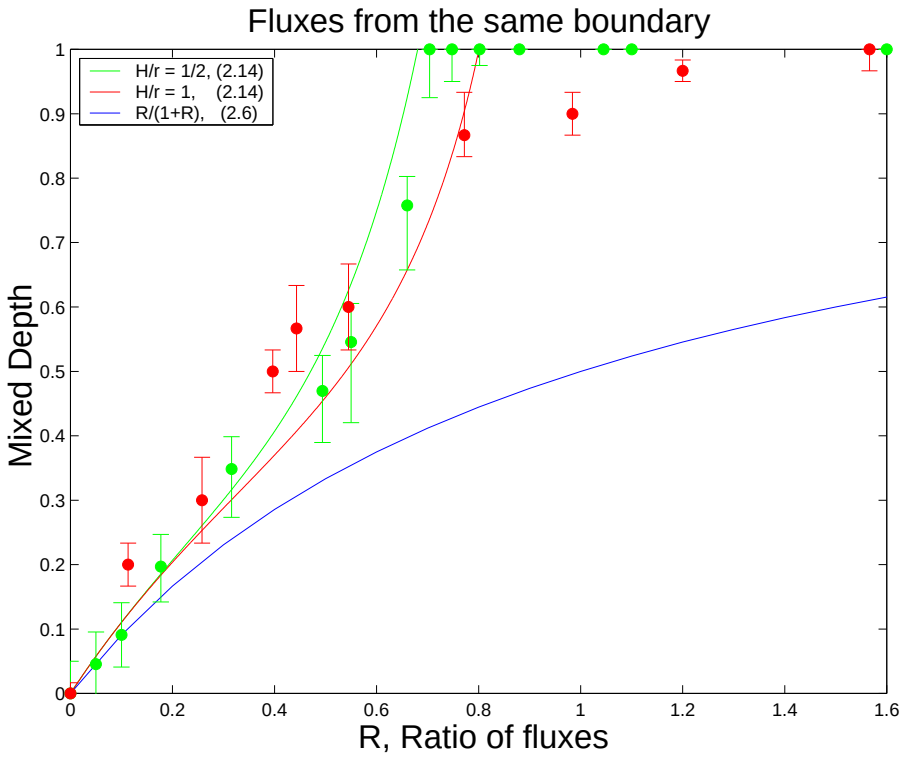

Figure 2.3: A comparison of experimental results and theory (2.6 and 2.11) for the steady state mixed depth when the sources are on the same boundary, for aspect ratios of 0.5 and 1. We see that full depth mixing occurs for $R \approx 1$.

2.4 Experimental results for fluxes from the same boundary

The quasi-steady mixed layer depths ζ measured from shadowgraph visualization, are shown in figure 2.3. The steady mixed depth ζ varies from 0, when there is no heating, to the whole depth overturning $(\zeta = 1)$ when $0.8 < R < 1.2$. There is some dependence upon the aspect ratio with the narrower tank showing full depth overturning earlier than the wider tank. The mixed layer depth is much deeper than predicted by (2.6), plotted in figure 2.3 with $E^* = 1/3$. There is much better agreement with (2.11), which includes the thickness the interface and is plotted in figure 2.3 with $E^* = 0.4$. The density gradient in figure 2.1 is very weak in the plume outflow region, so the Richardson number becomes low for large ζ and hence the interface thickness becomes large. The weak aspect ratio dependence in (2.11) also matches the data well, with the narrower tank having a relatively deeper mixed layer than the wide tank for a given R. The error-bars in figure 2.3 are of order 20% of h, which is roughly the thickness

of the interfacial region produced by penetrative convection.

Measurements of the density profile when the steady mixed depth had been reached were made for the case of no base heating ($R = 0$) and for $R = 0.4$. In figure 2.4 (a) there is no heating, and the predicted "filling box" density profile of Baines & Turner (1969) developed quickly, approaching its constant asymptotic shape and decreasing in density with time in a linear rate.

In figure 2.4 (b) we plot profiles for R = 0.4, when the position of the the mixed depth was steady.When both heat and salinity are used to provide buoyancy fluxes,there will be concentration gradients of each component. However, the individual profiles will give density contributions of similar forms, both being stable above the mixed layer and near uniform in the mixed layer. A small fraction of the heat flux into the mixed layer is entrained into the plume to produce the overlying temperature profile, which produces a thermal contribution to the stable density gradient of the same form as the salinity gradient. As the flux of heat out of the base by entrainment into the plume is small relative to the input by basal heating, we see a minimum in temperature just above the mixed layer.

The density profile retains a constant shape with time, while decreasing linearly with time between measurements. The transition from the stratified region to the convecting region occurs at a position that agrees well with the measurements from the shadowgraph. The profiles shown are instantaneous (rather than time-averaged) and hence they ignore significant variability in the top of the mixed layer. The transition from the stratified region to the well mixed region is of the same order as the interface thickness for the salinity profile. Due to thermal diffusion the temperature interface is about twice as thick as the salinity interface. In the stratified region, the density and salinity profiles have the same shape as in the case with no bottom heating as they are again controlled by the filling box mechanism. However, the entrainment of heat from the convecting layer gives rise to a characteristic stable temperature gradient in the stratified region.

The use of heat and salt to provide the two buoyancy fluxes also leads to some double diffusive effects in the experiments. For $R < 0.2$ a "diffusive" interface formed at the top of the mixed layer and the gradient region immediately above broke down to form a second convecting layer. This second layer was relatively shallow and appeared to make little difference to the predicted mixed depth.

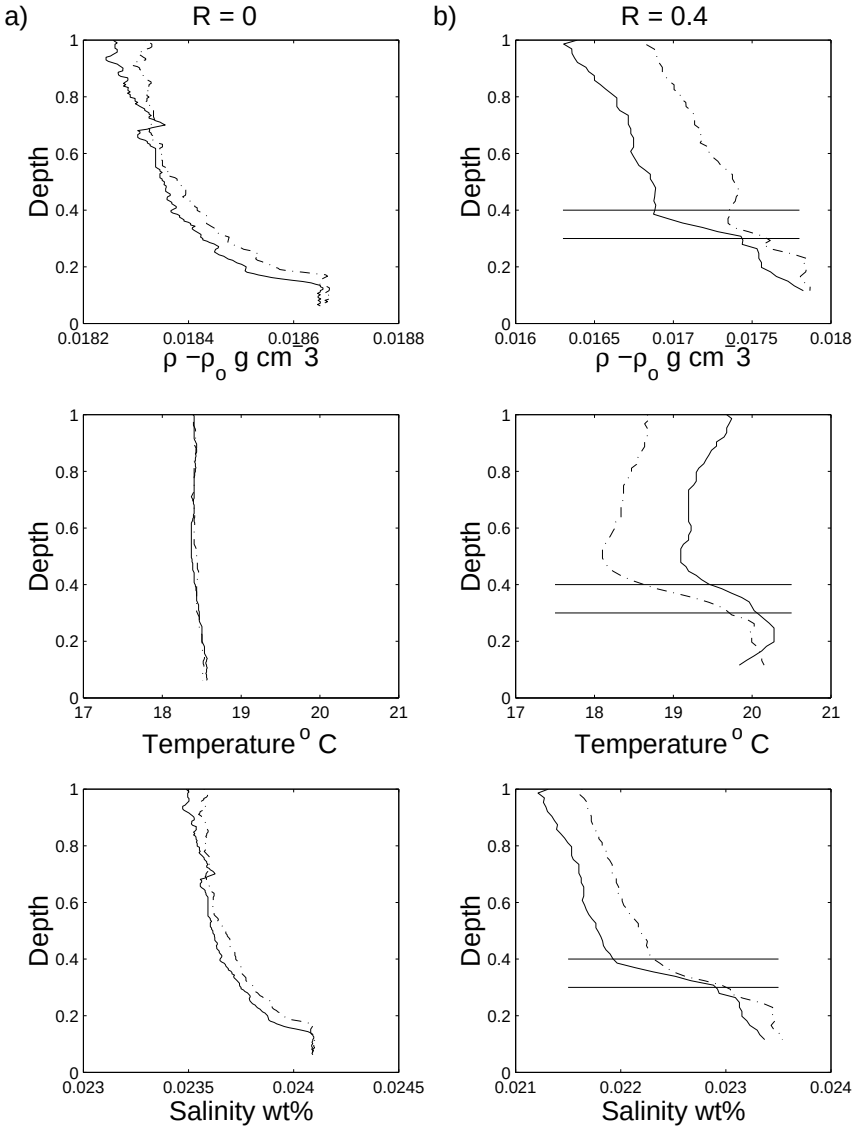

Figure 2.4: Measured density, temperature and salinity profiles at two successive times for; (a) $R = 0$, a normal filling box and (b) buoyancy fluxes from the same boundary and $R = 0.4$. Profiles were taken 1 minute apart in (a) and 5 minutes apart in (b). The aspect ratio is 0.5 and the horizontal lines in the graph represent upper and lower limits to the depths of convection measured independently from the shadowgraph. In both cases the density is decreasing while the profile shape remains constant.

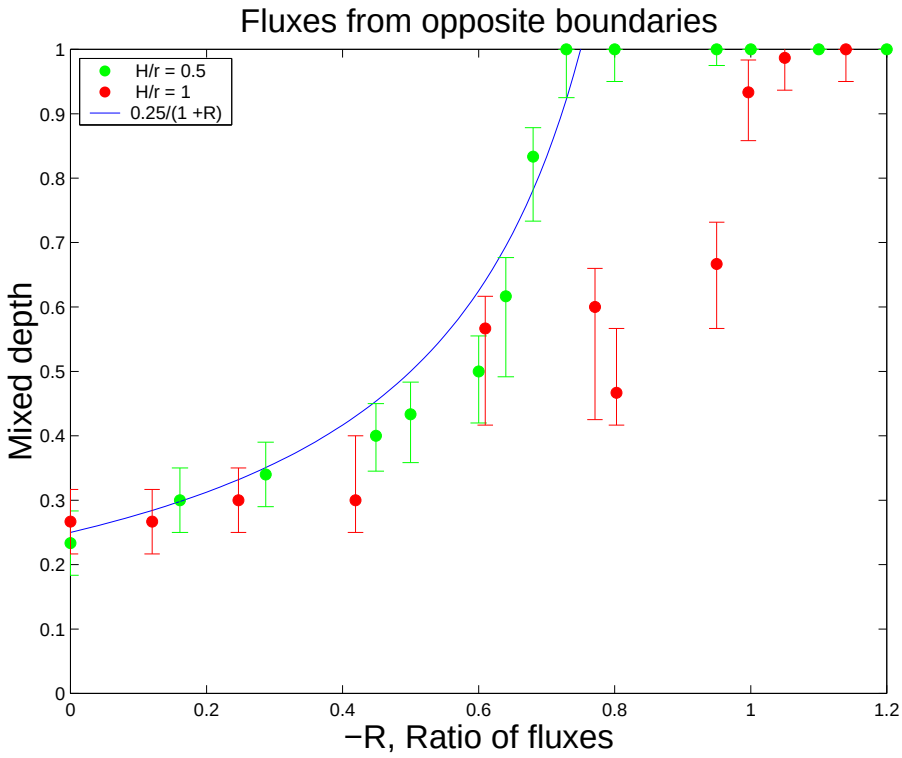

Figure 2.5: A comparison of experimental results and theory (2.17) for the steady state mixed depth when the sources are on opposite boundaries, for aspect ratios of 0.5 and 1. We see that full depth mixing occurs for $R \approx 1$ when $H/r = 1$ and at $R \approx 0.7$ when $H/r = 1/2$.

2.5 Experimental results for fluxes from opposite boundaries

When the plume was dense and descended from the top boundary, the basal heating increased the thickness of the well mixed outflow layer. The mixed depth was measured from shadowgraphs which reveal the maximum turbulent outflow depth. The results are plotted in figure 2.5 and agree with the theoretical prediction of (2.17) for small R. For magnitudes of R greater than about -0.4 we do not expect the theory to agree well with experiment, and the apparent agreement is despite the expected inertial recirculation driven by the plume (Baines & Turner, 1969; Barnett, 1991). For the small aspect ratio full tank mixing does not occur until $R = -1$ when there is no longer any stabilizing input to the tank.

Measurements of the temperature, salinity and density profiles provide additional information. For the case of $R = 0$ we see in figure 2.6 (a) that the temperature profile was uniform and the salinity distribution produced by the plume was solely responsible for the density changes.

The profile was a constant shape between successive measurements while increasing linearly in density at every point. At the base the water was well mixed by turbulence to a normalized depth of 0.25 in agreement with the shadowgraph observations.

When the experiment was repeated with heating, both temperature and salt gradients developed and the mixed depth increased. Since the density gradients due to both temperature and salinity are produced by the plume recirculation they have exactly the same shape, but the temperature profile is destabilizing while that of salinity is stabilizing. Profiles for $R = -0.4$ are shown in figure 2.6 (b) where the mixed layer depth has increased to $\zeta = 0.4$. Because the temperature profile is destabilizing the overall density gradient was reduced by a factor $(1+R)$ below that in the simple "filling box" process. When R = -1 the buoyancy fluxes were equal and opposite and the whole tank was well-mixed, giving uniform property profiles.

Double-diffusive effects were seen in the experiments only when $R < -0.7$. These took the form of up to 3 diffusive layers which developed above the well-mixed layer. Similar layers have been observed for a double-diffusive plume (and single buoyancy source) (McDougall, 1983). While the layers did not appear to significantly influence the overall density distribution, they did make it more difficult to distinguish the top of the well-mixed layer.

2.6 Geophysical applications

The density structure of enclosed seas may, in part, represent the partially-mixed result of competition between the tendency for deep localized convection to stratify the water column by the "filling box" process on the one hand, and the maintenance of a surface mixed layer on the other. As our model is more general than for just the point source plume studied, the same result should hold if the localized buoyancy production is periodic but with the same total buoyancy flux when integrated over each cycle (Baines & Turner, 1969; Killworth, & Turner 1982).

Addition of rotation to the problem is expected to make only small quantitative differences to the long term density profile and vertical advection of this very large "filling box". This is shown by Pierce & Rhines (1996) who experimentally found that for low rotation a turbulent plume generates the same density gradient as in the non-rotating filling box. Thus while we do not find point sources in nature, we do find periodic isolated sources of deep convection so

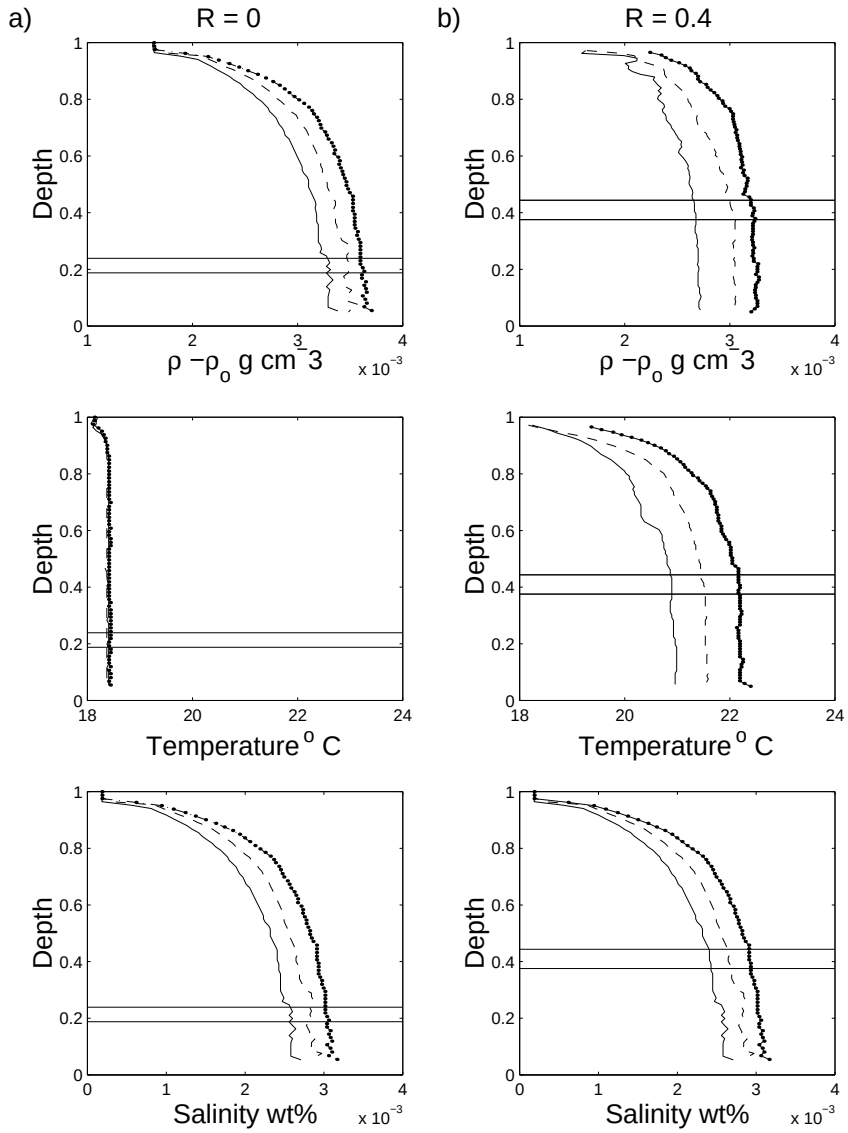

Figure 2.6: Measured density, temperature and salinity profiles at three successive times for (a) $R = 0$; since there is no heating the temperature is constant (except for small amount of surface cooling). In (b) $R = -0.4$ and the temperature profile is the same shape as the salinity profile. The normalized mixed-layer depth is in this case 0.41 which agrees well with independent shadowgraph measurements, where the upper and lower limits of this measurement are shown by the horizontal lines. Profiles were taken 5 minutes apart in (a) and 10 minutes apart in (b). In both cases the density is increasing while the profile shape remains constant.

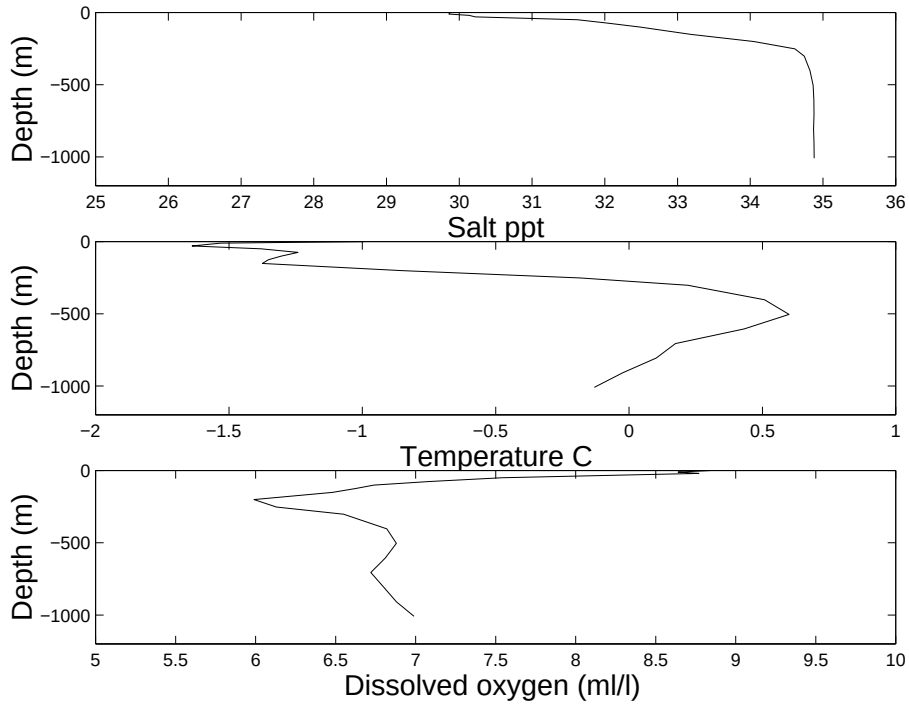

Figure 2.7: Measurements of density, temperature and oxygen profiles taken in the the Bering Sea, from the Levitus oceanographic data set (Levitus, 1987).

expect our study to be indicative of processes in the ocean.

Profiles in high latitude seas such as that from the Bering Sea, shown in figure 2.7, reveal a characteristic temperature profile with a maximum beneath the mixed layer, in the same way that our 'upside down' experiments show a minimum temperature above the mixed layer. The concentration profile of dissolved oxygen (an indication of how long the water body has been away from the surface) shows a minimum below the mixed surface layer and a maximum at greater depths. Both of these effects are consistent with the circulation and stratification produced by the combined effects of deep plume-like convection and a widespread surface buoyancy flux. The weak stratification apparent within the surface layer may be a result of other factors, such as an input of fresh water at the surface from melting ice and precipitation or lateral advection of water masses. Since this sea, like most others, is not isolated from the oceans, lateral advection will lead to intrusions of warmer water into the colder Bering Sea. It is this lateral advection that is the means by which the sea can maintain steady long-term properties rather than continue to decrease in density as do our confined 'upside down' laboratory experiments.

2.7 Conclusions

When there is a uniform buoyancy flux through the horizontal boundary at which the plume source is located, we have shown that the long-time steady state of the finite chamber may be a partially mixed and partially stratified one, a wholly stratified one or a completely mixed one, depending on the ratio of the two buoyancy fluxes. The partially-mixed state involves a convecting layer whose depth adjusts until the rate of encroachment into the stratification is equal and opposite to the vertical advection driven by the plume "filling box" process. For flux ratios $0 < R < 1$ the normalized mixed layer depth, $\zeta_{mixed} = (h + \Delta h)/H$, is $\zeta_{mixed} = (1.2 + 1.31Ri^{-1})\, 3E^*\, R/(1+R)$, where E^* is a mixing efficiency defined by Manins & Turner (1977) and Ri is the Richardson number of the convecting layer. For $R = 0$ the whole tank is stratified apart from the turbulent outflow from the plume and for $R > 1$ the whole of the water column is convectively stirred. Profiles in the stratified layer had the same form as in the "filling-box" theory of Baines & Turner (1969). Entrainment of buoyancy (heat) from the mixed layer resulted in the production of a temperature minimum (in our case with bottom heating) just above the convectively mixed layer. The transition between the well mixed region and the stratified region has an appreciable thickness, which increases as the aspect ratio increases so in tanks having large aspect ratios overturning occurred for $R < 1$.

In a possible oceanographic application of these results, concurrent widespread surface cooling or salt input due to freezing or evaporation on the one hand and deep convection due to a localized buoyancy flux on the other, are predicted to lead to a steady-surface mixed-layer depth. The results apply equally to the cases where there is a line source or a periodic source of buoyancy in competition with a steady distributed source, as the relationships between vertical plume advection and the density gradient are the same.

When the two buoyancy fluxes were released from opposite boundaries a steady mixed depth was again observed. However, the balance of vertical advection and enchroachment, processes which now act in the same direction, could not occur. A dynamic balance applies instead. Since the fluxes were introduced at opposite boundaries, the distributed boundary flux must be added to the outflow from the turbulent plume, resulting in a "filling box" density gradient proportional to the difference between the fluxes. Thus the gradient is a factor of $(1+R)$ smaller than that which would be generated by the plume alone. The reduced gradient is

stable only for $R > -1$ whereas for $R < -1$ the whole tank overturns. For $R > -1$ a mixed layer forms due to the turbulent kinetic energy of the plume outflow, and has a depth determined by the extent to which the turbulent kinetic energy is able to mix the stabilizing density gradient. The mixed layer depth in this case again increases as $|R|$ increases. This situation may possibly occur in the Earth's liquid outer-core, where it has been suggested (Fearn *et al.*, 1981; Fearn *et al.*, 1981; Whaler, 1980) that plumes of less dense residual melt may be released from the solidification front at the bottom of the outer core, potentially leading to density stratification of the outer core. The relatively uniform heat flux from the core to the base of the solid mantle provides a destabilizing buoyancy flux from the top and must tend to overturn the core. If isolated plumes do exist in the core (and we doubt this because they seem likely to have azimuthal spacings much smaller than the depth of the outer core) then our results would imply that the system should be completely mixed if the total buoyancy flux from the inner core - outer core boundary is less than the total buoyancy flux due to cooling from the top of the core ($R < -1$). On the other hand, the outer core could be partially stratified with a convecting layer of normalized depth $\zeta \approx 0.25/(1+R)$ at the top if the cooling to the mantle provides a lesser buoyancy flux ($R > -1$).

Chapter 3

Stratification produced by surface cooling in lakes with significant shallow regions

In this chapter, results of chapter 2 are applied to understand field observations of steady stratification that forms due to prolonged surface cooling when a large area of a reservoir is relatively shallow. We start by reviewing previous experimental studies of the formation of dense gravity currents by cooling a shallow side arm of a reservoir. The initial timescales for these gravity currents to fill a deep basin with a stratification are then discussed in § 3.1.1. By considering the input of buoyancy into control volumes for the deep stratified layer and surface convective layer a predicted equilibrium mixed layer depth is derived in terms of the bathymetry of the reservoir in § 3.1.2. The predicted mixed layer depth is then compared with a laboratory experiment in § 3.2.3 and with field observations of winter stratification in a medium-sized reservoir in § 3.3. Conclusions are then presented on the application of this theory to predicting the existence of winter stratification based on reservoir bathymetry and surface cooling.

3.1 Theoretical background

We consider the circulation and stratification of a simple reservoir with the bathymetry shown in figure 3.1 in which a uniform surface heat flux, $\tilde{H}$, drives the negative surface buoyancy flux, $B = g\alpha\tilde{H}/\rho c_P$. Negative fluxes represent heat lost from the water to the atmosphere. Cooling of the shallow sidearm leads to a dense gravity current, analogous to the buoyant

plume in chapter 2. Away from the shallow sidearm, surface cooling will result in a well mixed layer so that the stratification results from competition between the stratifying gravity current and the distributed surface cooling.

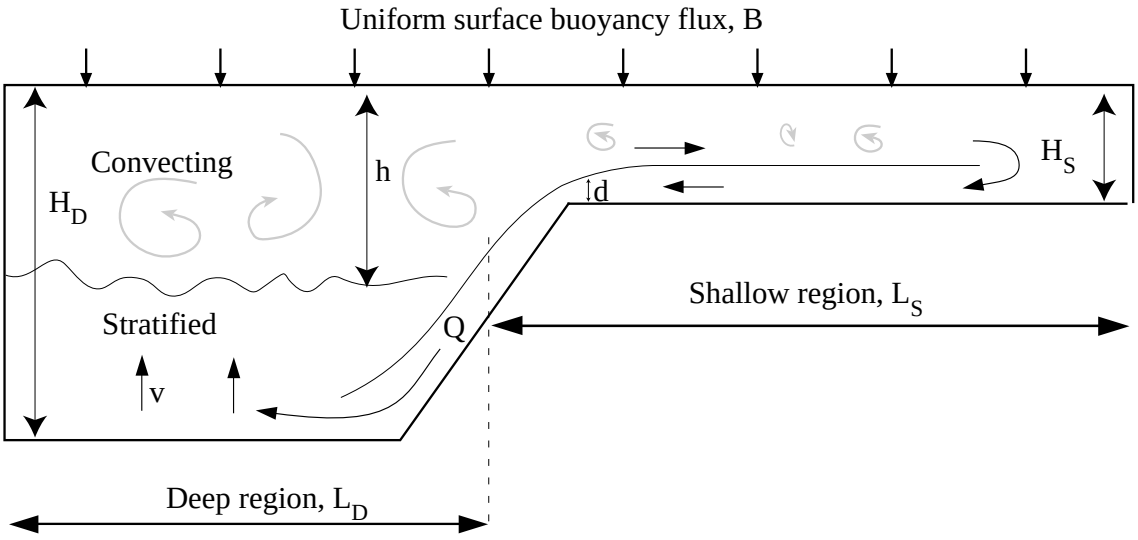

Figure 3.1: A uniform destabilizing buoyancy flux per unit area B is applied to the surface of a reservoir with a deep region of length L_D, depth H_D, and width W_D, and a shallow side arm of length L_S and depth H_S, and width W_S. The shallow region cools rapidly and produces a gravity current of initial thickness d and volume flux Q. The gravity current fills the deep region with cold dense fluid and causes a general upwelling with velocity v. Near the surface of the deep region there is a convecting layer of depth h.

3.1.1 Convective circulation timescales

Surface cooling on the shallow sidearm of a reservoir results in horizontal density gradients that drive the formation of a dense cold gravity current. In laboratory studies of such cooling, Sturman & Ivey (1998) found that there was an initial period of disorganized overturning convection before horizontal density gradients started to drive a dense gravity current. This timescale, $\tau_{initial}$, was found by Finnigan & Ivey (1999) to depend upon the length of the shallow region L_S, the buoyancy flux B, and the ratio of the thickness of the gravity current d, to the depth of the shallow region H_S, as

$$\tau_{initial} \sim L_S^{2/3} B^{-1/3} \left(1 - d/H_S\right)^{-1}. \tag{3.1}$$

Experimental observations of d/H_S by Finnigan & Ivey (1999) and Grimm & Maxworthy

(1999) found values in the range d/H_S = 0.25 - 0.33. This suggests that exchange occurs at a rate less than the theoretical maximum of d/H_S = 0.36, predicted by Armi (1986).

The steady volume flux per unit width of the gravity current was found by Sturman & Ivey (1998) to vary as

$$\frac{Q}{W_S} = 0.2(BL_S)^{1/3}H_S, \tag{3.2}$$

where Q is the volume flux of the gravity current and W_S is the width of the shallow region. Finnigan & Ivey (1999) and Grimm & Maxworthy (1999) found similar expressions for the volume flux but with slightly different experimental constants. The timescale for the gravity current to fill the whole of the deep region of volume $V_D = W_D L_D H_D$ then becomes,

$$\tau_{flush} = \frac{V_D}{Q} = 5L_D\, B^{-1/3}\, L_S^{-1/3}\, \frac{H_D}{H_S}. \tag{3.3}$$

The steady circulation sketched in figure 3.1 can only become established if the duration of surface forcing is longer than both $\tau_{initial}$ and τ_{flush}.

3.1.2 Steady convective layer depth

We consider control volumes for the surface mixed layer of constant depth h and a deep stratified layer of thickness $(H_D - h)$. Both layers have the same area $A_D = L_D W_D$. The discharge of the gravity current provides a buoyancy flux from the shallow to the deep region which is exactly balanced by a surface return flow from the deep to the shallow region.

If the convective layer depth, h, is to remain constant, then the rate at which the gravity current forces the interface to upwell, v, must balance the rate at which penetrative convection causes the surface layer to deepen, $U = dh/dt$, (defined in 2.2). This requires that the density difference between the two layers remains constant, so the density of both layers changes at the same rate.

The rate at which the density of both layers increases must equal the rate of density increase of the entire system. This is due solely to the surface buoyancy flux applied across both deep and shallow areas

$$\frac{d\rho}{dt} = \frac{\rho_o B(A_D + A_S)}{g(A_D H_D + A_S H_S)}, \tag{3.4}$$

where the total surface area is $(A_D + A_S)$, the total volume is $(A_D H_D + A_S H_S)$, g is the gravitational acceleration and ρ_0 is a reference density. Within the stratified layer $d\rho/dt$ must balance the induced upwelling velocity, v, of the density gradient, as defined by (2.3). Using (2.3) and (3.4) the upwelling velocity is equivalent to

$$v = \frac{B(A_D + A_S)}{N^2(A_D H_D + A_S H_S)}. \tag{3.5}$$

Equating the interface entrainment rate (2.2) with the upwelling velocity of the density gradient gives

$$\zeta \equiv \frac{h}{H_D} = 3E^* \frac{R+P}{R+1}, \tag{3.6}$$

where $\zeta = h/H_D$ is the normalized mixed-layer depth and

$$P = H_S/H_D, \tag{3.7}$$

is the ratio of the shallow and deep region depths, and

$$R = A_D/A_S, \tag{3.8}$$

is the ratio of the deep and shallow areas. As the discussion of R concerns the relative strengths of the gravity current to the surface convection, it has the same interpretation as the parameter defined by (1.1).

The mixed layer penetrates to full depth of the deep region ($\zeta = 1$), as R becomes very large. When $P = 0$ the normalized mixed-layer depth ζ is essentially the same as defined by (2.6) in chapter 2.

3.2 Laboratory experiments

3.2.1 Methods

An extensive series of laboratory experiments were performed to test the dependence of the normalized mixed layer depth ζ upon P and R, as in equation (3.6). The apparatus used was a rectangular tank 1.2 m long $\times$ 0.2 m wide $\times$ 0.4 m deep with geometry as shown in

figure 3.1. The base was made of copper and the side walls were insulated with 15 mm of polystyrene foam. Rather than provide cooling from the upper surface we found it easier to invert the whole setup and heat from the base using two electric heat pads that allowed the deep and shallow regions to be heated independently. Before each experiment, the tank was filled with fresh water at the laboratory temperature. The heat flux was then started over the base of the whole tank. The buoyancy flux was the same in all experiments and had a value of 1.2×10^{-5} m^2 s^{-3}.

The ratio of shallow and deep areas, R, was varied by changing the relative length of the deep and shallow regions. The slope region between the shallow and deep regions occupies about 10 cm, as shown in figure 3.2. The lengths L_S and L_D are measured to the halfway position of this sloping region. In initial experiments the deep region had H_D = 280 mm. The shallow region had a depth of H_S = 40 mm. Later experiments systematically varied the ratio $P = H_S/H_D$.

To determine the flushing timescale of the deep region, as defined by (3.3), one experiment was conducted with R = 1 and P = 1/5 where only the shallow region was heated. A gravity current formed that stratified the whole of the deep region after 12 minutes, in agreement with (3.3). All experiments were run for at least twice this time to ensure a steady balance in the convective depth.

3.2.2 Development of the circulation

Immediately after the initiation of heating, thermals formed in the deep region and initially mixed the whole depth of the water column. After 3 - 5 minutes horizontal temperature differences were set up between the deep and shallow areas and a gravity current started to stratify the deep region. The timescale for the initiation of the gravity current was consistent with (3.1). After approximately 12 minutes the thermals in the deep region were influenced by the stratification and no longer penetrated the full depth of the deep region and by about 15 minutes the upwelling of the deep region had forced the interface to the steady depth given by (3.6).

In some experiments heating was commenced in the shallow region 20 minutes before it commenced in the deep region in order to establish a strong stratification. The surface convection subsequently eroded the stratification within 15 minutes and the same steady state

was attained. Similarly, when the heating was turned off so that the circulation stopped, the circulation was re-established 5 minutes after the heating restarted, consistent with (3.1).

To visualize the circulation in the experiments, food dye was added to the water in the shallow and deep regions. Experimental photographs are shown in figure 3.2, where the images are inverted so that they appear to be cooled from the surface as in figure 3.1. The well mixed surface layer can be seen in figure 3.2 (a) where red dye is transported by thermals to an average depth h, marked by a horizontal line. The dense gravity current can be seen in figure 3.2 (b) where blue dye had been added to the shallow region. The blue dye was subsequently observed to fill the deep region and further input of dense fluid by the gravity current advected the blue dye into the well mixed surface layer.

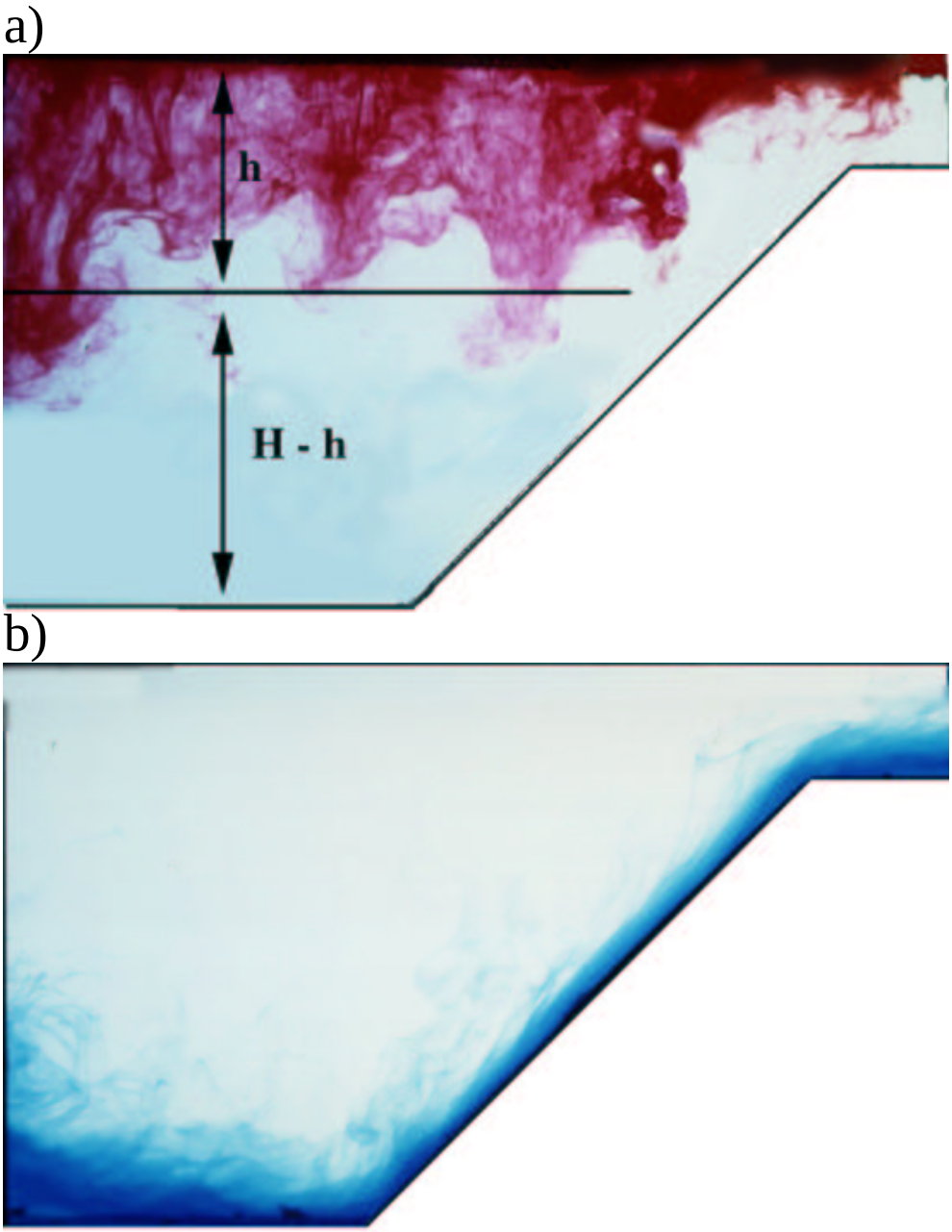

Figure 3.2: Photographs showing the circulation of dye in an experiment where $R = 0.5$. In (a) red dye is placed into the convecting layer of depth h. In (b) blue dye is placed in the gravity current.

3.2.3 Results

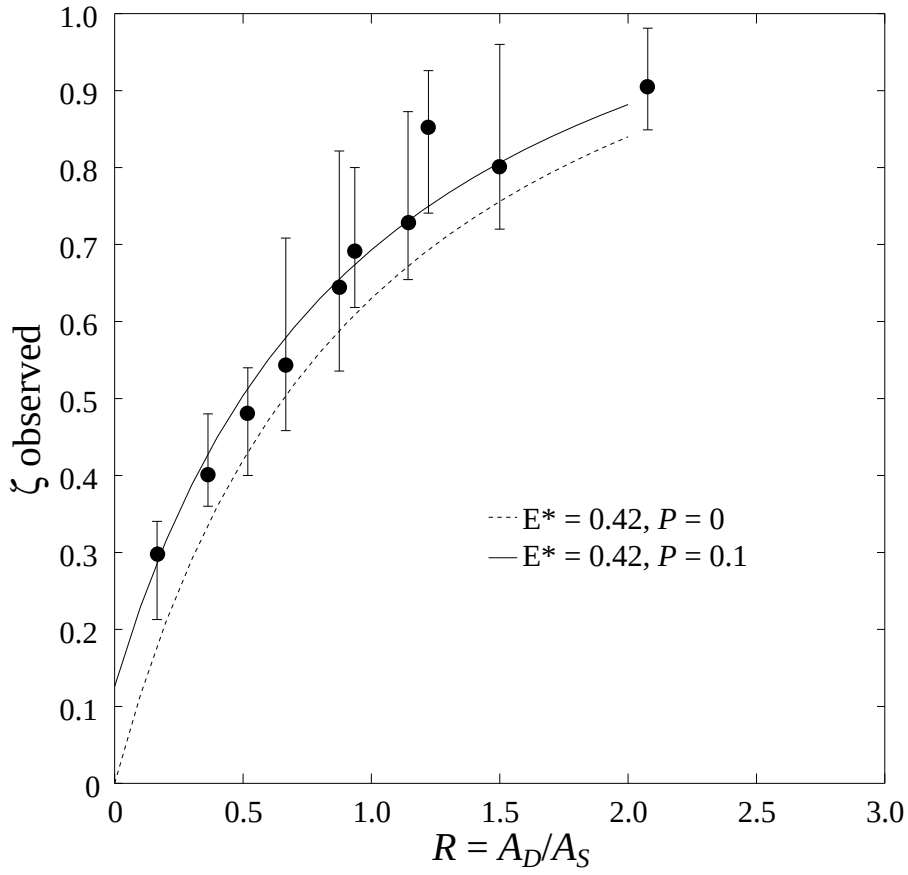

Figure 3.3: Experimental results of the normalized convecting layer depth ζ as a function of R, the ratio of deep to shallow areas. The theoretical result of (3.6) is shown as the curves for P = 0.1 (solid) and P = 0 (dotted) and agrees well with data.

Two sets of experiments were conducted. The first tested the dependence of the surface mixed layer depth upon the relative surface areas of shallow and deep regions, as described by (3.6). The thickness of the convecting region was estimated visually by injecting dye into the layer, as shown in figure 3.2 (a). In these experiments the shallow depth was at most 1/5 of the deep layer depth, i.e. $P = H_S/H_D \leq 0.2$. The experimental data is is plotted in figure 3.3 and is in good agreement with theory (3.6), and we see that for $R > 2$ the whole depth is essentially well mixed.

The size of the error bars reflects the thickness of the interface, as described in §2.1.2. In all experiments the maximum interface thickness was $\Delta h = 0.2\ h$ consistent with large Ri_g (as defined by 2.12). The observed interface thickness ζ in figure 3.3 is smaller than in the

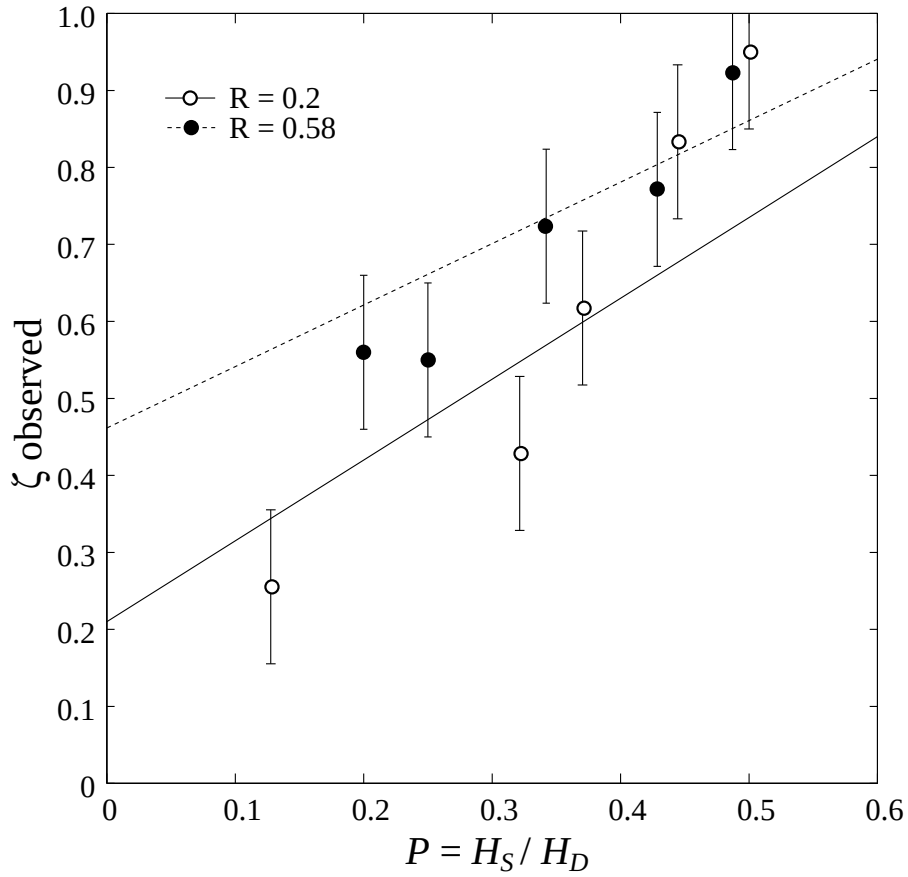

Figure 3.4: Experimental measurements of the normalized convecting layer depth ζ as a function of the ratio of shallow to deep depths, $P = H_S/H_D$, for a given area ratio R. The theoretical result of (3.6) is shown as the curves for $R = 0.2$ (solid) and $R = 0.58$ (dotted), with $E^* = 0.42$.

experiments shown in figure 2.3. This is because the gravity current entrains less fluid than a plume from a point source for the same buoyancy flux (Ellison & Turner 1959), so will produce a stronger density gradient in the stratified region. This resulted in the persistence of stratification beneath the well mixed layer until $R \approx 2$ in figure 3.3, as opposed to $R \approx 1$ in figure 2.3.

The second set of experiments studied the dependence of the normalized mixed layer depth ζ, upon the depth ratio $P = H_S/H_D$, for a given area ratio R. Experimental results are shown in figure 3.4, and ζ can be seen to increase with P. Theoretical values of ζ given by (3.6) are plotted for $R = 0.2$ and $R = 0.58$. When P increased above 0.5, the whole deep region was well mixed by an overturning cell driven by the surface convection. This experimental result shows that the shallow sidearm must be less than half the depth of the deep region ($H_S/H_D < 0.5$) if

the gravity current is to produce a significant stratification in the deep region.

3.3 Field experiment

3.3.1 Site description and methods

Chaffey reservoir is located in northeastern New South Wales, Australia (31°21′ S, 151°8′ E) approximately 32 km southeast of Tamworth at an elevation of 519 m above sea level. When full the reservoir has a capacity of 62,000 ML, a surface area of 542 hectares, a maximum depth of 28 m and a mean depth of 11.4 m. A drought during 1994-1995 led to a drop in reservoir level to 506 m above sea level, equivalent to approximately 20% of capacity, by the beginning of winter, i.e. June 1995. Subsequent inflows increased the level to 512.3 m above sea level ($\sim$ 53% capacity) by winter 1996 and to 518.3 m above sea level ($\sim$ 93% capacity) by winter 1997. The water level was constant to within ± 0.1 m throughout each winter.

The reservoir has a deep region extending from roughly the 502 m contour in the south and west to the dam wall at the northeastern corner. To the south, the broad shallow region between the 502 and 506 m contours spans the drowned channel of the Peel River (figure 3.5), the only major source of inflow.

Monitoring of the reservoir took place from February 1995 through November 1997 by a team of scientists, led by Dr Brad Sherman (CSIRO). Meteorological (air temperature, relative humidity, emission or absorption of long wave and short wave radiation, wind speed and direction) and thermistor chain data were collected 200 m northeast of Stn 1 (figure 3.5). The instruments were sampled every 10 seconds and recorded as 10 minute averages from September 1995 to November 1997. Weekly conductivity-temperature-depth-dissolved oxygen (CTDO) profiles with a spatial resolution of 0.25 m were measured in the early morning at 5 - 6 sites (see figure 3.5) depending on water level using a Seabird Electronics SBE-19 profiler. The sixth site, Stn 3, was located 3 km upstream (2.5 km SSE) of Stn 2 (not shown in figure 3.5) and was only sampled in winter 1997 when the reservoir was nearly full. Full details of the measurement program are given in Sherman *et al.* (2000).

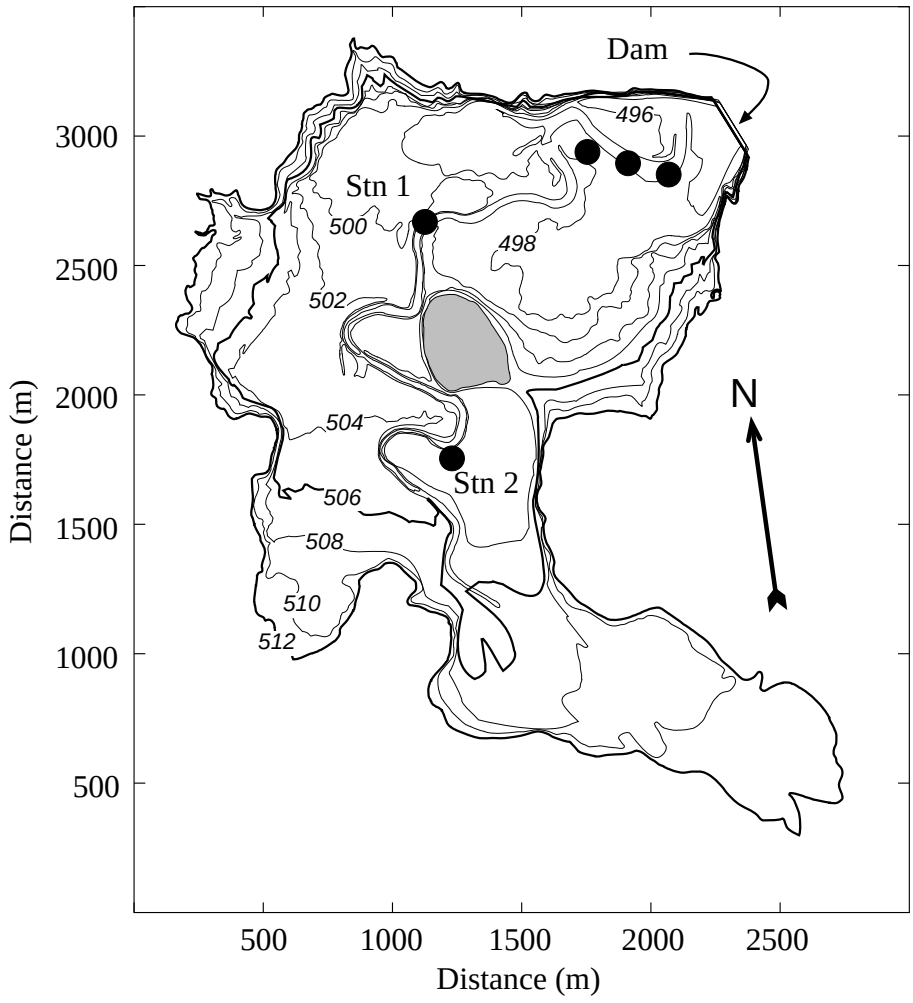

Figure 3.5: Bathymetry of Chaffey reservoir. The elevation above sea level is in m with contours at 2 m intervals. Filled circles denote locations of the weekly CTDO casts. Meteorological station and thermistor chain were located at Stn 1. Reservoir levels were 506.6 and 512.3 m above sea level during the winters of 1995 and 1996, respectively. The drowned river channel is evident along the west side of the island. Figure plotted with data collected by Dr Brad Sherman.

3.3.2 Calculations

The surface heat flux, $\tilde{H}$, was computed by Sherman *et al.* (2000) as the sum of the turbulent sensible and latent heat fluxes plus the net emission or absorption of long wave and short wave radiation. Turbulent heat, mass, and momentum fluxes, adjusted for atmospheric stability, were computed using the air temperature, relative humidity, wind speed and water surface temperature (0.10 m depth) data following Liu *et al.* (1979). The velocity scale of the eddies in the convective layer, w^*, was computed using (2.13) and observed values of h and $\tilde{H}$ with the buoyancy flux, $B = g\alpha\tilde{H}/\rho c_P$, determined by the surface heat flux.

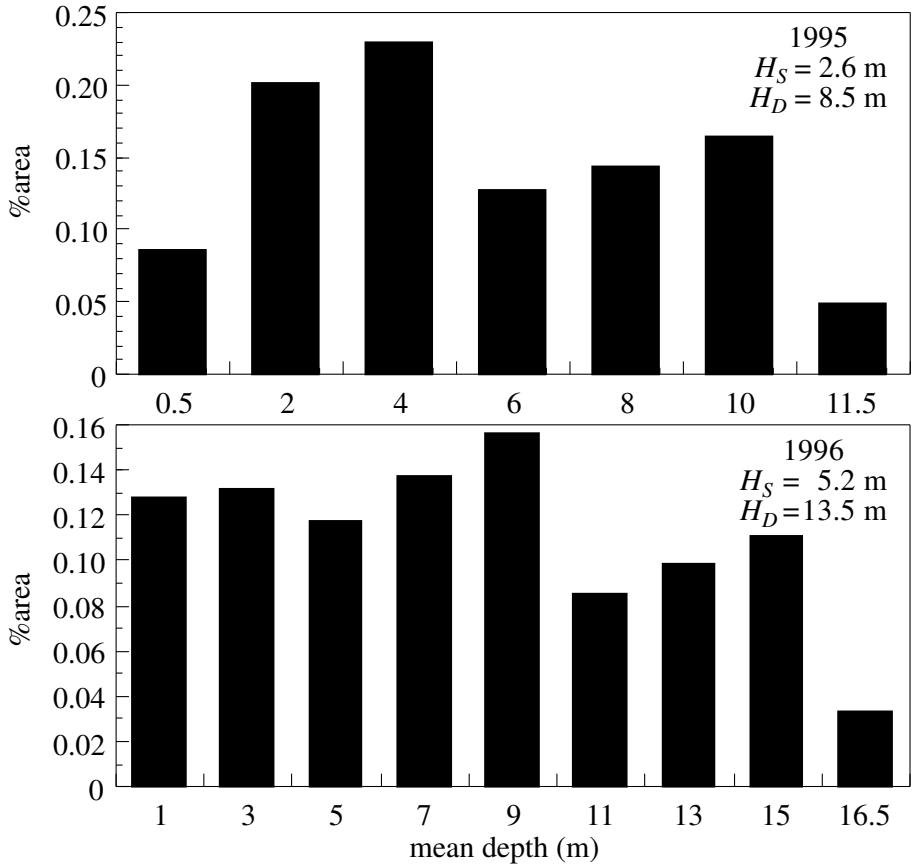

Figure 3.6: Depth distributions and areally weighted mean depths of the shallow, H_S, and deep, H_D, regions in Chaffey reservoir during 1995 and 1996. Peaks in the distribution occur at 4 and 9 m depth in 1995 and 1996, respectively. R = 0.93 during 1995 and 0.49 in 1996.

The predicted value of the normalized convective layer depth, ζ, can be computed from the field data using (3.6). This required that R and P be determined from the bathymetry of Chaffey reservoir, as shown in figure 3.5. The boundary between deep and shallow areas was assumed

to correspond to the largest peak in the frequency distribution of reservoir depths (figure 3.6). This occurred at roughly the 502 m contour during both years. Areal mean depths, H_S and H_D, were then computed for the shallow and deep regions from the frequency distribution data. The efficiency of the convective deepening process, E^*, is expected to be within the range 0.36 to 0.43 for the range of Ri_g experienced in the field, as described by (2.7) and (2.8).

3.4 Field experiment results

3.4.1 Meteorology, heat fluxes

Sherman *et al.* (2000) found that during winter 1996 (1 June - 22 Jul), the average daily net heat flux from the reservoir was -27 $W\mathrm{m}^{-2}$ comprising sensible, latent, and radiative (short wave + long wave) fluxes of -22, -43, and + 38 $W\mathrm{m}^{-2}$, respectively. The mean daily wind speed was 2.2 ms^{-1}. When just the main cooling period is considered, i.e. between 1800 h and 0600 h, the corresponding fluxes were -29, -45, and -66 $W\mathrm{m}^{-2}$. The typical night time cooling flux driving the circulation was therefore -140 $W\mathrm{m}^{-2}$ ($B = 3.7 \times 10^8$ m^2 s^{-3}) whereas during the day there was a net flux of heat into the water. The field experiment is analogous to the laboratory experiments but with the constant boundary heat flux replaced by a periodic flux of approximately -140 $W\mathrm{m}^{-2}$.

The periodic nature of the reservoir heat flux is shown in figure 3.7 (a) and thermistor chain data for the temperatures of the surface mixed layer and at a depth of 14 m are shown in figure 3.7 (b). The signature of the cold gravity current is particularly noticeable on 9, 12 and 18 June 96 when the temperature at 14 m continued to decrease long after the surface layer had started to heat up. Episodes of cooling were of 7 to 8 days duration and were defined by periods when the 24 hour moving mean net heat flux was negative.

Meteorological data were not available for 1995, but 1997 data showed a 10% greater rate of heat loss than occurred in 1996. A 10% change in the heat flux changes the computed timescales of (3.1) and (3.3) by less than 5% and has no effect on the determination of ζ. Therefore, we assume the same heat flux for both 1995 and 1996 to facilitate comparison of results between years.

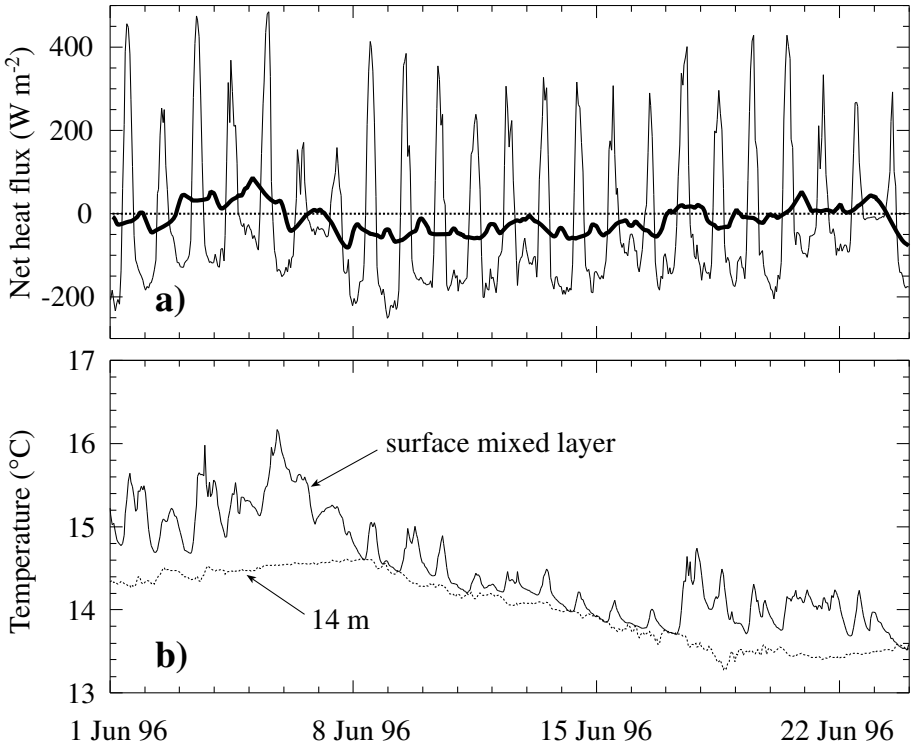

Figure 3.7: (a) Net heat flux into Chaffey reservoir during 1-21 June 1996. Negative values indicate heat loss from the reservoir. The bold line is the 24 hour moving mean. (b) Thermistor chain data from near Stn 1 showing water temperature in the surface mixed layer (solid line) and at 14 m depth (dashed line). Figure plotted with data collected by Dr Brad Sherman.

3.4.2 Stratification

Temperature profiles at Stn 1 in Chaffey reservoir for the winters of 1995 and 1996 are shown in figure 3.8. As each winter progressed the temperature decreased everywhere throughout the water column while at the same time the water column remained stratified with a sharp interface located 4.5-5 m above the bottom due to the presence of a cold intrusion. At no time during either winter was an isothermal water column observed. The time variation in the surface forcing can be seen in the temperature profile of 20 June 95 where a significant cooling event has produced a very cold intrusion in the deep region that is removed by thermal diffusion and subsequent intrusions. The temperature profile shapes are very similar to the equivalent density profiles shown in figure 2.6 when $R = 0.4$.

From visual inspection of figure 3.8 the convecting layer depth h, is 6.5 and 12 m during 1995 and 1996, respectively. Profiles measured at the three locations close to the dam wall

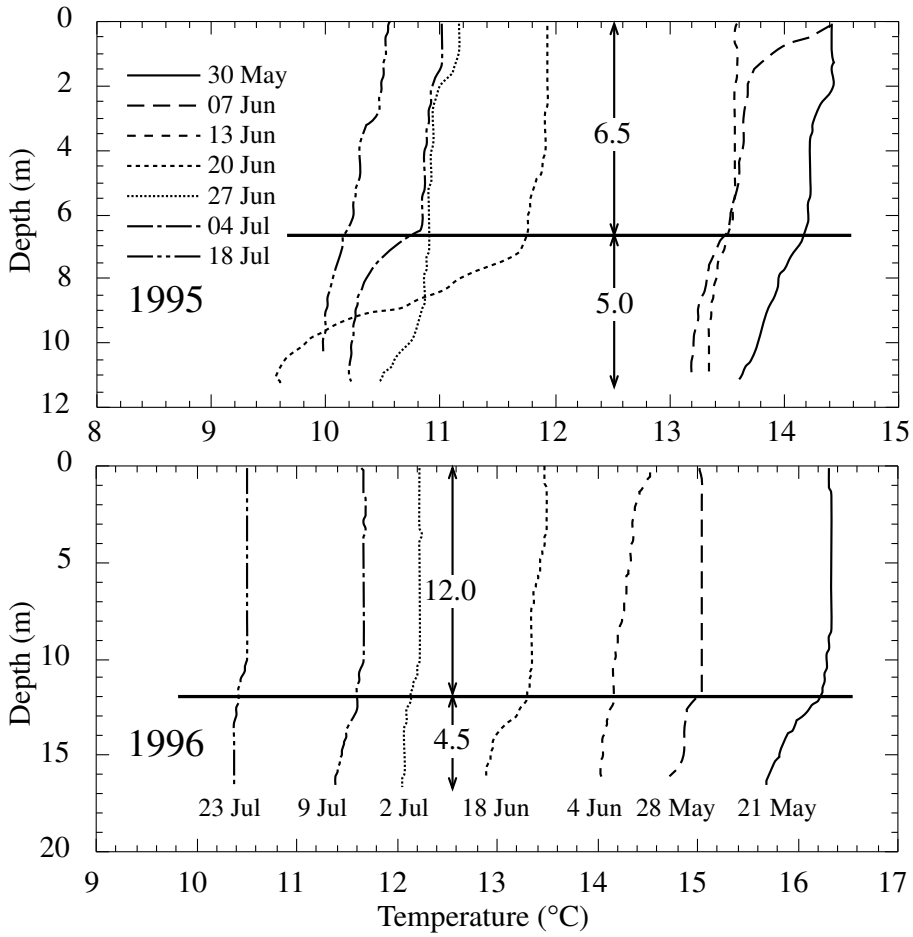

Figure 3.8: Temperature profiles from CTDO casts taken at Stn 1 during the winters of 1995 (top) and 1996 (bottom). The horizontal line indicates the boundary between the convecting region near the surface and the stratified region near the bottom caused by the intrusion of cold water. Arrows indicate the thicknesses of the two regions. Figure plotted with data collected by Dr Brad Sherman.

confirmed the location of the interface at this depth.

3.4.3 Normalized convective layer depth and circulation timescales

Using the field data we can compute the expected normalized convective layer depth using (3.6) and the timescales for the initial set up of the circulation $\tau_{initial}$, defined by (3.1), and for the filling of the deep region τ_{flush}, defined by (3.3).

During winter 1995 the areal mean depths of shallow and deep regions, H_S and H_D, were 2.6 m and 8.5 m, respectively, and the shallow region accounted for 52% of the reservoir's surface area. This gives R = 0.93 and P = 0.31. Using these values in (3.6), predicts that the

convective layer depth is ζ = 0.71 - 0.83, assuming a similar range as the experimental results. The observed convective region thickness was 6.5 m giving ζ_{obs} = 0.76. We approximate L_S = 1500 m and L_D = 1500 m, so that the timescales for the initial establishment of circulation and flushing the deep region are $\tau_{initial}$ = 15.9 hours and τ_{flush}= 7.6 days, consistent with the observations of Sherman *et al.* (2000) that the intrusion appeared to be replenished with colder water on a weekly basis.

Year	1995	1996
Deep region contour	502 m	502 m
Shallow region contour	506 m	512.3 m
h	6.5 m	12.0 m
L_S	1500 m	3000 m
L_D	1500 m	1500 m
H_D, areal mean	8.5 m	13.5 m
H_S, areal mean	2.6 m	5.2 m
$P = H_S/H_D$	0.31	0.38
A_D	48% (124 ha)	33% (129 ha)
A_S	52% (132 ha)	67% (265 ha)
$R = A_D/A_S$	0.93	0.49
B	$3.7 \times 10^{-8} m^2 s^{-3}$	$3.7 \times 10^{-8} m^2 s^{-3}$
Ri_g	10 - 80	20 - 160
Measured ζ	0.76	0.86
Predicted ζ	0.71 - 0.83	0.63 - 0.70
$\tau_{initial}$	15.4 hours	24.4 hours
τ_{flush}	7.4 days	4.7 days

Figure 3.9: A summary of field observations for 1995 and 1996 winters.

By winter 1996, the reservoir had filled to 512.3 m and the shallow region shifted significantly towards the southeast, as seen in figure 3.5. We approximate L_S = 3000 m, whereas the deep length was relatively unchanged at L_D = 1500 m. Areal mean depths for the shallow and deep regions were 5.2 and 13.5 m, respectively. With R = 0.49 and P = 0.38, we find theoretically ζ = 0.63 - 0.70, assuming a similar range as the experimental results The observed convective layer thickness was 12 m giving ζ_{obs} = 0.86. The circulation and flushing timescales are $\tau_{initial}$= 25.3 hours and τ_{flush}= 4.6 days. A summary of these results is included in table 3.9.

Agreement between the field data, theory, and the laboratory model is good for 1995 but poor for 1996. We believe the reason for the discrepancy relates to the way in which changes in

the geometry of the field situation interact with the timescales for the forcing and establishment of the convectively driven circulation.

Of particular significance is the periodic forcing in the field which varies from destabilizing to stabilizing buoyancy fluxes not only diurnally but also on weekly timescales associated with the movement of high and low pressure systems (figure 3.7 a). This timescale, $\tau_{atmosphere}$, is approximately 12 hours. If $\tau_{atmosphere} > \tau_{flush}$ we expect to see a steady normalized mixed layer of depth ζ as in the laboratory. If $\tau_{initial} < \tau_{atmosphere} < \tau_{flush}$ we expect to see a gravity current starting to stratify the deep region but probably with a deeper normalized mixed layer depth than the predicted ζ as steady state has not yet been reached. If $\tau_{initial} > \tau_{atmosphere}$, then the whole deep region would be well mixed and, although there may be horizontal density differences between deep and shallow regions, no significant gravity current would have time to form.

During 1995, $\tau_{initial}$ was about 16 hours, i.e. similar to $\tau_{atmosphere}$, and so the circulation in the shallow region had time to become established. In 1996, the shallow region was roughly twice as long as in 1995 ($\tau_{initial}$= 25 hours) and so the buoyancy flux was never applied long enough for the circulation to become fully established. This means that in 1996, ζ may not have reached the equilibrium described by (3.6) and is probably only due to the cold water of the shallow region flowing into the deep region after surface cooling had stopped.

Another factor that may contribute to a deeper than expected ζ in the field is the presence of a wind-generated shear stress at the water surface. At Chaffey reservoir, shear stress contributes about an additional 20% to the energy available to deepen the surface mixed layer during the winter. This amount is less than 15% of the energy required to explain the additional entrainment observed in the field. The insufficient duration of forcing must therefore be a far more significant contributor to the discrepancy in ζ than is wind mixing.

3.5 Conclusion

Stratification can occur in reservoirs during periods of winter cooling if the bathymetry can be characterized by distinct deep and shallow regions. If the ratio of the deep areas to the shallow areas of the lake is less than 1 and the ratio of the shallow depth to the deep depth is less than 0.5, then a mixed surface layer and a deep stratified region can develop.

These reservoirs might otherwise be expected to be well-mixed due to convective overturning. Should the cooling persist for at least one deep region filling timescale, τ_{flush}, (given by 3.3), then theory predicts that a steady state can exist in which the depth of the convecting layer normalized by the depth of the deep region, $\zeta = h/H_D$, is given by $\zeta = 3E^* (R+P)/(1+R)$ where R is the ratio of deep and shallow areas. Laboratory experiments presented here have confirmed this functional relationship.

The field data from Chaffey reservoir, has good agreement with theory for 1995 but poor agreement for 1996. The probable reason for this is that the timescale for the circulation to become fully established, which depends on the length of the shallow region, was close to the timescale of the forcing buoyancy flux during 1995 but much longer in 1996 when the shallow region extended much further.

The timescales for establishing the circulation in the shallow region and flushing the deep stratified region suggest that with a typical periodic destabilizing heat flux of $-140\ W\mathrm{m}^{-2}$, only reservoirs up to 2-3 km in length will be able to reach the steady circulation observed in the laboratory experiments. Larger reservoirs will still experience convective circulation, and possibly persistent winter stratification, but the theoretical predictions of the normalized convective layer depth presented here will not be applicable.

An interesting consequence of convectively driven circulation is the significant upwards advective transport in the deep region driven by the gravity current. Sherman *et al.* (2000) concluded that differential cooling was the second strongest vertical transport mechanism in Chaffey reservoir, behind only the circulation resulting from artificial destratification (by bubble plume injection) and between 2 to 20 times stronger than turbulent diffusion. They proposed also that the associated stratification was likely to be responsible for the frequent winter blooms of dinoflagellates and buoyant cyanobacteria that are more often associated with strongly stratified water columns during summer and autumn.

Chapter 4

Generation of density fine structure by salt fingers in a spatially periodic shear

In this chapter we discuss the interaction of salt fingers with a spatially varying shear. In § 4.1 we review previous experiments where salt fingers were present in shear. A model of the flux divergences caused by a spatially varying shear is developed in § 4.2. The steady state solutions are discussed in § 4.2.1 and compared with a numerical model in § 4.2.2. Observations from laboratory experiments are presented in § 4.3 and in § 4.4 we discuss the possible implications for an oceanographic setting.

4.1 Previous experiments

The effect of shear on laboratory salt fingers has been studied by Linden (1971) in the context of turbulent eddies impinging upon a density step where salt fingers were growing. Here the turbulence and salt fingers are spatially separated with turbulent entrainment occurring at the edges of the interface. The turbulent eddies provide a shearing motion that reduced the salt finger fluxes. In the ocean, on the other hand, shear is generated by internal inertial waves and by collapsing intermittent turbulence (Gregg, 1987) in vertical stratification that is often salt finger favourable. Tilting of fingers by shear was observed in some of the sharp interfaces of the Caribbean Sheets and Layers Transect (CSALT) experiment (Kunze *et al.*, 1987). St. Laurent & Schmitt (1999) report observations from the North Atlantic Tracer Release Experiment (NATRE) of optical structure in the form of near-horizontal laminae typically at $10° - 20°$ to

the horizontal.

For a density interface with hot salty water overlying relatively cold and fresh water stirred from beneath by an oscillating grid, Linden (1971) measured the fluxes of heat and salt as a function of stirring frequency ω and the ratio of temperature T and salinity S gradients defined as

$$R_\rho = \alpha T_z / \beta S_z, \tag{4.1}$$

where α is the coefficient of thermal expansion and β is the coefficient of saline contraction. There are two competing effects that can contribute to the fluxes of T and S across the interface: salt fingering and turbulent entrainment. When the eddies were weak, their main effect at the interface was to provide a shearing motion upon the growing fingers. Water in the fingers had a velocity U, and the turbulent eddies had an RMS velocity ΔV, and on average, it was found that the fingers in the thin interface were tilted at an angle from the vertical of

$$\theta = \tan^{-1}(\Delta V / U). \tag{4.2}$$

This result for a thin interface follows from the more general description that in a continuous uniform shear the angle that fingers will make to the vertical has the time dependence

$$\tan\theta = \tan\theta_o - \int_o^t \frac{\partial V}{\partial z} dt. \tag{4.3}$$

Since the fingers are buoyant rising and falling parcels of water (rather than passive tracers), one can derive (4.2) in the limit where the fingers have short length scales. The finger fluxes are reduced from the undisturbed flux F_o by

$$F_S = F_o \cos(\theta), \tag{4.4}$$

because of a change in the effective gravity. This result agrees well with the measurements of Linden (1971) for small $\Delta V/U$ when fingers are tilted up to 45° from the horizontal, but at larger $\Delta V/U$ the fluxes were dominated by turbulence.

When a large velocity difference ΔV is applied across a salt finger interface (such that the ratio $\Delta V/U$ is large), a different form of salt fingering convection can emerge (Linden, 1974):

vertical two-dimensional sheets form, aligned with the direction of the sheared flow. Theoretically, these two-dimensional sheets can have the same buoyancy fluxes as three-dimensional fingers.

Kunze (1990) used measurements of inertial wave shear in the main thermocline and typical values of salt fingering vertical velocities to conclude that most oceanic salt fingers should take the form of two-dimensional (2-D) sheets. He derived a dependence of the vertical finger velocity on the angle of the salt fingers, taking into account the action of viscosity and the reduced total wave number of the strained fingers. For large θ the flux is expected to be reduced as

$$F_S = F_o \cos^4(\theta). \tag{4.5}$$

The theoretical form of the shearing flux reduction by Kunze (1990) is consistent with the experimental results (4.2) in that the salt finger fluxes are reduced to zero as the salt fingers are tilted toward the horizontal. At present, there are no experimental data to test the predictions of flux reduction at large θ. It is also not clear from the experiments of Linden (1971, 1974) how salt fingers make a transition from 3-D salt fingers, where fluxes are reduced by shearing, to form 2-D sheets in high shear, where fluxes are not reduced by shearing. As salt fingers in the ocean generally occur in regions of high $\Delta V/U$, this is an important question that needs to be addressed.

Various mechanisms have been proposed by which the growth unsheared salt finger fluxes is limited at large amplitude. The initial growth of fingers is thought to be exponential until the point where shear instability (described by a Froude or Reynolds number criterion) sets in (Kunze, 1987). Holyer (1985) and Taylor & Veronis (1986) have identified vertical disturbances that grow on a wavelength comparable with the finger width, consistent with observations of Taylor (1993) that salt fingers with $1 < R_\rho < 5$ broke down into 'blobs' of aspect ratio 2. In 2-D and 3-D numerical experiments (Shen, 1995; Stern & Radko, 1998; Radko & Stern, 1999), low aspect ratio blobs were again found, and scaling was developed for the resulting buoyancy fluxes.

In the experiments reported here, active salt fingers and a sinusoidally varying shear were established simultaneously. Rather than dealing with a continuous spectrum of internal waves, we study the effects of shear produced only by a zero-frequency baroclinic mode. The shear

in this simple case is only a function of depth. A similar but finite frequency shearing mode is discussed by Wong *et al.* (2001) for the case of a filling box where a plume outflow feeds energy into vertically propagating internal wave modes having vertical wavelength similar to the thickness of the plume outflow. The salt finger buoyancy flux is reduced by strong shear, where maximum horizontal velocities are greater than vertical finger velocities. This leads to regions of flux divergence which change the local $\partial\rho/\partial z$ and R_ρ. The buoyancy flux becomes constant with depth when the variations in $\partial\rho/\partial z$ and $R_\rho(z)$ balance those caused by the variations in the shear so that density fine structure emerges with the same vertical wavelength as the shear. In the ocean such a periodic shear could be a mechanism for the initial formation of staircase structure, which would therefore reflect the vertical scales of internal waves, intrusions, or turbulent patches driving the shear.

4.2 Growth of density perturbations in a sinusoidal shearing flow

The action of a local horizontal velocity shear is to reduce the flux of T and S by changing the angle θ that the fingers make with the vertical (and hence reducing the effective gravity), so that the flux is locally reduced by a factor $\cos\theta$ (4.4). We assume that the horizontal velocity varies sinusoidally in the vertical so that $V = V_o \sin(kz)$, where k is the vertical wave number. The salt fingers will be tilted according to the local shear. For $R_\rho < 2$, heat/salt salt fingers are characterized by rising and falling blobs, so it seems appropriate to use a form similar to (4.2) to determine the angle. We use (4.4) to approximate the reduction in vertical buoyancy flux and define a flux reduction factor Ω as

$$\Omega \equiv \cos(\theta) = (\Theta^2 \cos^2(kz) + 1)^{-1/2}, \tag{4.6}$$

where $\Theta = V_o/U$.

For mathematical simplicity we will assume that we can describe the salt finger fluxes in the form of an eddy diffusivity as discussed in §1.2.4 . This assumption has been used by other authors, such as Walsh & Ruddick (1995b, 1998) and Zhang *et al.* (1998), when studying vertical length scales much larger than the finger scale. For low R_ρ, salt fingers have aspect ratio near 2 (Taylor, 1993), so in the present experiment the shear is always at much larger

scales than the finger length. In the following we use an eddy diffusivity that takes into account the effect of shear reduction (4.6), of the from $\Omega K_S(R_\rho)$, where $K_S(R_\rho)$ is the eddy diffusivity due to salt fingers that would occur without any shearing. The exact functional form of (4.6) or $K_S(R_\rho)$ is not critical in the following discussion; the important point is that where the shear is locally high, the eddy diffusivity $\Omega K_S(R_\rho)$ is reduced. The vertical fluxes of T and S are then

$$F_S = -\Omega\, K_S(R_\rho)\, \frac{\partial S}{\partial z}, \tag{4.7}$$

and

$$\alpha F_T = \gamma\, \beta F_S, \tag{4.8}$$

where γ is the ratio of T and S fluxes. Salt fingers transport S most efficiently, so that $\gamma < 1$, and there is a net transport of density downward. Laboratory measurements of the heat/salt system indicate $\gamma \approx 0.6$, and for sugar/salt $\gamma \approx 0.9$ (Turner, 1967; Schmitt, 1979b; Griffiths & Ruddick, 1980; McDougall & Taylor, 1984).

Using equations (1.22) and (1.23) the rates of change of S and T are

$$\frac{\partial S}{\partial t} = -K_S(R_\rho)\, (\Omega\, \frac{\partial^2 S}{\partial z^2} + \frac{\partial \Omega}{\partial z}\, \frac{\partial S}{\partial z}) - \Omega\, \frac{\partial K_S(R_\rho)}{\partial z}\, \frac{\partial S}{\partial z}, \tag{4.9}$$

and

$$\alpha \frac{\partial T}{\partial t} = \gamma\, \beta \frac{\partial S}{\partial t}. \tag{4.10}$$

With an initially constant salinity gradient $\partial S_{\text{initial}}/\partial z$ but spatially varying Ω, $\partial S/\partial t$ will be a function of depth, leading to flux divergences. The gradient $\partial S/\partial z$ must evolve in phase with $\partial \Omega/\partial z$. The initial growth rate of horizontally averaged salinity S is given by

$$\frac{\partial S}{\partial t} = -K_S(R_\rho)\, \frac{\partial \Omega}{\partial z}\, \frac{\partial S_{\text{initial}}}{\partial z}. \tag{4.11}$$

4.2.1 A steady state

A steady state ($\partial S/\partial t = 0$) can arise when there are no vertical gradients of buoyancy flux, ($\partial F_S/\partial z = 0$). In this case a simple solution to (4.9), assuming the changes of $K_S(R_\rho)$ with

depth are small in comparison to the other terms, is

$$\Omega \frac{\partial^2 S}{\partial z^2} = -\frac{\partial \Omega}{\partial z} \frac{\partial S}{\partial z}, \tag{4.12}$$

and hence

$$\frac{\partial S_{\text{steady}}}{\partial z} = \frac{c}{\Omega}. \tag{4.13}$$

where c is a constant of integration. This solution has maximum destabilizing $\partial S/\partial z$ at regions of minimum Ω, which are also regions of maximum shear. Stable αT anomalies grow in the same sense as βS anomalies by (4.10) but have smaller magnitude because $\gamma < 1$. This implies that the stable density gradient is dominated by $\beta \partial S/\partial z$ and has minimum $\partial \rho/\partial z$ at regions of maximum shear. Thus there may be a breakdown due to shear instability.

We can determine the constant c by assuming conservation of S over a vertical wavelength of the shearing, thus

$$\int_0^{k^{-1}} \frac{\partial S_{\text{steady}}}{\partial z} dz = \int_0^{k^{-1}} \frac{\partial S_{\text{initial}}}{\partial z} dz, \tag{4.14}$$

and the constant c is given by

$$c = \frac{1}{k} \frac{\partial S_{\text{initial}}}{\partial z} \left(\int_0^{k^{-1}} \frac{1}{\Omega} dz \right)^{-1}. \tag{4.15}$$

Evaluating c for the present form of Ω involves an elliptic integral and was done numerically. Using (4.13) and (4.11), we derive a timescale for the approach to the steady state. Integrating (4.13) gives $S(z)$, and we define a salinity anomaly as $\Delta S = \int (S_{z\ \text{initial}} - S_{z\ \text{steady}})\, dz$. If $\partial S/\partial t$ (4.11) is approximated as $\Delta S/\Delta t$, then the timescale is

$$\Delta t = \left(\frac{\partial \Omega}{\partial z} \right)^{-1} \frac{1}{K_S} \int \left(1 - \frac{c}{\Omega} \right) dz. \tag{4.16}$$

This timescale is a function of z. We are most interested in the time it takes to reach maximum ΔS, which occurs when $\partial \Omega/\partial z$ is a maximum. We define a dimensionless timescale Δt^* to reach maximum ΔS as

$$\Delta t^* = \Delta t\ k^2\ K_S / f(\Theta), \tag{4.17}$$

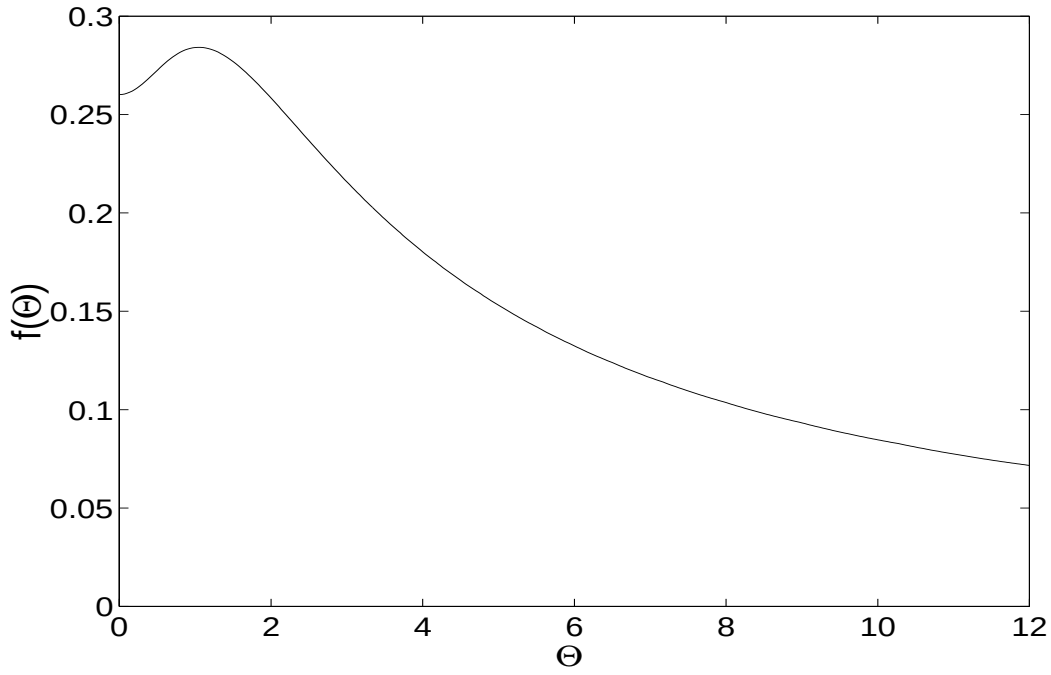

Figure 4.1: A numerical evaluation of the function $f(\Theta)$, defined by (4.18) plotted against Θ, the ratio of maximum horizontal velocity to vertical finger velocity. There is a maximum in $f(\Theta)$ of 0.28 at $\Theta \approx 1$.

where the dimensionless function $f(\Theta)$ is defined as

$$f(\Theta) = k^2 \left(\frac{\partial \Omega}{\partial z} \right)^{-1} \int_0^{k^{-1}} \left(1 - \frac{c}{\Omega} \right) dz, \tag{4.18}$$

and evaluated the depth z that corresponds to maximum $\partial\Omega/\partial z$. This function is plotted in figure 4.1 against Θ. There is a peak of 0.28 at $\Theta \approx 1$, while at large values of Θ, $f(\Theta)$ decreases like Θ^{-1}. If we use a parameterization of Ω based on (4.5) rather than (4.4), $f(\Theta)$ has a similar dependence upon Θ with a peak at $\Theta \approx 1$ of $f(\Theta) = 0.6$, implying that the time to equilibration Δt is twice as long. The form of the flux reduction implied by (4.4) was only experimentally verified by Linden (1971) up to $\Theta = 3$, so we caution the use of (4.18) at high Θ. The dimensional timescale Δt is inversely dependent upon the undisturbed vertical eddy diffusivity of salt K_s and wavenumber k of the shearing; highly active fingers in a varying shear of short wavelength will result in rapid approach to the steady density structure.

4.2.2 Numerical solutions

The model equations (4.9) and (4.10) were discretized using a semi-implicit Crank Nicholson scheme. For runs where the undisturbed vertical eddy diffusivity $K_S(R_\rho)$ is a function of local R_ρ we explicitly calculated this from current values of T and S for use in the next time step. Ω is calculated from (4.6) and the prescribed values of Θ and k. We ran the model with values typical of salt-sugar fingers: $\gamma = 0.9$, $K_S = 10^{-5}$ m^2 s^{-1} and $R_\rho = 2$, with a shear wavelength of $2\pi/k = 0.20$ m in a total tank depth of 1 m. We used no-flux boundary conditions to model laboratory conditions. Agreement between equilibrium predictions of §4.2.1 and calculated values of F_S, ΔS, and $\partial S/\partial z$ was very good. We have assumed that all the depth variation in the eddy diffusivity ΩK_S is due to the term Ω rather than changes in K_S with R_ρ, so we only discuss numerical solutions in which we set $\partial K_S/\partial z$ to zero. In runs where K_S was a function of R_ρ we found qualitatively similar behaviour in the evolution of F_S, ΔS, and $\partial S/\partial z$. When we parameterize the diffusivity in the realistic form of $K_S \propto R_\rho^{-1}$, the vertical fluctuations of K_S are small and the time Δt^* for adjustment to equilibrium is longer.

In figure 4.2 we plot the vertical flux of salt F_S defined by (4.7) for Θ= 0.5 and 2, which correspond to cases of weak and strong shearing through the term Ω (equation 4.6). The initial S_z was chosen to be uniform. However the vertical fluctuation in Ω led to divergence in F_S. In both cases the salinity field evolved with F_S becoming uniform in the central region and approaching the equilibrium state described by either $F_S = -\Omega\, K_S\, \partial S_{\text{steady}}/\partial z$ or $\partial S_{\text{steady}}/\partial z = c/\Omega$, which is plotted in figure 4.2 (b). Numerical evaluation of the constant c in (4.15) shows that it is a slowly decreasing function of Θ; thus we expect the steady F_S to be slightly less than the initial F_S, as is seen in figure 4.2 (a). The top and bottom boundary conditions lead to the more slowly evolving smooth gradient over the full depth. In figure 4.2 (c) we plot the flux reduction factor Ω due to shear for the same values of Θ. For the smaller values of Θ, there were changes of only 10% in the magnitude of the S flux, whereas for $\Theta = 2$ the fingers were periodically tilted up to 60° from the vertical and S fluxes are reduced by up to 50%, leading to large vertical flux divergences.

In figure 4.3 we plot further results from numerical simulations for $\Theta = 0.5$ and 2. In figure 4.3 (a) we plot ΔS, defined as $\Delta S = S_{\text{initial}} - S(t)$. This increases from an initial value of zero through an initial linear growth and equilibrates to a vertically periodic structure of

the same wavelength as Ω. Theoretical predictions for the steady values of ΔS are found by integrating (4.13), which are plotted as circles in figure 4.3 (a) and show good agreement with numerical results. The no-flux boundary conditions lead to growth of boundary layers at the top and bottom. The magnitude of ΔS is determined in part by the initial growth rate, which depends upon $\partial\Omega/\partial z$, plotted in figure 4.3 (c). At larger values of Θ, for which there is greater vertical variation in shearing, the amplitude of ΔS is larger. In the numerical simulation we also calculate the evolution of T using (4.10) and determine $\rho = \rho_o[1-\alpha(T-T_o)+\beta(S-S_o)]$. In figure 4.3 (b) we plot the normalized density gradient $\rho_z/|\rho_{z\ \mathrm{initial}}|$. A comparison of figures 4.3 (b) and 4.2 (c) shows that minimum ρ_z occurs where Ω is smallest, which is where the shear is highest. Thus shear instability may occur, and if it does, it will be at levels of minimum Ω.

The growth of ΔS is plotted against the dimensionless time Δt^* (defined by 4.17) in figure 4.4, for Θ = 0.5 and $\Theta = 2$ at the depth $z = 0.45$ m (at which point $\partial S/\partial t$ is at a local maximum). In both cases, there is a brief period of initial growth in good agreement with the predictions of (4.11) which are plotted in figure 4.4 as straight lines. Later, growth slows, and the profiles asymptotically reach a steady state at around $\Delta t^* = 1$.

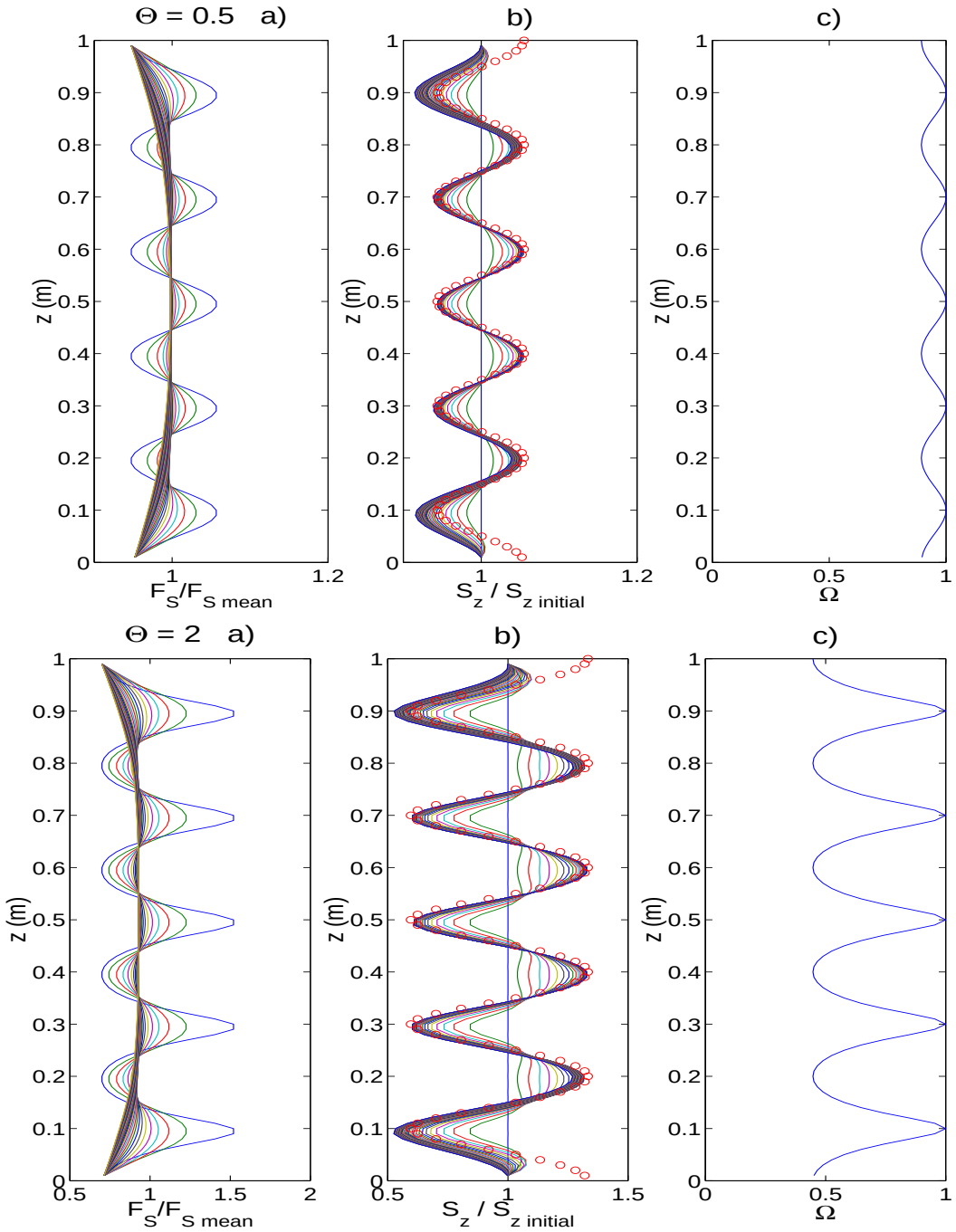

Figure 4.2: Numerical solutions of (4.9) and (4.10) starting with a uniform gradient S_z, with $\Theta = 0.5$ (top) and $\Theta = 2$ (bottom). (a) The salt flux F_S normalized by the mean initial value of F_S, (b) the salinity gradient S_z normalized by $S_{z\ \text{initial}}$ and the prediction of (4.13), which is plotted as circles, and (c) the flux reduction factor Ω. The flux divergences result in changes in S_z, and the flux F_S becomes uniform. The final steady values of $S_z/S_{z\ \text{initial}}$ agree well with the prediction of (4.13).

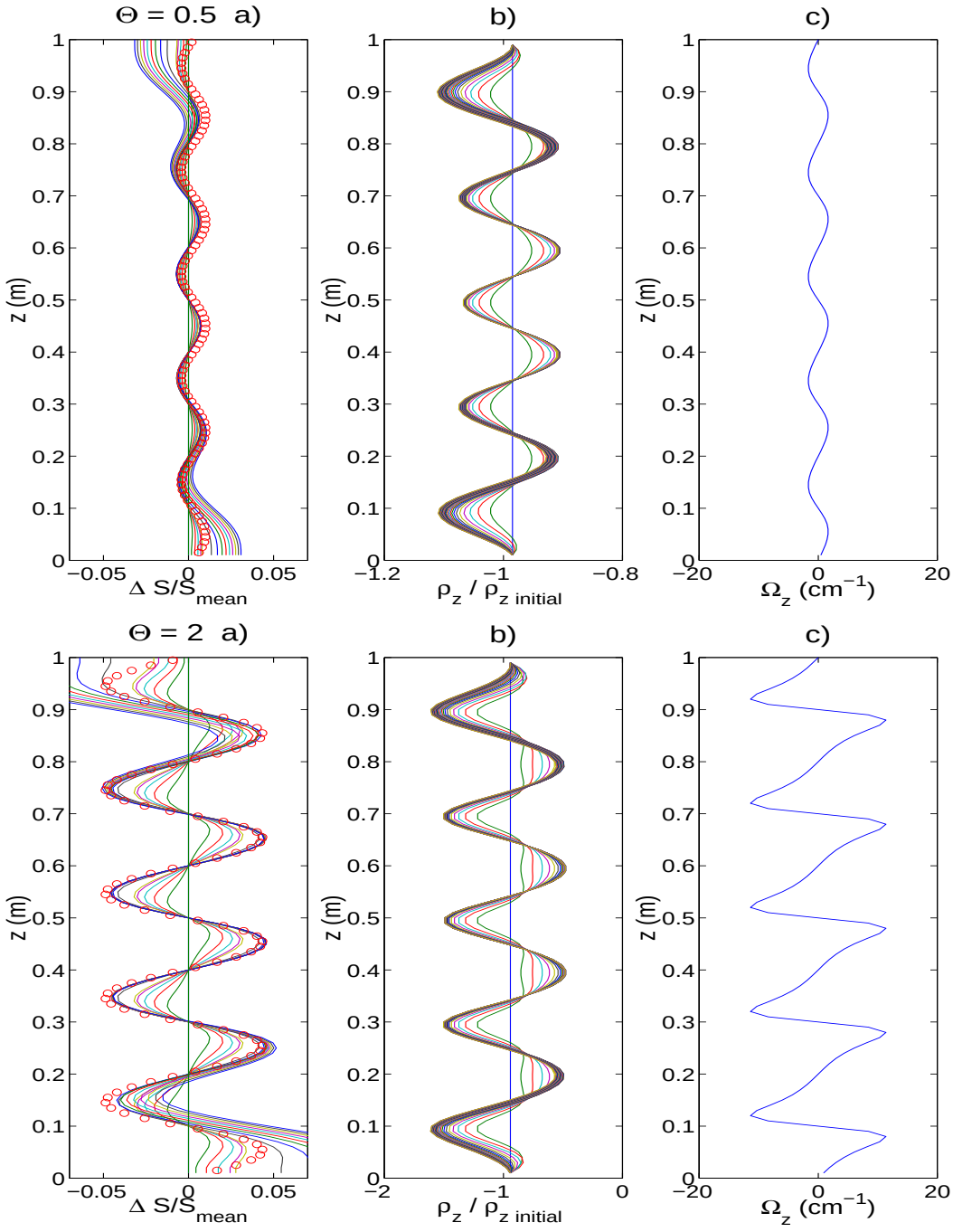

Figure 4.3: Further results of numerical solutions, with $\Theta = 0.5$ (top) and $\Theta = 2$ (bottom). Plotted are (a) the salinity anomaly $\Delta S = S_{\text{initial}} - S(t)$ along with predicted values (circles) that are found by integrating (4.13), (b) the normalized density gradient ρ_z, and (c) Ω_z. Note that ΔS evolves to a steady state with periodic changes of the same wavelength as the shear and Ω_z has greater magnitude for $\Theta = 2$ than for $\Theta = 0.5$. The use of a no-flux boundary condition causes ΔS to grow at the top and bottom boundaries.

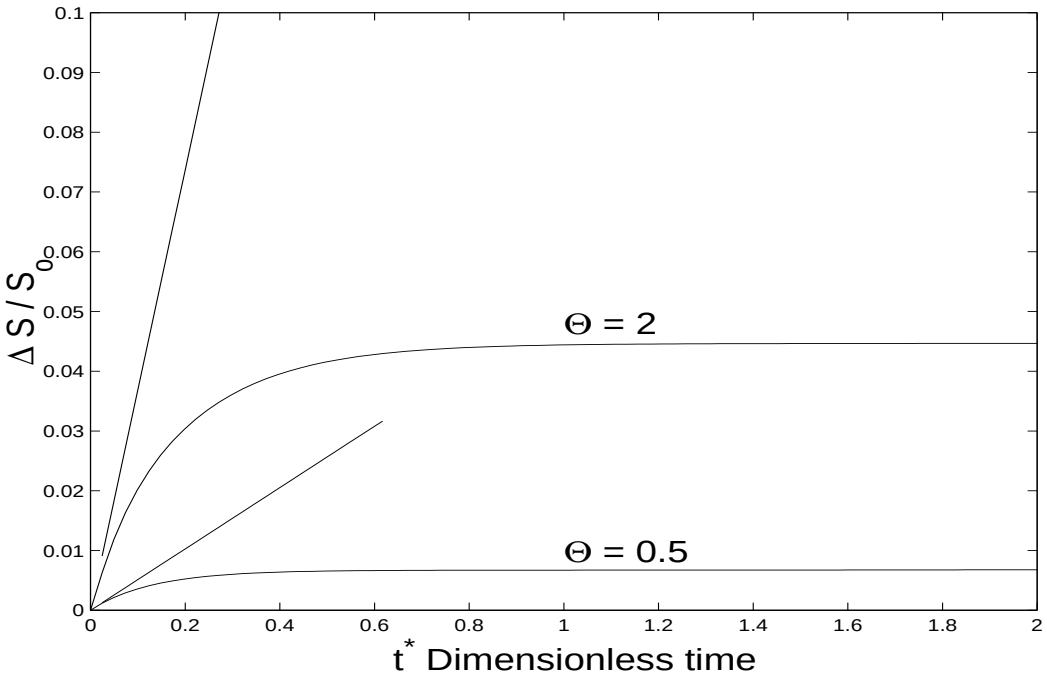

Figure 4.4: Further results of numerical solutions. The evolution of ΔS toward its steady value is plotted here at $z = 0.45$ m for $\Theta = 0.5$ and $\Theta = 2$. When $\Theta = 2$, the steady value of ΔS is roughly 5 times that when $\Theta = 0.5$. The initial growth of the anomaly is well described by the linear prediction of (4.11) (straight line). In figure 4.3 (a) the depth of $z = 0.45$ m is the local site of maximum ΔS.

4.3 Experimental observations of salt fingers in shear

4.3.1 Experiments

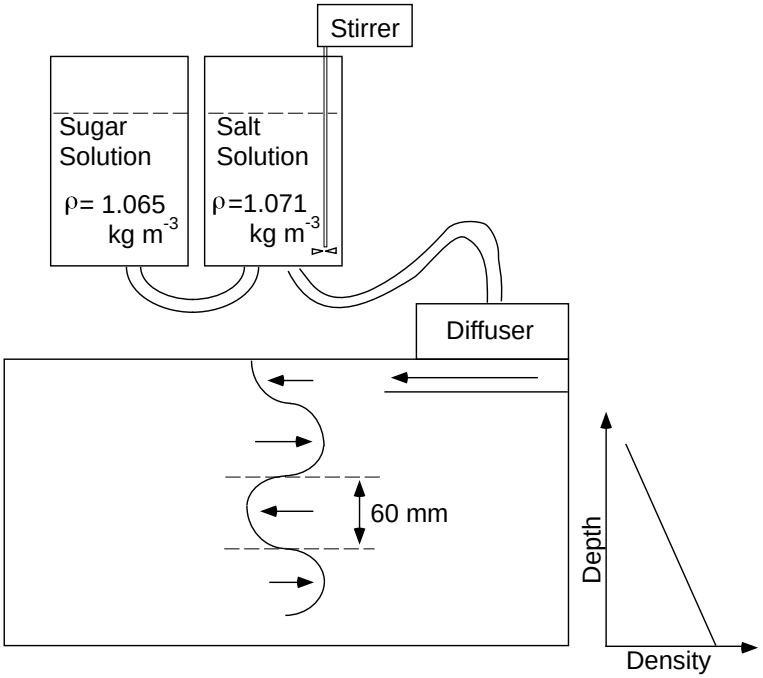

Figure 4.5: A linear density gradient produced using the standard double bucket method. By using a small float localized at one of the tank we were able to force a low-frequency baroclinic mode of wavelength of 120 mm as the tank was being filled.

To conduct experiments on the effect of a steady sinusoidal shear, we used a double bucket system to produce a salt finger-favourable density gradient by continuously adding less dense (but more S rich) solution at the top of the gradient through a permeable diffuser floating on the the surface of the tank, as shown in figure 4.5. The diffuser was confined to one end of the tank so that the outflow of less dense solution produced a surface flow toward the other end of the tank, while creating the density gradient. This arrangement produced a low-frequency baroclinic mode with a vertical wavelength of ~ 120 mm and maximum horizontal velocities of around $V = 2.5$ mm s^{-1}. The maximum shear was ~ 0.05 s^{-1}. A discussion of similar baroclinic modes forced by the outflow of a turbulent plume is given by Wong *et al.* (2001). For the initial density gradients and horizontal velocities used in these experiments the calculated Richardson numbers are high so that the flow is stable to shear instabilities. Vertical velocities of the fingers were measured from the shadowgraph as $U = 2.5 \pm 0.5$ mm s^{-1}, which is the

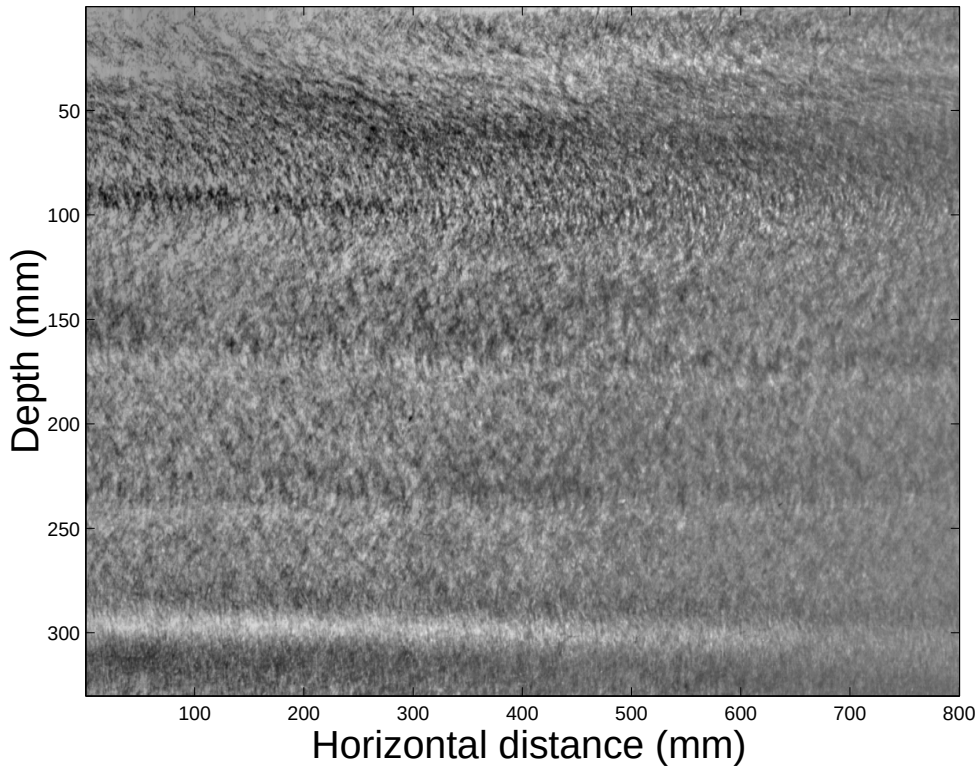

Figure 4.6: A shadowgraph of the observed shearing and banded density structure, $R_\rho = 1.13$ and $N = 1\text{s}^{-1}$

same as the maximum horizontal velocity. This resulted in fingers being tilted to 45°.

In the laboratory it is easier to use salt and sugar in place of the oceanic properties of heat and salt, thus avoiding the difficulties in insulating the experiment and in making observations and measurements very rapidly before a heat/salt system runs down. The difference in molecular diffusivities between sugar and salt is much less than between heat and salt, so the resulting salt finger convection is less vigorous. In these experiments it is usual to refer to the faster diffusing component as T and the slower as S. However, one experiment was conducted with heat/salt, and similar layered structure was observed in the shadowgraph. A series of eight sugar/salt experiments were conducted for R_ρ = 1.02-2.2 and N = 1-5 s^{-1}. In all cases the tank was filled in the same manner.

We observed the experiments using a shadowgraph, an example of which is shown in figure 4.6. The salt fingers are sheared, and there are bands of different intensity in the vertical indicating that there are variations in horizontally averaged density gradient. This ‘layering’

of the density gradient was observed in experiments with low R_ρ, where there was a large buoyancy flux and hence faster growth rate of ΔS as predicted by (4.11). The emergence of a steady pattern is consistent with (4.13). For runs with $R_\rho > 1.5$, layering was not observed. The absence of visible structure under these conditions may have been a result of the limited duration of the forcing or a change of phase of the forcing (on a period of order 300 s) from the filling of the tank. We use (4.17) to get an idea of the timescale at which the disturbances are expected to grow. In chapter 5 (§5.3.3) an experimental determination of buoyancy flux for the salt/sugar system for $R_\rho = 1.13$ and $N = 1$ s^{-1} finds $K_S \approx 10^{-5}$m^2 s^{-1}. Thus with a shear that has 60 mm between maxima and $\Theta = 1$ we expect the time to reach the equilibrium state to be $\Delta t = 90$ s. The numerical simulations in figure 4.4 clearly show the emergence of structure before the dimensionless time $\Delta t^* = 1$, so the dimensional result is consistent with observations of banded structure in the shadowgraph of figure 4.6 after only 30 s of forcing for low values of R_ρ. The experiments with higher R_ρ had a lower vertical eddy diffusivity K_S and hence took much longer to produce significant density structure.

4.3.2 Salinity profiles

By taking measurements of the salinity gradient we can test some of the ideas developed in § 4.2.1. The conductivity and temperature were measured as functions of depth using a conductivity probe (Head Precision Engineering model 5021) and thermistor (Fenwal GB38P12). The salinity profiles were calculated from these using the polynomials of Ruddick & Shirtcliffe (1979), and the mean linear salinity gradient was subtracted from the measured profiles (figure 4.7 a) to obtain the fluctuations (figure 4.7 b). Because the tank was being filled from the surface diffuser, the forcing is constant relative to the surface, and the pattern of the salinity fluctuation remained constant relative to the surface. The wavelength of the anomaly was the same as that of the shear (observed with the shadowgraph) and has a similar sinusoidal pattern to that described in §4.2.1. The salinity anomaly becomes much smaller near the base of the tank due to the decay of velocity in the low-frequency shear mode with distance from the forcing region (Wong *et al.*, 2001).

Unpublished experimental results of Turner (1974), which were carried out to explore further some qualitative observations reported by Turner & Chen (1974), show a similar behaviour to that described here. His experiment consisted of three layers: a top layer containing sugar,

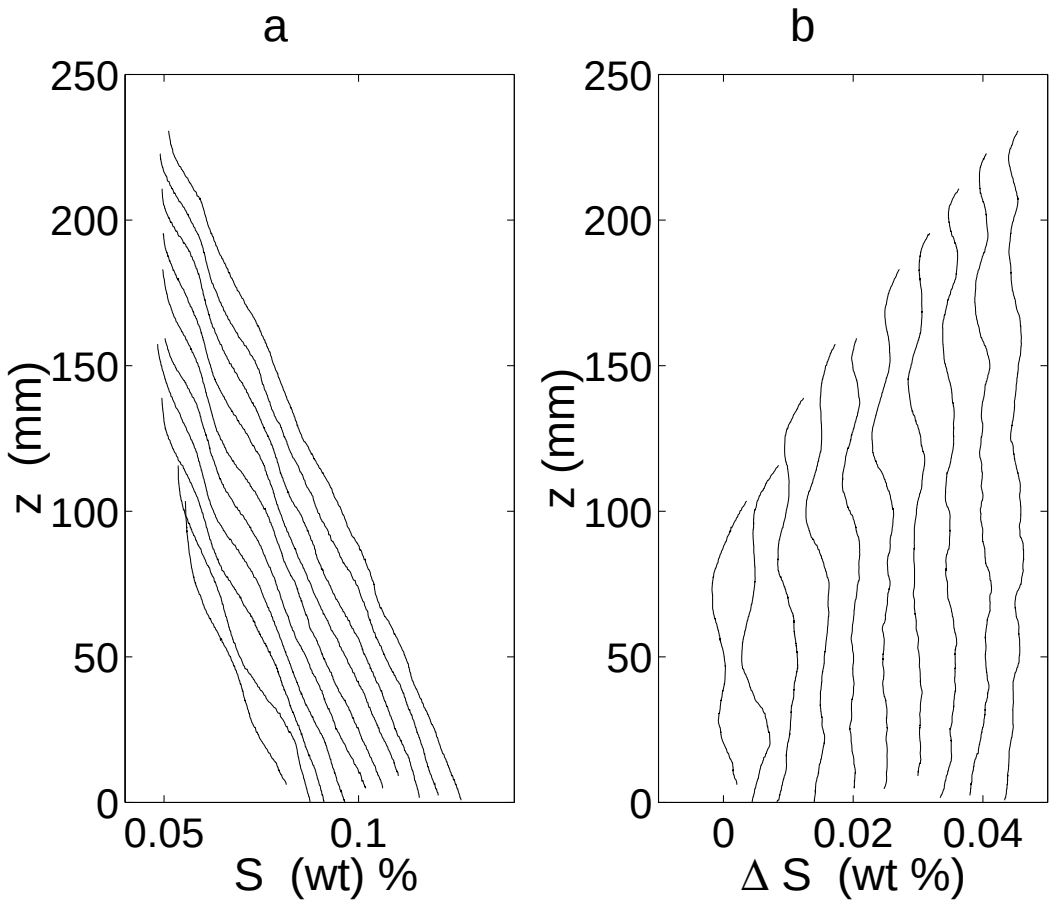

Figure 4.7: Measured salinity profiles through the salt-sugar gradient shown in figure 4.6 while the density gradient is being filled using the double bucket method. In figure 4.7 (a) successive profiles of salinity gradient taken 1 min apart are shown, each offset by 0.005 wt %. The fluctuations in the salinity gradient resulting from the shear are plotted in figure 4.7 (b) after subtracting the background linear gradient of salinity (profiles offset by 0.005 wt %).

a middle layer containing a gradient region (from sugar at the top to salt at the bottom), and a lower layer of salt. Between these layers were solid horizontal boundaries, each with a gap at opposite ends as shown in figure 4.8. The system was unstable to salt finger convection. As a result of the horizontal separation of the gaps in the horizontal boundaries the convection set up horizontal density differences which rapidly generated a low-frequency baroclinic mode with four layers, very similar to the shear structure used in the present experiments. The rapid emergence of a banded structure which broke down to form a staircase structure with two interfaces at the top and bottom where the shear was greatest, is shown in figure 4.9. As the density gradient changed due to flux divergences, there may have been bands of low Richardson number

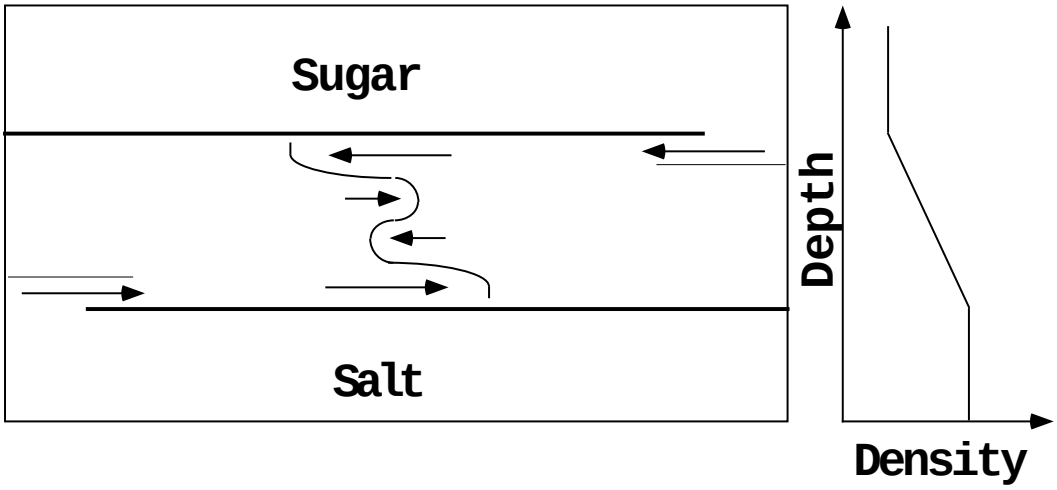

Figure 4.8: A second experimental setup which produces zero frequency baroclinic modes with stronger diagonal forcing. The three layers are filled separately, and then two barriers are removed at the ends. The salt finger buoyancy flux forces the circulation shown. This "cross gradient" experiment was carried out by J. S. Turner in 1974, but a description has not been previously published.

and consequent the shear instability. These experiments had much larger horizontal velocities than present experiments. The formation of regions of low stability in regions of high shear is predicted by (4.13) for the case of a constant diffusivity and was also found for non-constant diffusivity in numerical experiments. This "density staircase" structure looks very similar to structure reported by Linden (1978) except that the vertical wavelength is set by the imposed shear rather than an intrinsic salt finger length scale.

Figure 4.9: Three successive shadowgraphs of the cross gradient experiments by Turner (1974). In the first photograph, only the bottom salt reservoir and the middle salt finger region are in place. When the top sugar reservoir was added, the shearing set up by the horizontal differences in vertical buoyancy flux led to bands in the shadowgraph. The third photograph shows the subsequent breakdown into a series of convecting layers.

4.4 Discussion and conclusion

The results of our experiments indicate that density structure can be formed from an initially linear density gradient by a spatially varying shear in the presence of salt fingering. The spatially varying shear leads to a divergence of the salt finger buoyancy flux on the same wavelength as the shear, and this in turn leads to an initial rapid growth in density perturbations from a linear gradient. Further growth of the fine structure ceases once the fluctuations in $\partial S/\partial z$ and R_ρ become large enough for vertical flux divergences to vanish.

This response to low-frequency shearing represents a previously unreported mechanism by which density fine structure can arise from salt finger convection. The initial vertical scale does not depend upon an intrinsic finger length scale nor the scale of collective instability but instead upon the externally imposed shear wavelength. If the forcing is very strong the formation of the density structure by the salt fingers may lead to low Richardson numbers, shear instability, and consequent breakdown into a series of convecting layers, as shown in figure 4.9. This new mechanism adds to the variety of other mechanisms by which structure can be produced in a continuous density gradient. Experimental observations by Stern & Turner (1969) and Linden (1976) showed that a finger-favourable gradient region between two unstratified reservoirs can breakdown to a series of convecting layers. We interpret these convecting layers as being due to the large buoyancy fluxes occurring at the edge of the salt finger region which results in the formation of layering by a similar mechanism to the experiments of Turner (1968) where a stable salinity gradient is heated from below. Layered structures also form when two bodies of water with different thermohaline properties meet to give horizontal gradients of T and S (Turner & Chen, 1974; Ruddick & Turner, 1979).

In none of our experiments did we observe the formation of two-dimensional salt finger sheets aligned with the shear as seen by Linden (1974). This is probably because horizontal velocities were never much larger than finger velocities. Kunze (1990, 1994) inferred that the formation of such sheets was important in the CSALT experiment where the shear due to inertial waves was large. We hope this thesis will motivate further study of externally imposed velocity gradients in direct numerical simulations of salt fingering to quantify when flux reduction or formation of 2-D sheets occur under oceanographic shearing conditions, as we are not aware of any laboratory studies after the original work by Linden (1971, 1974).

Whether or not the mechanism suggested here is important in the initial development of oceanographic fine structure depends sensitively on the magnitude and wavelength of the vertical shear, the salt finger velocity, and eddy diffusivity as these control the timescale of the fine structure growth (4.17). St. Laurent & Schmitt (1999) found values of the eddy diffusivity of temperature due to salt fingers of the order of $K_T = 10^{-5}$ m^2 s^{-1} when $R_\rho = 2$ at the NATRE site. We use this observation to infer a characteristic vertical velocity of a salt finger. Steady salt fingers have a balance between vertical advection and horizontal diffusion of temperature (Stern, 1969) so that

$$w' \frac{\partial T}{\partial z} = \kappa_T k^2 T', \tag{4.19}$$

where w' and T' are velocity and temperature anomalies in the salt finger field, $\kappa_T = 1.4 \times 10^{-7}$ m^{2}s^{-1} is the molecular diffusivity of heat, $\partial T/\partial z$ is the background temperature gradient and k is the horizontal wave number of salt fingers. If we equate the salt finger flux $K_T\ \partial T/\partial z$ with $< w'T' >$, then we can determine a vertical salt finger velocity w' as

$$w' = k\sqrt{\kappa_T K_T}. \tag{4.20}$$

At the NATRE site k was of the order of 100 m^{-1} implying that vertical velocities were of the order of $w' = 10^{-4}$ m s^{-1}. Measurements of fine structure at the NATRE site by Polzin *et al.* (2001) found that turbulent patches have typical thickness D = 1-10 m. After a turbulent event, partially mixed patches collapse with a Richardson number of the order of 1, so that the maximum shear is $\Delta U/D = N$. With a typical buoyancy frequency at the NATRE site of the order of $N = 10^{-5}$ s^{-1} this implies horizontal velocities of the collapsing patches were of the order of $\Delta U = 10^{-4} - 10^{-5}$ m s^{-1}. The ratio Θ of maximum horizontal velocities to maximum vertical finger velocities is then of order Θ = 0.1–1, so that the dimensionless function $f(\Theta)$ is in the range 0.1–0.25. This implies that the timescale for the formation of significant density structure (4.17) is of the order of $\Delta t = 10^3 - 10^4$ s when collapsing turbulent patches are driving intrusions and the associated spatially varying shear described by Wong *et al.* (2001). Inertial waves are another candidate for a spatially varying shear, but as their vertical wavelengths are typically larger than 10 m and their shear is typically lower than in collapsing intrusions, the growth times (4.17) are consequently orders of magnitude larger, and density structure would not appear in less than the timescale $1/2f$ over which the shear changes phase.

Chapter 5

Localized stirring experiments in salt finger-favourable gradients

In this chapter experiments and theory on the interaction between isolated patches of turbulence and salt finger convection are presented. Previous experiments with salt fingers are discussed in §5.1. In §5.2.1 we review background theory on partially mixed turbulent patches. In §5.2.2 we model the effect that 'up gradient' buoyancy fluxes of salt fingers have upon a partially mixed patch. We show that salt fingers can lead to overturning instability of this region. A criterion is derived in §5.2.3 for the critical patch thickness for a transition to occur from laminar salt finger convection to overturning convection. Turbulent entrainment is shown to lead to an increase in patch thickness in §5.2.4. These theoretical predictions are compared with new experimental observations in §5.3. The application to an oceanographic setting is discussed in §5.4.

5.1 Previous salt finger experiments

In a series of exploratory experiments, Turner & Chen (1974) noted that under certain conditions, an isolated patch of turbulence could cause a salt finger favourable gradient to breakdown into a convecting layer. These experiments were conducted in a tank of length 90 cm, width 7 cm and depth 30 cm. Using the double bucket method, the tank was filled with linear 'crossed' gradients of sugar and salt to create a salt finger favourable gradient. A small flap was located at the left end of the tank that could be moved up and down, to create a patch of turbulence. A photograph from one of their experiments is shown in figure 5.1. Here the tank had been filled with an initially linear density gradient, with $R_\rho = 1.08$. At 20 minutes after the

initiation of filling, the flap was raised by 45° from its initial vertical position. This generated a patch of turbulence, which subsequently caused the linear density gradient to breakdown and form a well-mixed convecting layer at the base of the tank. At 54 minutes the flap was moved to 45° upwards, generating a patch of turbulence in the top of the tank but now no convecting layer formed. The photograph shown in figure 5.1 was taken at 85 minutes and the sharp interface above the lower convecting layer can be seen. As the T and S gradients decrease with time during experiments, R_ρ increased with time. Other experiments with different R_ρ showed similar behaviour - with R_ρ near one, virtually any disturbance would cause breakdown into a convecting layer, but at later times (when R_ρ was higher) no amount of mixing could lead to the breakdown to a convecting layer.

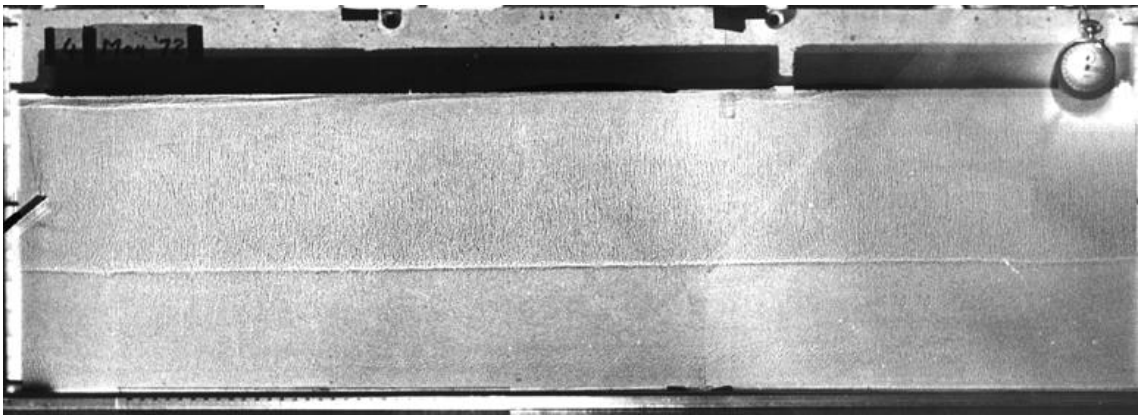

Figure 5.1: A photograph taken at 85 minutes after the start of the experiment. A convectively overturning layer can be seen at the base of the tank, with salt fingers occupying the rest of the tank. The convecting layer was generated by setting the flap down at 20 minutes, subsequent movement of the flap at 53 minutes failed to cause another convective layer. Photograph reproduced from Turner & Chen (1974).

Some further experiments from Turner & Chen (1974) are shown in figure 5.2. The tank was filled with a salt finger favourable gradient as before, but a wedge was now placed at the left end of the tank. This locally reduced the width of the tank. With the double bucket method of creating $T - S$ gradients, the reduced width meant that a region of low density gradient was produced in the otherwise linear gradient. At 39 minutes after the start of the experiment the salt finger gradient broke down and a convectively overturning layer formed of the same vertical dimension as the wedge, as shown in figure 5.2 (a). At 63 minutes the convecting layer was well established and had increased in thickness by 10%, as shown in figure 5.2 (b). This

is similar to the theoretical predictions of Stern & Turner (1969), where a convecting patch in a salt finger gradient increases in thickness with time due to convective entrainment. The two processes illustrated in figures 5.1 and 5.2 may be important in the ocean where isolated turbulent patches could interact with salt fingers to form convecting layers. This would result in large horizontal intrusions and may be important in the initial formation of density staircase structures that are often associated with salt fingers in the ocean.

a)

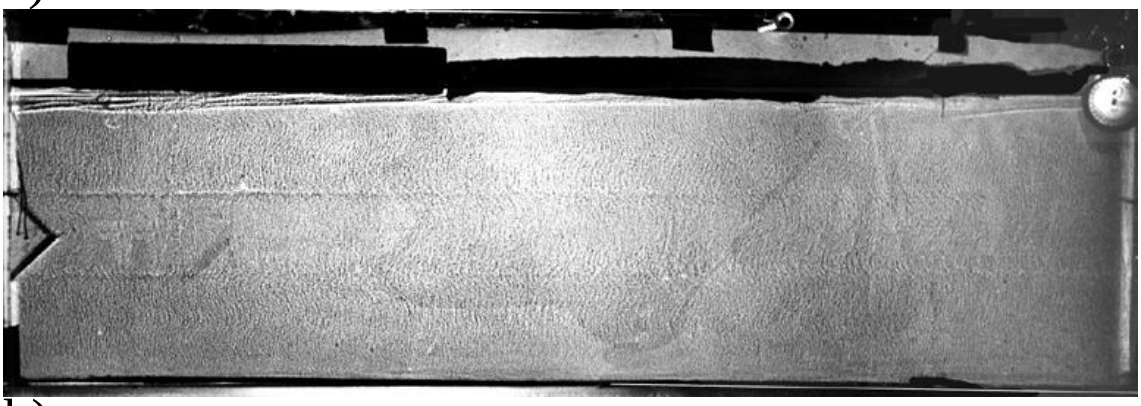

b)

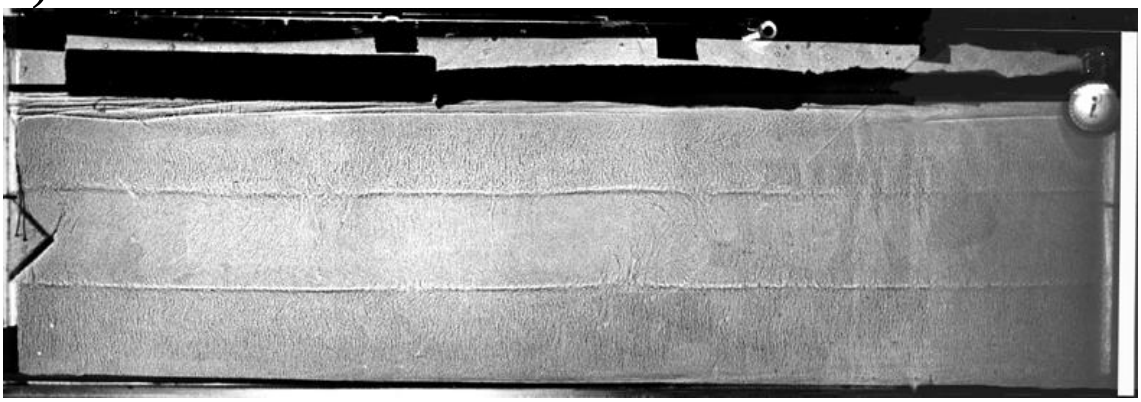

Figure 5.2: The disturbance was created by filling the tank past a wedge fixed on the left wall. a) 39 minutes into the experiment, showing initiation of the convecting layer, b) 63 minutes, with convection well established. Photographs reproduced from Turner & Chen (1974).

The qualitative experiments of Turner & Chen (1974) show that a salt finger gradient can breakdown to a convecting layer if there is sufficient mixing and R_ρ is near one. Theoretical models have been developed by Zhurbas, Kuzmina & Kulsha (1987), Walsh & Ruddick (1995b) and Merryfield (2000) which show that an 'up gradient' flux of density due to salt fingers, can form density anomalies in an initially linear density gradient. Subsequent flux di-

vergences can locally weaken the density gradient and may lead to overturning instability and convection. While 'up gradient' flux divergences offer a plausible mechanism for the breakdown of a linear gradient, the models of Zhurbas, Kuzmina & Kulsha (1987), Walsh & Ruddick (1995b) and Merryfield (2000) did not depend upon R_ρ or the magnitude of the initial density anomaly. In the next section we develop theory to quantify the previous observations of Turner & Chen (1974) in terms of the initial R_ρ, vertical scale of the turbulent patch and the degree of mixing within the patch. The theory is then tested against new experiments in §5.3.

5.2 Theory

5.2.1 Salt fingers and turbulent mixed patches

Turbulent patches can be created in stable density gradients by shear instability, internal wave breaking or mechanical mixing (Turner, 1973). It has been widely recognized that a patch of turbulence due to wave breaking or mechanical mixing of a density gradient will not result in complete mixing of the density gradient within the patch. An illustration of vertical gradients in such a partially mixed patch is shown in figure 5.3. The mixed patch has an interior region, of depth h_{in}, where the density gradient has been reduced by the action of the turbulent mixing. This interior region is bounded above and below by thin interfaces of high density gradient. The ratio of the outer patch thickness h_{out}, to inner patch thickness h_{in} was measured by De Silva & Fernando (1992) as being around 0.8, indicating most of the patch depth is occupied by low density gradient. The vertical scale of a turbulent patch, h_{out}, can be determined by a balance between buoyancy and energy dissipation (Ivey & Imberger 1990).

Partial mixing of a density gradient results from the low efficiency of converting mechanical energy into increased potential energy of the density gradient. Measurements by Linden (1979, 1980) indicate that turbulent mixing is strongly dependent upon a Richardson number and has a maximum mixing efficiency of 25%. A parameter related to the mixing efficiency is the 'mixedness' parameter of De Silva & Fernando (1992) and Hughes (1996).The mixedness of the patch shown in figure 5.3 (a), is defined as the ratio of the mixed interior density gradient, $d\rho_{in}/dz$ to the initial linear density gradient, $d\rho_{initial}/dz$, as

$$M = 1 - \frac{d\rho_{in}}{dz} \Big/ \frac{d\rho_{initial}}{dz}. \tag{5.1}$$

The mixedness can also be defined in terms of the density difference over the patch, defined as $\Delta\rho_{out} = h_{out}\, d\rho_{initial}/dz$,

$$M = 1 - \Delta\rho_{in}/\Delta\rho_{out}. \tag{5.2}$$

Complete mixing corresponds to $M = 1$ and no mixing corresponds to $M = 0$. Experiments by De Silva & Fernando (1992), in which a linear gradient was stirred by a mechanical device, have shown that both M and the patch thickness h decreased with increasing Richardson number of the stirring and increased with the duration of the stirring. Thus weak and brief stirring of a linear density gradient resulted in thin patches of low mixedness ($M \sim 0$) and strong continued stirring resulted in deep well-mixed patches with high mixedness ($M \sim 1$).

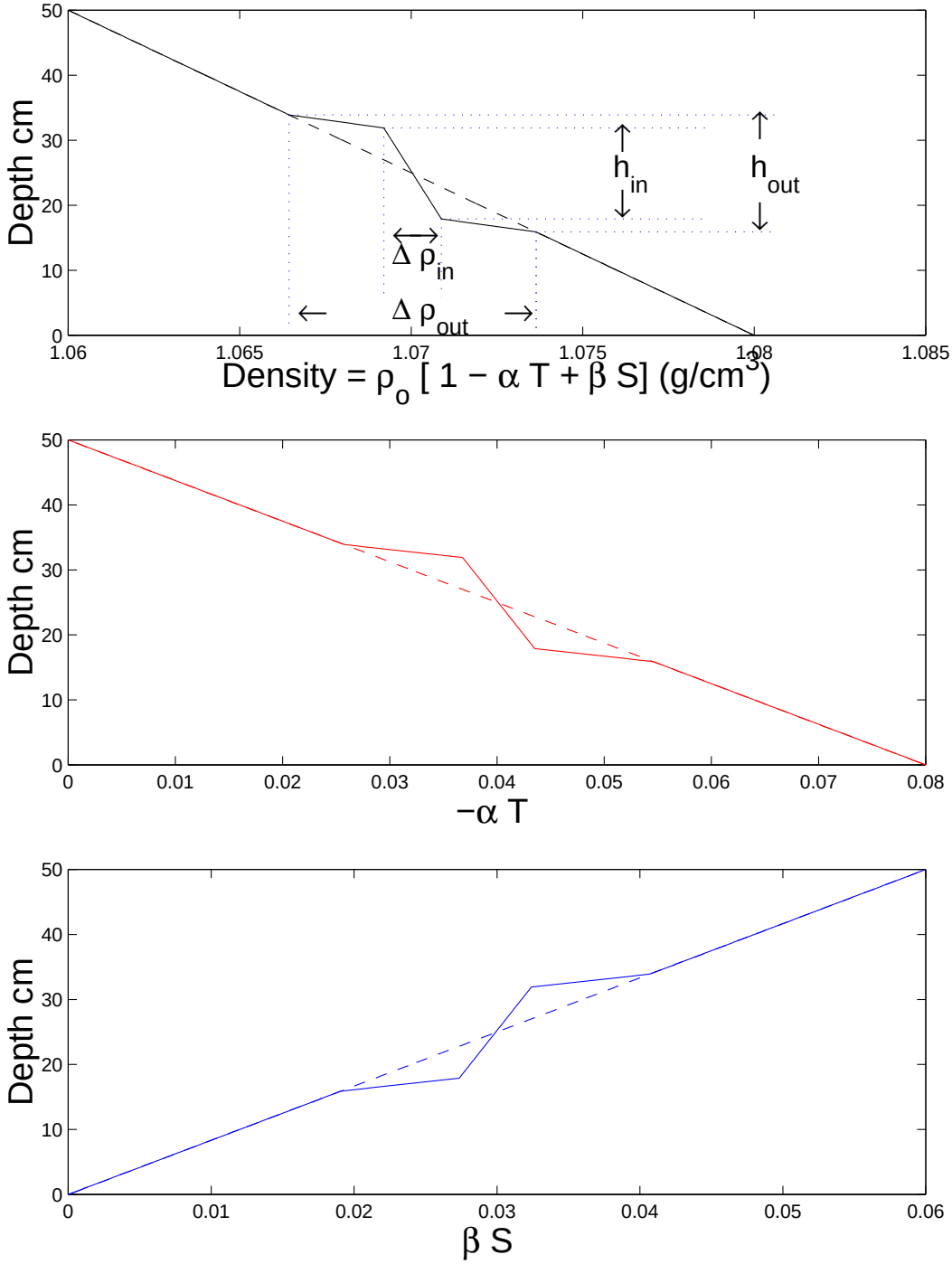

Figure 5.3: (a) A sketch of the density gradient of a partially mixed patch. In the interior region the density gradient is weaker, while in a thin inter-facial region at the edges the density gradient has increased. In (b) and (c) we sketch the S and T distributions after a turbulent event. In this figure we have plotted values typical of laboratory sugar-salt experiments where $R_\rho = 1.13$.

5.2.2 Overturning due to salt fingers

Salt fingers can change density fine structure due to vertical divergences in T and S fluxes. If the partially mixed region has a large horizontal extent then we can consider a simple one dimensional model of the evolution of the T and S fields and use the flux equations (1.22), (1.23), (1.24) and (1.25), as discussed in § 1.2.3.2. An 'up gradient' flux of density is consistent with a negative diffusivity of density, K_ρ. However mathematically this implies that density anomalies at the smallest scales would grow the fastest. The effective diffusivity of salt K_S is positive, and it is only due to the coupling of T and S fluxes in (1.25) that there is an 'up gradient' flux of density. The time evolution of S anomalies after a perturbation is simply one of enhanced 'diffusion' to a linear gradient. The coupling of fluxes in (1.25) means that the T anomalies will change only while the S anomalies are changing. This is different to the model of Merryfield (2000) who considered the evolution of perturbations in a density gradient by 'up gradient' salt finger fluxes using a negative diffusivity of density.

Initially we shall consider the simple case illustrated in figure 5.3 (b) and (c) where the T and S gradients were initially linear. Figure 5.3 is plotted in the sugar/salt sense, where increasing the concentration of T (salt), increases the density. After a mixing event of depth h_{in} the local gradients in the patch interior will have weakened by the factor $1-M$. The ratio of T and S gradients, R_ρ, remains constant because turbulent mixing changes only the density gradient and transports S and T equally. After the turbulence has stopped the change in S over the interior of the patch is

$$\Delta S_{in} = (1-M) h_{in} \frac{dS_{initial}}{dz}, \tag{5.3}$$

and the change in T over the interior of the patch is

$$\alpha \Delta T_{in} = R_\rho \, \beta \Delta S_{in}. \tag{5.4}$$

The action of salt fingers on the S component is governed by (1.22) to (1.25). Because the flux ratio $\gamma < 1$ the S gradient changes more rapidly than the T gradient. Hence R_ρ will change within the interior of the patch, implying that K_S would also change. For mathematical simplicity we will initially assume that K_S is a constant. With this assumption S will 'diffuse' back

to the original linear gradient and the change in S over the patch depth is

$$\Delta S_{final} = h_{in} \frac{dS_{initial}}{dz}. \tag{5.5}$$

The time scale for evolution of the S component back to the original linear gradient after the mixing event is of the order of

$$t = h_{in}^2 / K_S. \tag{5.6}$$

The changes in T are related to changes in S by the flux ratio γ. The total change in T from the time after the turbulent event to the time that flux divergences in S disappear is

$$\alpha(\Delta T_{final} - \Delta T_{in}) = \gamma M \, \beta \Delta S_{in}. \tag{5.7}$$

Because $\gamma < 1 < R_{\rho\ initial}$ the final T_z will be less than before the mixing event and consequently the final R_ρ will be smaller. There is now the possibility that this final T gradient will no longer compensate for the unstable S gradient, making the density gradient unstable. This occurs if $\alpha \Delta T_{final} / \beta \Delta S_{final} \leq 1$. Using (5.3), (5.5) and (5.7), this implies that an unstable density gradient occurs when

$$R_{\rho\ initial} \geq \frac{1}{1-M} - \gamma M. \tag{5.8}$$

Thus for small $R_{\rho\ initial}$ a small mixedness M can lead to flux divergences that result in overturning instability of the density gradient and when $R_{\rho\ initial} = 1$, any value of M will lead to an unstable density gradient. For large initial R_ρ an unstable density gradient occurs only when M is almost one. This is similar to the observations of Turner & Chen (1974). Increasing γ to a greater value means that a larger mixedness M is required for overturning instability to occur, implying that heat/salt fingers will be more unstable than sugar/salt fingers.

To test these ideas we model the evolution of T and S gradients due to salt fingers by numerically solving equations (1.22), (1.23), (1.24) and (1.25) using a semi-implicit Crank Nicholson scheme, as used in § 4.2.2. The initial T and S gradients are shown in figure 5.4 and are similar to those sketched in figure 5.3 except now we use more realistic gradients to model a partially mixed patch. The initial mixing efficiency in figure 5.4 is $M = 0.9$ and initial $R_\rho = 1.3$, representative of sugar/salt laboratory experiments that will be discussed in §5.3.

The S gradient evolves by a 'diffusion' equation until $\partial^2 S/\partial z^2 = 0$, where flux divergences are zero. The T flux is coupled to the salt gradient by the flux ratio $\gamma = 0.9$. As the final T gradient is less than the initial T gradient, the stability of the density profile has decreased. The result is that the density profile, shown figure 5.4 (c), becomes less stable with time. For the parameters we have chosen, the final density gradient is less than zero (i.e. unstable) in the center of the interior region. This corresponds to overturning instability and is in agreement with predictions of (5.8). Further runs (not shown) were conducted where M, γ and R_ρ were varied and also found good agreement with (5.8).

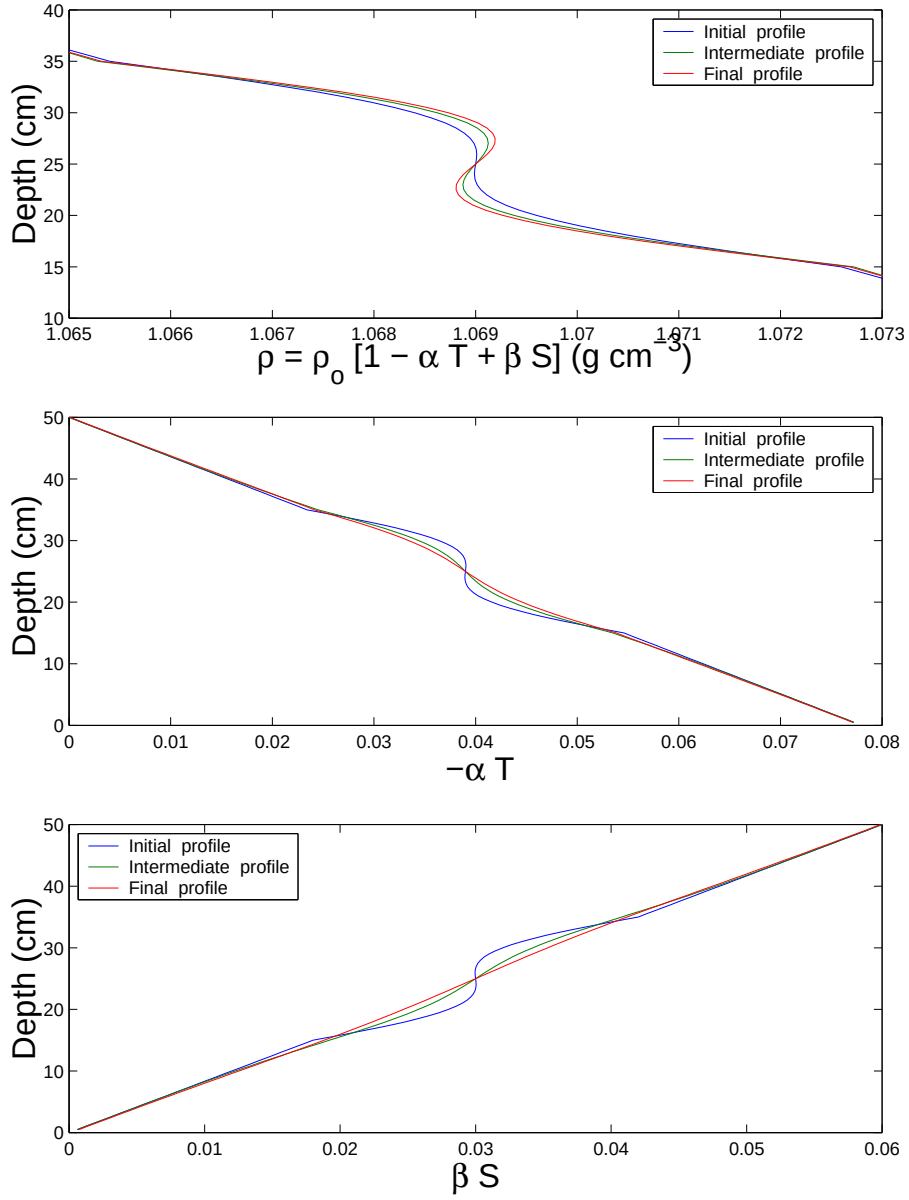

Figure 5.4: A numerical simulation of the evolution of T and S gradients due to salt fingers from the initial stratification that is present after a turbulent mixing event of mixing efficiency $M = 0.8$. The curves were obtained by numerically solving equations (1.22) to (1.25) using a semi-implicit Crank Nicholson scheme. The values of T and S were typical of laboratory sugar-salt experiments where $R_\rho = 1.13$.

Another way of representing the evolution of density anomalies is by plotting αT against βS, as shown in figure 5.5. This is plotted in the sugar/salt sense, where increasing the concentration of T (salt), increases the density. Only points from within the partially mixed region are shown in figure 5.5, outside this region there no changes in T and S. All the points initially lie on a line of slope $R_\rho = 1.3$. Mixing by the turbulent patch does not change the initial R_ρ, but changes the spacing of the points along the line of constant R_ρ, reflecting changes in the density gradient. The increased concentration of the points in the center represents the low gradient in the interior of the mixed patch. The high gradient interfaces are represented by the wide spacing of the points. Subsequent evolution of the S and T fields occurs along lines of slope γ, due to equation (1.25). The final slope of points within the patch has $R_\rho = 0.91$, indicating overturning instability of the density gradient. Near the edges of the patch the final R_ρ can be seen to have increased indicating higher static stability in these regions.

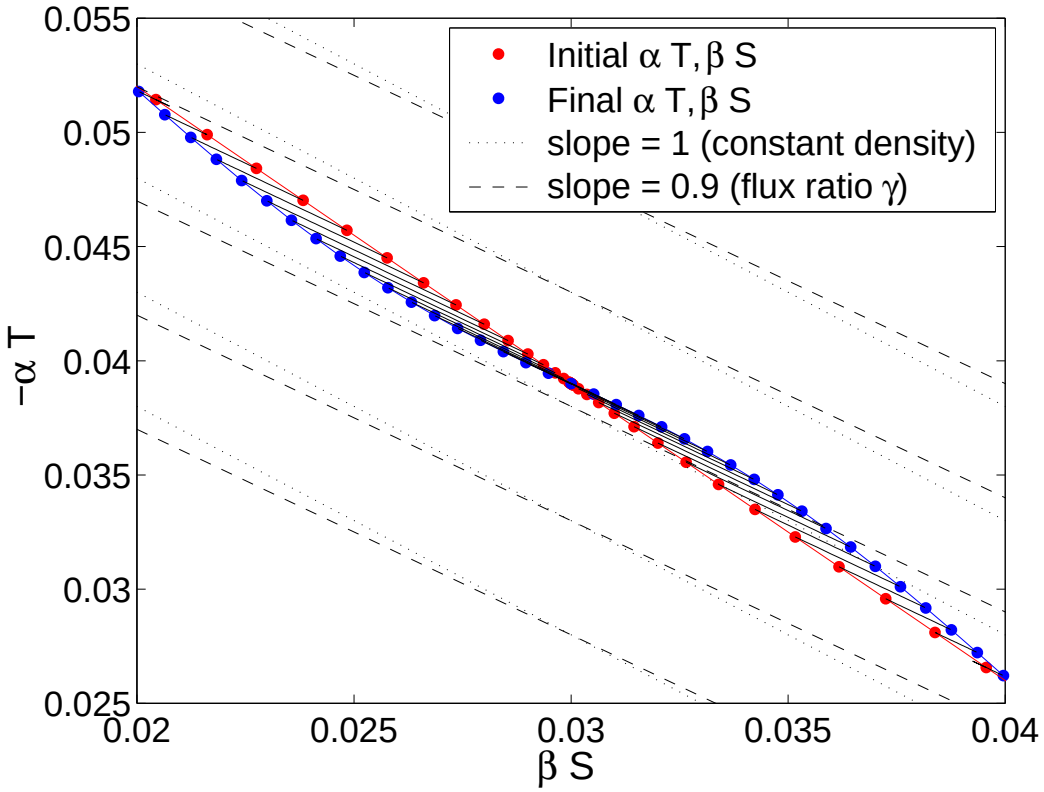

Figure 5.5: A graph showing a numerical solution for the evolution of T and S fields due to salt fingers after a mixing event has locally changed density gradients within a patch. This graph shows the same data as presented in 5.4.

The preceding discussion has ignored the effect that variations of R_ρ have upon on the eddy diffusivity K_S of the S component. In oceanographic observations, St Laurent & Schmitt (1999) found that $K_S(R_\rho)$ is a decreasing function of R_ρ. In our model R_ρ decreases with time in the interior of the mixed patch. Hence K_S in the interior should increase with time. This means that flux divergences can disappear without the S gradient returning to the initial linear gradient. This will decrease the change in T (5.7) so that the ratio (5.8) must increase. We explored this effect in numerical calculations for a case where $K_S = R_\rho^{-2}$ and found small changes from the predictions of (5.8) with the density gradient being slightly more stable than in the case where K_S was constant.

5.2.3 Transition to overturning convection

If the density gradient within the mixed patch is small or zero, there is the possibility that the form of convective instability may change from laminar salt fingers to turbulent overturning convection. We argue that this transition will occur not when the density gradient changes sign but when the turbulent convective velocity W_C is faster than the salt finger velocity W_F, a condition we express as:

$$\frac{W_C}{W_F} > C, \tag{5.9}$$

where C is a constant of order one. When this occurs, large scale convection can sweep away the fingers faster than the fingers extend from the boundaries. We will assume that the rate at which fingers extend into the mixed layer is that same as that defined by (4.20).

The salt fingers in the deep linear gradient above and below the mixed patch provides a constant buoyancy flux into the mixed region. The RMS velocity of convective eddies was found experimentally by Adrian, Ferreira & Boberg, (1986) for a buoyancy flux B and a well-mixed thickness h to scale as

$$W_C = 0.6(Bh)^{1/3}. \tag{5.10}$$

Because the convective eddy velocity (5.10) scales with the thickness h, of the patch we can rearrange (5.9) to give the critical patch thickness where laminar salt finger convection changes to turbulent overturning, as

$$h_{crit} = \frac{(1.66\, C\, W_F)^3}{B}. \tag{5.11}$$

We assume the buoyancy flux B depends only upon the S_z and T_z in the deep gradient regions rather than ΔT and ΔS across the patch. From (4.20) the finger velocity W_F also depends upon K_T and hence B. Once the buoyancy flux B in the linear salt finger gradients is known (as a function of R_ρ), the critical patch thickness h_{crit} can be determined.

An alternative to (5.11) would be to consider a Rayleigh number defined as

$$Ra = \frac{h^4 B}{\nu \kappa_T^2}. \tag{5.12}$$

The Rayleigh number at which the transition from finger convection to overturning convection can be found by substituting (5.11) in (5.12) to give

$$Ra_{crit} = \frac{(1.66\, C\, W_F)^{12}}{B^3\, \nu\, \kappa_T^2}, \tag{5.13}$$

which is not a fixed number, as both W_F and B are functions of R_ρ and S_z. In order to estimate the magnitude of Ra_{crit} we now discuss typical values of these parameters in laboratory experiments, detailed below in in § 5.3. Buoyancy fluxes B are of the order of $10^{-1}\mathrm{cm}^2\mathrm{s}^{-3}$ and a constant of $C = 5$ describes the laboratory observations well. In our laboratory experiments observations from the shadowgraph suggest that velocities are of the order of $10^{-1}\mathrm{cm\ s}^{-1}$. The molecular diffusivity of the T component (salt) $\kappa_T = 1 \times 10^{-5}\mathrm{cm}^2\mathrm{s}^{-1}$, and $\nu = 1 \times 10^{-2}\mathrm{cm}^2\mathrm{s}^{-1}$ so $Ra_{crit} \approx 10^{13}$. This is much larger than the values of $Ra \sim 10^3$ for the transition from molecular diffusion to overturning convecting in the classic Rayleigh-Benard cell, owing in part to the fact that convection in our case must overcome rapid salt finger growth (rather than molecular diffusion in the Benard problem).

5.2.4 Growth of mixed patch due to entrainment

If salt fingers can drive overturning convection then the patch can grow in thickness by entrainment of the overlying density gradient. A fraction of the buoyancy flux released from one unstable boundary is able to entrain part of the density gradient on the opposite boundary. This results in a buoyancy flux into the well-mixed layer of

$$B_e = -\frac{1}{2}\frac{\partial h}{\partial t}\frac{g\Delta\rho}{\rho}, \tag{5.14}$$

where $\partial h/\partial t$ is the rate at which the convecting layer increases in depth. By symmetry both boundaries are growing so there are equal and opposite entrainment fluxes, B_e, and the density in the mixed region remains constant. The density step $\Delta\rho$ at the edges of the well-mixed convecting patch is given by

$$\Delta\rho = \frac{h}{2}\frac{d\rho}{dz}. \tag{5.15}$$

Following Manins & Turner (1977) we express the ratio of entrained flux due to mixing to the salt finger buoyancy flux as

$$\eta = -\frac{B_e}{B}. \tag{5.16}$$

A value of $\eta = 0$ corresponds to no entrainment and maximum experimental values were found by Denton & Woods (1981) to be $\eta \approx 0.25$ for Richardson number of the order of one; for higher Richardson number η slowly decreases.

We will assume the salt finger buoyancy flux B is constant and is driven by the buoyancy flux in the deep linear gradients, rather than by the magnitude of the density step, $\Delta\rho$. Combining equations (5.14), (5.15) and (5.16) gives

$$\frac{\partial h}{\partial t} = \frac{-4\eta B}{hN^2}. \tag{5.17}$$

where N is the buoyancy frequency. The general solution for the time dependence of the mixed layer thickness is

$$h = \sqrt{-8\eta\frac{B}{N^2}(t - t_c)}, \tag{5.18}$$

where t_c is a constant that must be experimentally determined. This growth of a convecting patch is similar to the result derived by Manins & Turner (1977) for the time evolution of a convectively mixed region beneath a linear gradient heated from below.

The growth rate predicted by (5.18) differs from the theory of Stern & Turner (1969) where $h \sim t^{3/2}$. The central difference between (5.18) and Stern & Turner (1969) was their assumption

that fluxes were determined by the size of the S step at the edge of the convecting layer as $F_S \sim \Delta S^{4/3}$, rather than assuming constant fluxes from the deep linear gradients. As a third alternative, if one assumed that the buoyancy flux was proportional to the density step ($B \sim \Delta\rho$), this would imply that $h \sim t$. Thus an experimental determination of the growth rate of the mixed patch will test whether the buoyancy fluxes that cause the entrainment depend upon the uniform gradient S_z or upon $\Delta S^{4/3}$.

5.3 Laboratory experiments

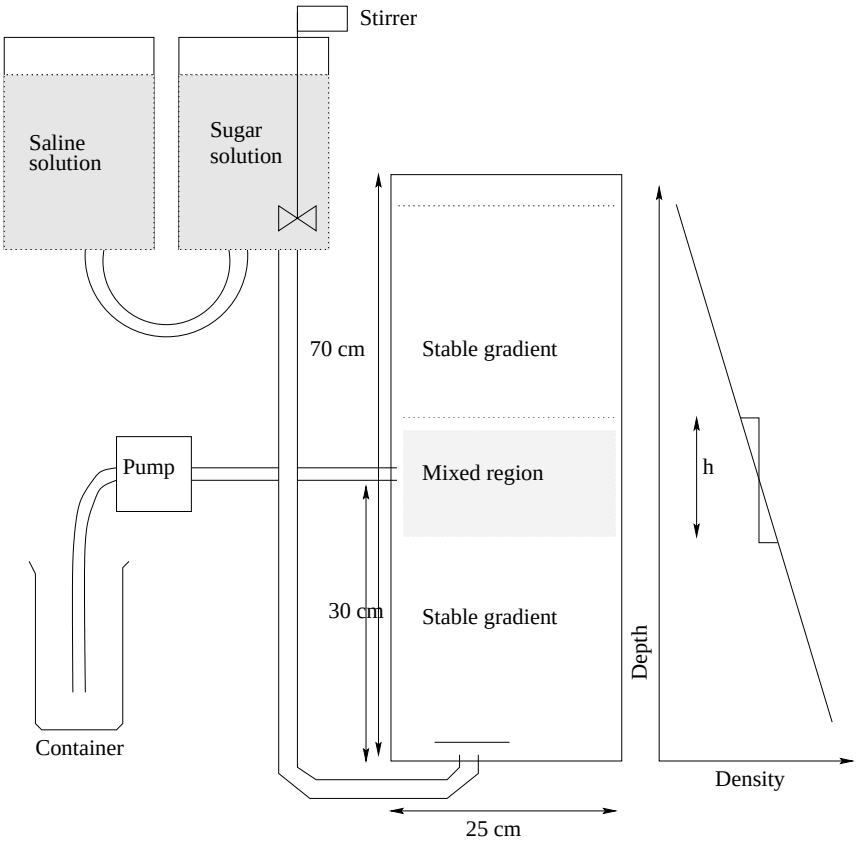

Figure 5.6: The apparatus used in laboratory experiments.

The experimental apparatus used is sketched in figure 5.6. It consisted of a glass tank of depth 70 cm and cross section 25 cm $\times$ 25 cm. Using a double bucket system the tank was filled from the base with linear 'crossed' concentration gradients of T (salt) and S (sugar) to a depth of 60 cm. In all experiments a constant value of destabilizing S gradient was used with

the density of sugar = 1.06 g cm^{-3}. To vary R_ρ between 1 and 2.5 we changed the density of the stabilizing T (salt) solution. At 30 cm depth there was a tube through which a known volume of water could be withdrawn to an external measuring container by a peristaltic pump. This water was then mixed and slowly pumped back in to create a well-mixed patch in the otherwise linear gradient. In some of the initial experiments we used a stirring device at the same 30 cm level to create a partially mixed patch but it was difficult to produce repeatable patch thicknesses. The subsequent development of this mixed patch was viewed using a shadowgraph and results of patch thickness were recorded from time-lapse video images, allowing experiments to be observed for up to 2 days.

5.3.1 Partially mixed patches

The evolution of partially mixed patches with salt fingers was investigated by briefly stirring a linear T and S concentration gradient. By varying the time that this stirring was active (between 1-5 seconds) we could create partially mixed patches that had thickness between 5-12 cm. A sequence of photographs of a laboratory experiment with $R_\rho = 1.2$ is shown in figure 5.7, ordered sequentially from top left to bottom right. Initially there is a linear field of salt fingers, shown in photograph (a). This is briefly stirred for 3 seconds, shown in photograph (b), and 30 seconds later a partially mixed region of thickness 10 cm can seen in (c). Five minutes after the stirring event salt fingers have fully re-established in (d). Between 10 and 12 min the partially mixed patch started to overturn, as shown in (e) and (f). In (g) and (h) the form of convection in the layer is characterized by strong overturning rather than laminar salt fingers and the resulting entrainment can be seen to increase the layer depth. This breakdown of a partially mixed patch is consistent with the numerical evolution of T and S profiles shown in figure 5.4. A number of similar experiments were conducted for different R_ρ. The time scale for overturning was smallest in experiments with low R_ρ. Use of equation (5.6) with the observed patch depths and time-scales of 10 - 30 minutes when $1.13 < R_\rho < 1.7$, implies an effective eddy diffusivity of $K_S = 0.04 - 0.08$ cm^2 s^{-1}. This value of K_S is consistent with later measurements shown in figure 5.12.

To explore the effects of the mixedness on the eventual breakdown to convection (as described by equation 5.8) we changed the intensity and duration of the stirring event. The experiments of De Silva & Fernando (1992) indicated that mixedness increases with the duration

of the stirring. Hence, although we were unable to directly measure the magnitude of M, we may have created more strongly or weakly mixed patches. For small $R_\rho = 1.13$ virtually any amount of mixing could lead to eventual overturning. When these experiments were repeated at $R_\rho = 1.5$ only very vigorous and extended mixing (high M) would lead to an eventual breakdown to convection. These observations are consistent with the predictions of (5.8). Similar observations were made by Turner & Chen (1974) who noted that for R_ρ close to one virtually any mixing of a salt finger gradient could lead to a breakdown to a well-mixed convecting layer. At high R_ρ no amount of mixing would produce a well-mixed convecting layer.

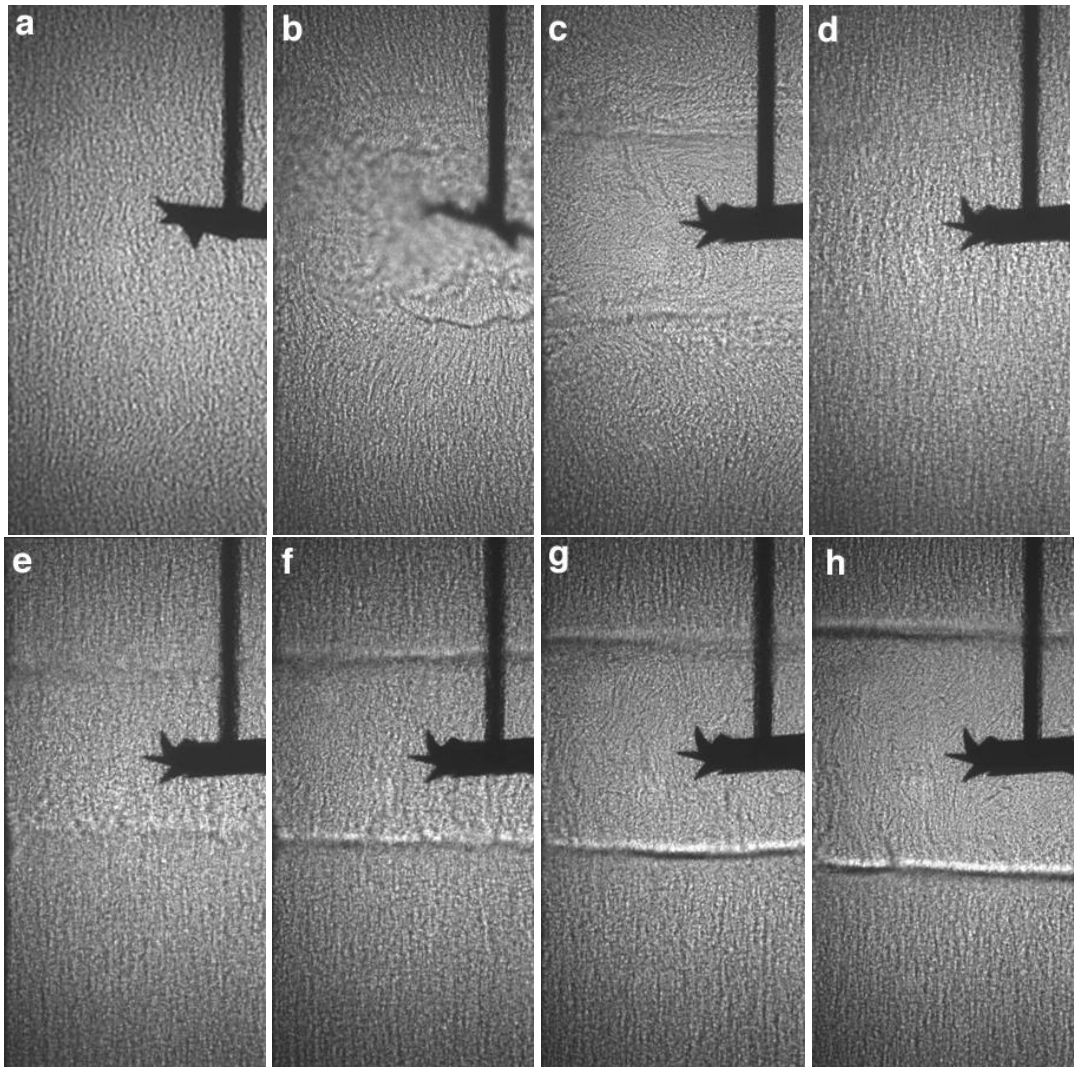

Figure 5.7: Experimental photographs of the development of convection after a brief stirring event in an initially linear density gradient with salt fingers. Initial $R_\rho = 1.2$ and photographs are ordered sequentially from top left to bottom right.

5.3.2 Critical patch thickness

To determine the critical patch thickness for convection to occur (described by 5.11), we systematically varied the size of the initial mixed patch thickness h and R_ρ. All experiments had the same initial S_z. The initial mixed patch thickness was varied by changing the volume of fluid that was withdrawn, mixed and then re-inserted. In figure 5.8 we plot the initial patch thickness h and initial R_ρ and indicate whether or not convection occurred. The experiments fell into two distinct groups; those where $h > h_{critical}$ and overturning convection occurred and subsequently deepened with time (figure 5.9 a) and those where $h < h_{critical}$, where laminar salt fingers were stable and no overturning convection occurred (figure 5.9 b). The prediction of $h_{critical}$ based on (5.11) is plotted in figure 5.8 with experimental values of B/N^2 discussed in the following § 5.3.3. To determine the finger velocity (defined by 4.20) we determine the eddy diffusity K_T in terms of the buoyancy flux by

$$K_T = \frac{B}{N^2}\frac{\gamma}{R_\rho}\frac{R_{\rho-1}}{\gamma-1}, \tag{5.19}$$

and assume $\gamma = 0.9$ for sugar/salt fingers. A good fit to the data is obtained with the constant $C = 5$ in (5.11). The dotted lines bound the experimental uncertainty in B.

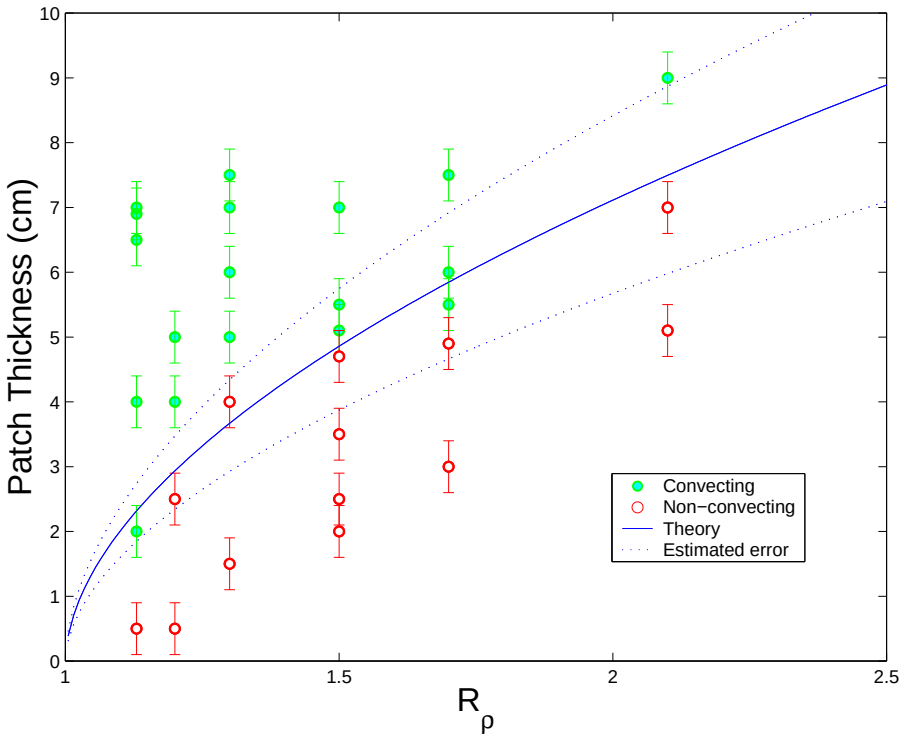

Figure 5.8: Plotted is a summary of initial patch thickness h against initial R_ρ indicating whether the patches started to convect and the prediction of $h_{critical}$ based on (5.11).

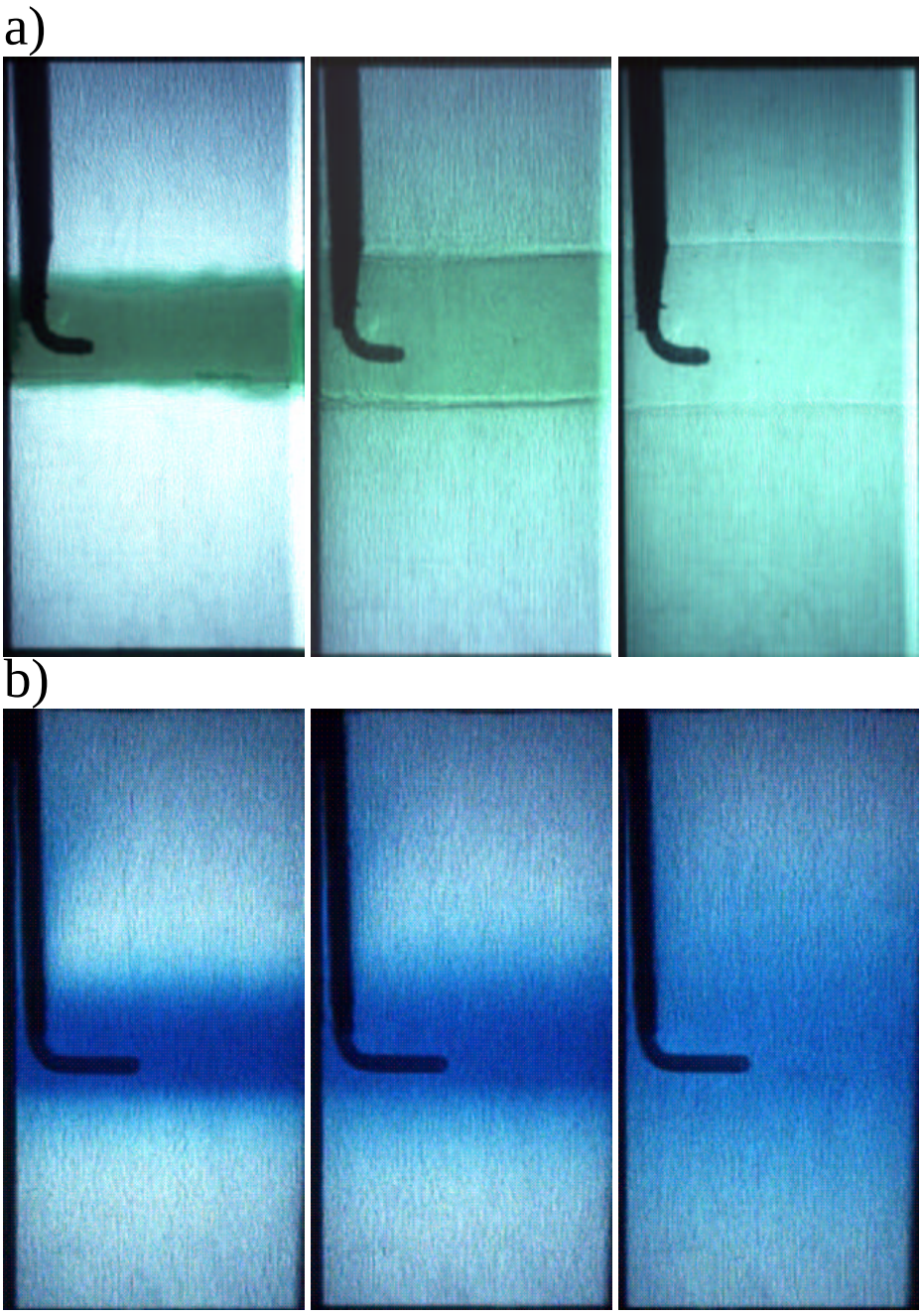

Figure 5.9: a) Experimental photos of patch evolution when $h > h_{critical}$. In this case the initial patch thickness is 6 cm and $R_\rho = 1.7$. Salt finger convection breaks down and starts to overturning, and subsequently deepens with time due to the action of turbulent entrainment. Photographs are taken 20 minutes apart. b) When $h < h_{critical}$ no overturning convection occurs. Here the extracted fluid had been well-mixed and had some dye added before being reinserted to make a patch of thickness 4 cm and $R_\rho = 1.7$. Photographs are taken 20 minutes apart.

To test that the critical thickness $h_{critical}$ depended only upon the density gradient and not on ΔS we conducted several additional experiments. In these experiments a thick mixed patch was created within a linear gradient (as in normal experiments) for R_ρ = 1.13, 1.2 and 1.5. Once the well-mixed patch had started to convect, fluid was withdrawn from the patch so that the patch thickness became less than the critical thickness of (5.11). This is sketched in figure 5.10 (a). The removal of this fluid would not change ΔS. In all cases once enough fluid was withdrawn so that $h < h_{crit}$, the overturning convection ceased and salt fingers re-established themselves across the mixed region, similar to figure 5.9 (b). Thus it seems that the ΔS across the mixed patch does not affect the stability of the convection and that h is the important parameter.

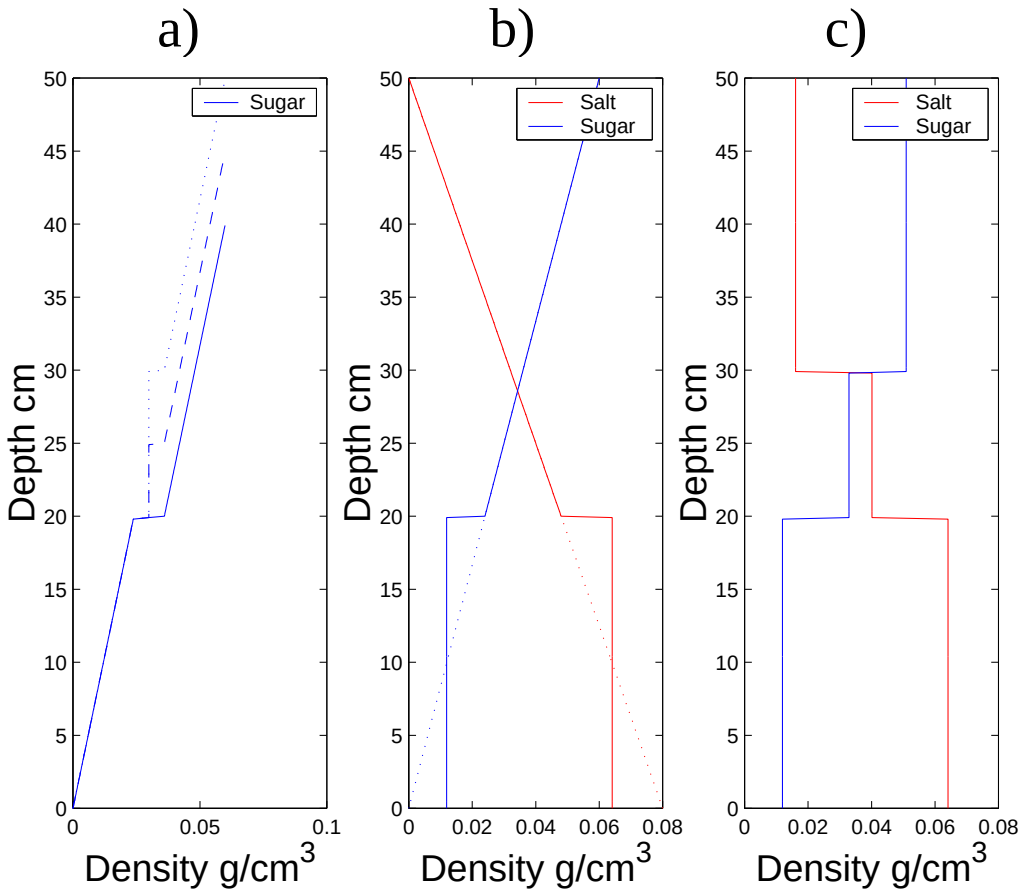

Figure 5.10: A sketch of T and S profiles used in additional experiments; in (a) ΔS across the mixed region remains constant but the thickness h is varied, in (b) the top half of the tank is stratified but the bottom half is well-mixed, in (c) there are three well-mixed layers.

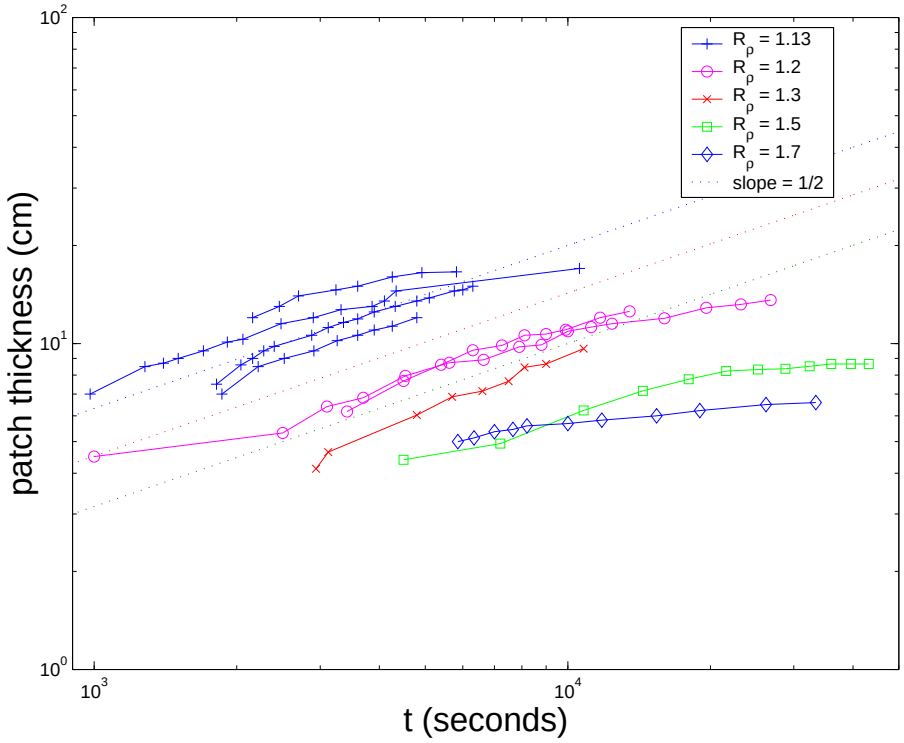

Figure 5.11: A log-log plot of the convecting layer depth h against the time t from onset of convection. The straight dotted lines have slope = 1/2. After several hours the growth decreases below that of a $t^{1/2}$ law as the convecting patch starts to feel the effect of the top and bottom boundaries.

5.3.3 Time evolution of patch thickness

A summary of experimental results of the time evolution of the convecting patch thickness h is shown in figure 5.11 for a range of R_ρ and initial patch thickness. The growth of h is plotted on a logarithmic scale against the time, t, from the onset of convection. In this figure all the straight lines have slope = 1/2. The results show very good agreement with the predicted $h \sim t^{1/2}$ power law (5.18) at small times. At large times the growth drops below the $t^{1/2}$ power law. This is expected to occur as we assumed a constant density gradient in deriving (5.18). At large times the density gradient and R_ρ outside the patch will have increased because the S and T gradients have weakened. The prediction of Stern & Turner (1969) was that a convecting patch would grow as $t^{3/2}$; this is clearly not consistent with the data. For thin 'two sided' interfaces the $\Delta S^{4/3}$ law is a reasonable assumption, but the present results show that it does not describe these 'one sided' interfaces, where there are deep linear gradients next to the sharp interfaces at the edges of the convecting patch. This difference should not be surprising as the

$\Delta S^{4/3}$ flux law was originally derived for sharp interfaces bounded above and below by well-mixed regions where salt fingers can penetrate all the way across the interface and be driven by the ΔS between top and bottom boundaries. In deep linear gradients this will not be the case, as discussed in § 1.2.3.2

Two additional experiments were performed to test other assumptions of (5.18). In the first experiment, 'crossed' linear T and S gradients were made with $R_\rho = 1.5$. The bottom half of the tank was then mixed, as sketched in figure 5.10 b). The depth of the mixed region easily exceeded the criterion of (5.11) and started to convect. However, as there was no buoyant convection from the bottom boundary, there was no entrainment across the interface and the mixed-layer depth remained constant to within 1 cm over a duration of 12 hours. The buoyancy flux of the salt fingers would only act to *increase* the density in this mixed layer and hence increase the stability, rather than drive strong convection that could entrain fluid from the interface. The second experiment used the same density of the T and S solutions as in other experiments but now three well-mixed layers were produced, as sketched in 5.10 (c). In this case convection occurred in all three layers. The interfaces were not observed to move over a 12 hour period. This illustrates the difference between our one sided interfaces above and below a mixed region, and the thin two sided interfaces that occur between the well-mixed regions. These two experiments show that for growth of a mixed layer to occur, there must be smooth gradients above and below the convecting region.

The data from the growth of the layer thickness shown in figure 5.11 can be used to estimate the buoyancy flux of B as a function of R_ρ by rearranging (5.17) to give

$$B = \frac{-N^2 h}{4\eta} \frac{dh}{dt}, \tag{5.20}$$

where $0 < \eta < 0.2$. Only values of h and dh/dt at small times are used to calculate the average value of B. As η is not a well known quantity we made an independent measurement of B by conducting a second set of experiments that measured the rate of change of a linear density gradient due to the 'up gradient' salt finger fluxes. In these experiments we used the same R_ρ and S_z as in earlier experiments but there was no mixed region. The top and bottom boundaries of the tank result in flux divergences that change the local density gradients. Syringe samples of fluid were taken at equally spaced depths through the tank and their densities measured on

an Anton Paar densitometer (model DMA 602). Thus we were able to measure the rate of the change of density gradient with time. The buoyancy flux per unit area due to irreversible processes (such as mixing or salt fingers) is defined by Winters *et al.* (1995) as

$$B = \frac{g}{\rho_o D}\frac{\partial}{\partial t}\left(\int \rho\, z\, dz\right), \tag{5.21}$$

where D is the depth of the tank, g is the acceleration due to gravity and ρ_o the mean density. The buoyancy flux defined by (5.21) is an averaged value within the tank. In figure 5.12 we plot experimental values of a Nusselt number, defined as

$$Nu_B = \frac{-B\rho_o}{g\kappa_T \alpha T_z}, \tag{5.22}$$

where κ_T is the molecular diffusivity of the T component (salt). Typically we would calculate B from the average for 5 - 7 density profiles. The large error bars represent the scatter in the determination of the rate of change of density profiles. The error was mainly due to the difficulty in accurately measuring the small changes in density caused by the low fluxes. The buoyancy flux could be measured more accurately if many repeated, continuous density profiles could be taken rather than with interpolating between 10 density samples to determine the profile. At present it is very difficult to record continuous density profiles using the sugar/salt system.

The Nusselt numbers inferred from (5.21) are in close agreement with those inferred from (5.20), if $\eta = 0.2$. This close agreement shows that the buoyancy flux into the well-mixed region is the same as the buoyancy flux in the linear gradients, rather than being controlled by the density step. An empirical formula for Nu_B that fits the data shown in (5.12) is

$$Nu_B = (11 \pm 3)(R_\rho - 1)^{-1.8}, \tag{5.23}$$

for the range $1.13 < R_\rho < 1.7$.

5.3.4 Comparison of laboratory results with numerical simulations of salt fingers

Recent advances in available computational power have meant that direct numerical simulations of salt fingers are now possible. Stern & Radko (1998) and Radko & Stern (1999)

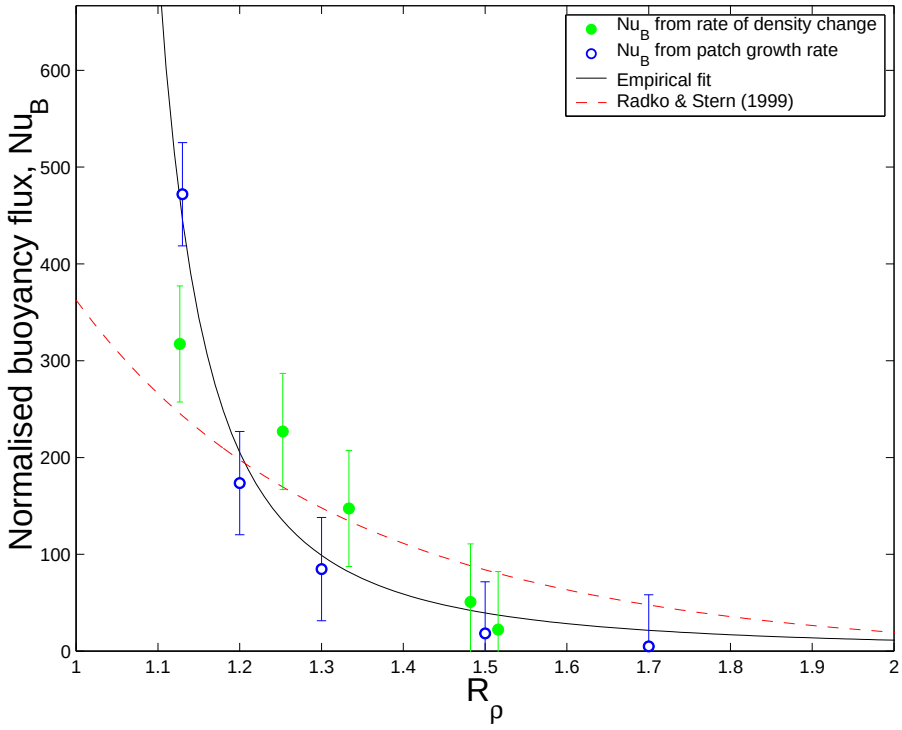

Figure 5.12: A plot of the inferred Nusselt number Nu_B, as a function of R_ρ. Plotted are experimental values of Nu_B determined from the growth of patch thickness with time (5.20), assuming $\eta = 0.2$, and values of Nu_B determined from the rate of change of potential energy of a linear salt finger gradient. The predictions of Radko & Stern (1999) are also plotted along with an empirical fit to our data.

carried out 2D and 3D simulations of sugar/salt finger fluxes in linear T and S gradients, for $2 < R_\rho < 3$. The numerical studies found that the eddy diffusivities K_S and K_T are decreasing functions of R_ρ.

The empirical form of Radko & Stern's (1999) Nusselt number for buoyancy, over the range $2 < R_\rho < 3$ is

$$Nu_B = 84\left(\frac{1}{\tau R_\rho} - 1\right)^{2.11}, \tag{5.24}$$

where $\tau = \kappa_S/\kappa_T = 1/3$ for sugar/salt. An extrapolation of this empirical result to lower values of R_ρ is plotted in figure 5.12. There appears to be good agreement, except at $R_\rho = 1.13$ when (5.24) fails to predict the increase of Nu seen in (5.23) as $R_\rho \to 1$.

5.4 Discussion

Whenever salt fingers are present in the ocean they will experience a background of external shear and intermittent turbulence. Hence the dynamics discussed in this paper are expected to be relevant. A partially mixed patch can become gravitationally unstable due to salt fingers when the initial R_ρ and mixedness, M satisfy the criterion of (5.8). A typical wave breaking event has a mixing efficiency of converting kinetic energy into potential energy of around 25 %, equating to a mixedness $M \approx 0.75$ (Hughes 1996). Using (5.8) this implies that partially mixed patches can become gravitationally unstable for $R_\rho < 2$, assuming heat-salt fingers have $\gamma = 0.6$. Using (5.11) we can estimate a critical patch size for oceanographic conditions. A typical value for buoyancy frequency for much of the oceanic thermocline is 0.02 s^{-1} and measurements of eddy diffusivity due to salt fingers from the NATRE site by St Laurent & Schmitt (1999) found $K_\rho = B/N^2$ in the range of 10^{-4} to $10^{-5} m^2 s^{-1}$. If we assume that the constant $C = 5$ in (5.11) applies to heat/salt fingers, then in the ocean the critical patch thickness is of the order $h = 1 - 10$ m for overturning convection to occur. Typical depths of mixed patches at the NATRE site were found by Polzin *et al.* (2001) to be in the range 1 - 10 m. Hence we expect that these patches may start convecting due to the salt finger fluxes. As K_T is a decreasing function of R_ρ, the critical patch thickness will tend to increase with R_ρ, thus only for R_ρ near 1 do we expect to see convecting patches forming.

In the ocean a turbulent patch will collapse laterally, as opposed to patches in our laboratory experiments which were confined by the walls of the narrow tank. We have shown that if the patch can start to convect then the patch thickness can increase in thickness with time. For patches of small aspect ratio, which behave locally as layers, this convective entrainment could balance the decrease in thickness of a patch as it collapses laterally. Such a balance would lead to mixed patches of small aspect ratio which would spread laterally at an increased velocity due to the sustained input of volume by convective entrainment. Polzin *et al.* (2001) inferred from their observations that collapsing mixed patches were an important mechanism for enhanced lateral dispersion of an anthropogenic tracer in the NATRE site.

After a turbulent event the collapse of the patch is initially governed by a buoyancy-inertia balance (Turner, 1973) so that the lateral intrusion propagates at wave speed U given by

$$U = Nh, \tag{5.25}$$

where h is thickness of the well-mixed patch and N is the buoyancy frequency of the surrounding stratification. For radial collapse of a cylindrical volume of radius R this corresponds to a volume flux of $2\pi RNh^2$. The volume flux into the horizontal surfaces of the cylinder due to the entraining convection, is given by $\pi R^2 dh/dt$. Using (5.17) with $\eta = 1/4$ to determine dh/dt, a steady h can occur when the patch has a radius

$$R > \frac{2N^3h^3}{B}. \tag{5.26}$$

An experiment designed to test (5.26) in the laboratory was carried out in a long narrow tank of length 150 cm, width 10 cm and depth 50 cm. A small stirring device was located at one end to create a mixed patch. However, even with the smallest buoyancy frequency N, smallest convecting depth h and most active salt fingers (large B) the resulting lateral intrusion from the collapsing turbulent patch reached the far end of the tank well before the layer started to thicken by convective entrainment. With realistically achievable laboratory parameters for N, h and B, we would need a tank of length ≈ 10 m to test the balance implied by (5.26).

Using plausible oceanographic values of $N = 0.02\ \mathrm{s}^{-1}$, $h = 1-5$ m, and $K_\rho = 10^{-4}\mathrm{m}^2\ \mathrm{s}^{-1}$ we would expect the condition (5.26) to be important when the radius R of the well-mixed collapsing patch is of the order of 200 m - 1000 m. This large horizontal length scale would only be detectable if one could measure the horizontal coherence of mixed patches. Observations made by Mack (1989) using a towed micro-structure chain in the Sargasso Sea revealed small aspect ratio patches of turbulence and salt fingering having horizontal scales of the order of 100 m - 1000 m. These scales are possibly consistent with the present mechanism. Intrusions of similar lengths scales have also been detected due to other mechanisms such as cross frontal exchange flows (Ruddick & Herbert 1988, Alford & Pinkel 2000b).

5.5 Conclusion

A theoretical and experimental model of the interaction of a patch of turbulence in a deep linear salt fingering gradient has been developed. The initial instability of the salt finger flux

divergences acting upon a partially mixed density gradient is shown by (5.8) to lead to an unstable density gradient for initial R_ρ near one. This unstable patch could subsequently start to convectively overturn if large convective eddies are able to transport T and S faster than salt fingers. This implies that there is a critical thickness of a mixed patch below which overturning convection does not occur. The theoretical description of the critical patch thickness (5.11) is in very good agreement with laboratory results.

Once a patch started to convectively overturn in the laboratory experiments the patch thickness was observed to increase by entrainment of the overlying linear density gradient. Measurements of the growth rate of the patch are in good agreement with the prediction of $h \sim t^{1/2}$. This is in contrast to theory of Stern & Turner (1969) who predicted that a patch of salt fingering will grow as $h \sim t^{3/2}$ based upon the assumption that fluxes scale as $\Delta S^{4/3}$, where ΔS is the difference of the unstable S component cross the mixed patch.

Using the theoretical prediction of patch growth rate (5.18) we have inferred the buoyancy flux of buoyancy B as a function of R_ρ (shown in figure 5.12). These results agreed well with independent measurements of B made by measuring the rate of change of density gradient in linear T and S gradients. This indicates that the fluxes in the mixed region are controlled by the linear gradients above and below the mixed region rather than the density step across the interface. We found B was a rapidly decreasing function of R_ρ, consistent with inferences from oceanographic observations of St Laurent & Schmitt (1999) and numerical studies (Shen 1995; Radko & Stern, 1998; Stern & Radko; 1999, Merryfield 2000 and Radko & Stern, 2000). Our measurements of B at $R_\rho < 2$ are of similar magnitude to predictions of a 3D numerical simulation of salt fingers by Radko & Stern (1999).

In an oceanographic setting our theory predicts that salt fingers can lead to unstable density gradients of partially mixed patches when $R_\rho < 2$. If the patch has thickness greater than 2-5 m, laminar salt-finger convection may give way to overturning convection. Once this occurs the growth rate of the patch thickness due to convective entrainment may balance the decrease in patch thickness due to lateral collapse when a patch is of the order of 200 m - 1000 m radius. The salt finger fluxes thereby enhance horizontal transport in regions of intermittent turbulence and may provide a mechanism for the initial formation of density staircase structure.

Chapter 6

Interaction between salt finger convection and intermittent turbulence

In this chapter we develop a model of the diapycnal fluxes due to the combined presence of intermittent turbulence and salt fingers. We focus on the disruptive effect that frequent turbulent events has upon salt fingers and consider the case where sharp density steps do not form, as was discussed in chapter 5. In §6.1 we review the previous laboratory experiments and results from direct numerical simulations of the initial growth and equilibration of salt fingers. In §6.2 we describe the time averaged buoyancy flux due to the presence of both intermittent turbulence and salt fingering. An experiment is then discussed in §6.3 where the time between turbulent events is systematically varied relative to the growth period of the salt fingers and the resulting average buoyancy flux measured. In §6.4 we use realistic oceanographic parameters to determine the resulting T and S diffusivities when both turbulence and salt fingering are present. We then compare this with previous *ad hoc* parameterizations of salt fingering diffusivities that have been used in ocean circulation models.

6.1 Previous work

In laboratory experiments, Linden (1971) found that continuous turbulence totally disrupted salt finger convection, resulting in 'down gradient' buoyancy fluxes. However experiments of Taylor (1991) found that after a turbulent event, salt fingers can grow and re-establish an 'up gradient' buoyancy flux. In these experiments a grid was dropped through a heat/salt

interface. By taking rapid horizontal and vertical conductivity and temperature profiles, the evolution of the wavenumber spectra was observed. Active turbulence was observed to stop after $Nt = 1$, and characteristic salt finger wave numbers were observed to form by $Nt = 10$, which corresponds to one *e*-folding period of the salt fingers. By calculating a Cox number from the wavenumber data, Taylor deduced that fingers reached equilibrium structures after 5-10 *e*-folding periods. In the ocean there are large regions that are salt finger favourable. Turbulence occurs intermittently in the ocean (Gregg, 1987) and so will disrupt salt finger fluxes. However if the time between turbulent events is greater than the time salt fingers take to re-establish themselves, then salt fingers may contribute significant diapycnal fluxes.

6.1.1 Equilibration of salt fingers

After salt fingers have been disrupted, the initial growth of the salt fingers' velocity, T and S anomalies is exponential (Stern, 1969; Schmitt, 1979a; Kunze, 1987). For given T and S gradients, the growth rate depends upon the wavelength of the salt fingers. The fastest growing fingers have a width that is set by a balance between lateral diffusion of T (which produces the buoyancy perturbation driving the anomaly) and the viscous dissipation generated by the shear between up and down going fingers. The growth rate of the fastest fingers is plotted as a function of R_ρ in figure 6.1. Exponential growth does not continue indefinitely and the flux of T and S becomes limited by secondary instabilities that grow on the salt fingers. Many secondary instabilities have been recognized, such as the "collective instability" of Stern (1969) and other "varicose" instabilities of Holyer (1984, 1985), Howard & Veronis (1987), Veronis (1987) and Shen (1995). For active fingers at low R_ρ, these instabilities have vertical wavelengths comparable to the finger width and growth rates that are only slightly lower than those shown in figure 6.1. In a laboratory experiment, Taylor (1993) made a comparison of vertical and horizontal wave numbers and showed that the salt fingers were characterized by small aspect ratio'blobs' rather than long 'fingers'. Thus we expect active salt fingers to reach equilibrium fluxes after several *e*-folding times (λ^{-1}) and at small aspect ratio.

Salt finger fluxes only grow exponentially for a small time and no analytic description is available for the subsequent evolution to steady fingers. Direct numerical simulations of salt fingers in linear T and S gradients have modeled the brief initial period of exponential growth and the subsequent equilibration of salt fingers fluxes at large times. The two-

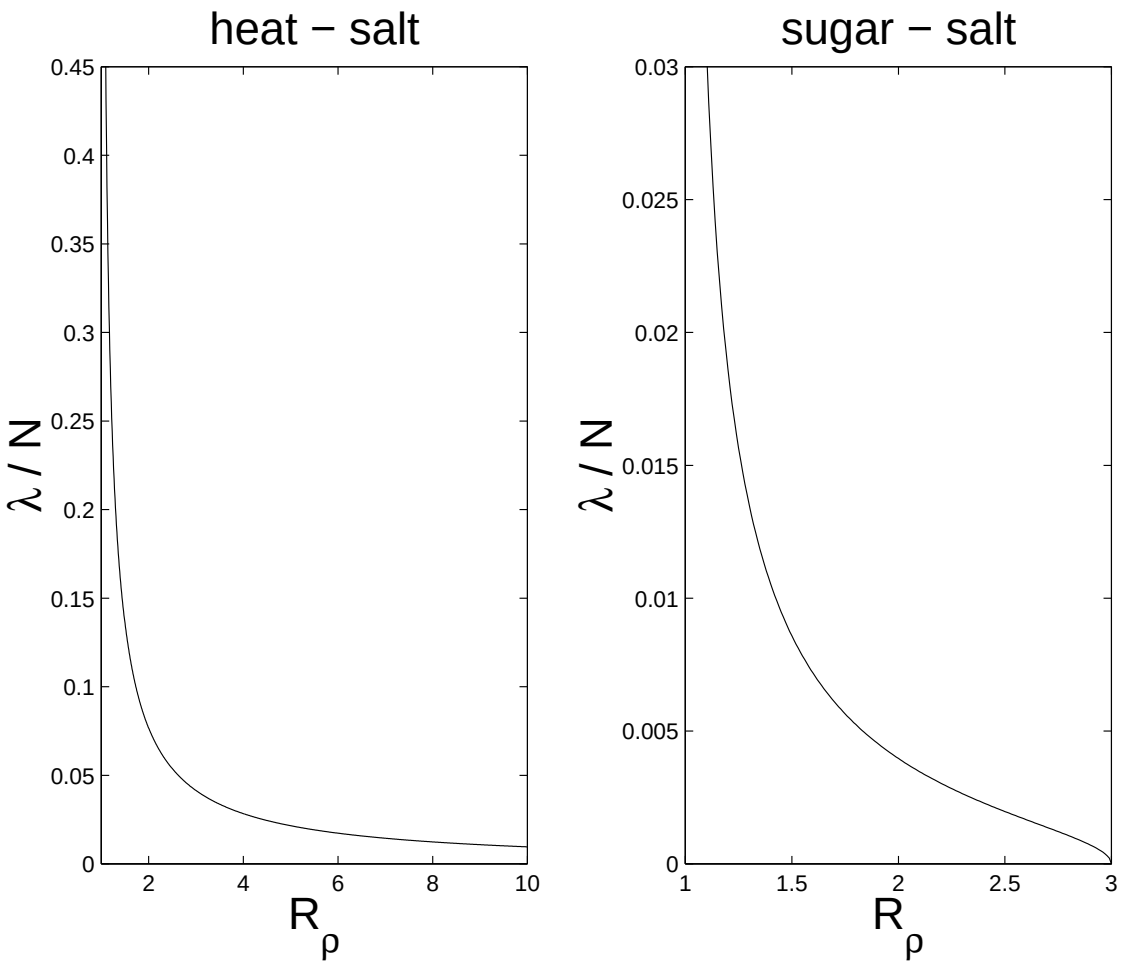

Figure 6.1: A plot of the (1.12), exponential growth rates λ of salt fingers normalized by the buoyancy frequency N, for the heat/salt and sugar/salt case.

dimensional heat/salt simulations of Shen (1995) and Merryfield & Grinder (2001) and the three-dimensional sugar/salt simulations of Radko & Stern (1999) all found similar results for the time-dependence of the salt finger fluxes over the range $1.25 < R_\rho < 15$ for heat/salt fingers and for $1.6 < R_\rho < 3$ for sugar/salt fingers. Results from these models showed that when the velocity, and T and S anomalies are initially very small the growth rate is very similar to the predicted exponential growth rate, described by (1.12). Subsequently the growth rate reduces and then steady velocity, T and S anomalies are reached at around 3-7 e-folding periods. The difference in the timescales to equilibration of the various numerical models depends in part upon the magnitude and structure of the initial 'white noise' that the linear T and S fields are seeded with.

The time evolution of salt finger fluxes is plotted in figure 6.2 (a) from a numerical simulation by Merryfield & Grinder (2001). In this graph, the T flux has been normalized in the form of a Nusselt number

$$Nu = \frac{F_T}{\kappa_T T_z}, \tag{6.1}$$

where κ_T is the molecular diffusivity of T. The three different curves are for R_ρ = 2, 6 and 15, so that the exponential growth rates vary. When time is normalized by the salt finger growth rate, λ, the three curves all reach equilibrium values of Nu at around 4-5 e-folding periods after the initiation of the growth from linear T and S gradients. These equilibrium values of Nu are very similar to those found by Shen (1995) for similar R_ρ. In figure 6.2 (b) the numerical data are plotted on logarithmic axes. When Nu is growing to equilibrium values the three curves closely follow a t^7 power law. Similar steep growth was found in the evolution of sugar/salt salt finger fluxes in the numerical experiments of Radko & Stern (1999) where a similar steep approach to equilibrium values over approximately 7 e-folding periods was seen. The growth of Nu in figure 6.2 (a) is also consistent with exponential growth at small times, however the exact functional form of this growth will be relatively unimportant in the following discussion.

6.2 Interaction between intermittent turbulence and salt fingers

In this section we discuss how the buoyancy fluxes due to salt fingering and intermittent turbulence vary with time. By averaging these time dependent buoyancy fluxes over large timescales we describe how the total buoyancy flux depends upon the time between turbulent events and the e-folding period of the salt fingers.

6.2.1 Salt finger fluxes

After a turbulent event has disrupted the salt fingers fluxes, salt fingers re-establish themselves over several e-folding periods. For simplicity in the following discussion we propose an empirical parameterization of the growth of salt fingers based upon the numerical results shown in figure 6.2. The fluxes are parameterized as having an initial growth which follows a

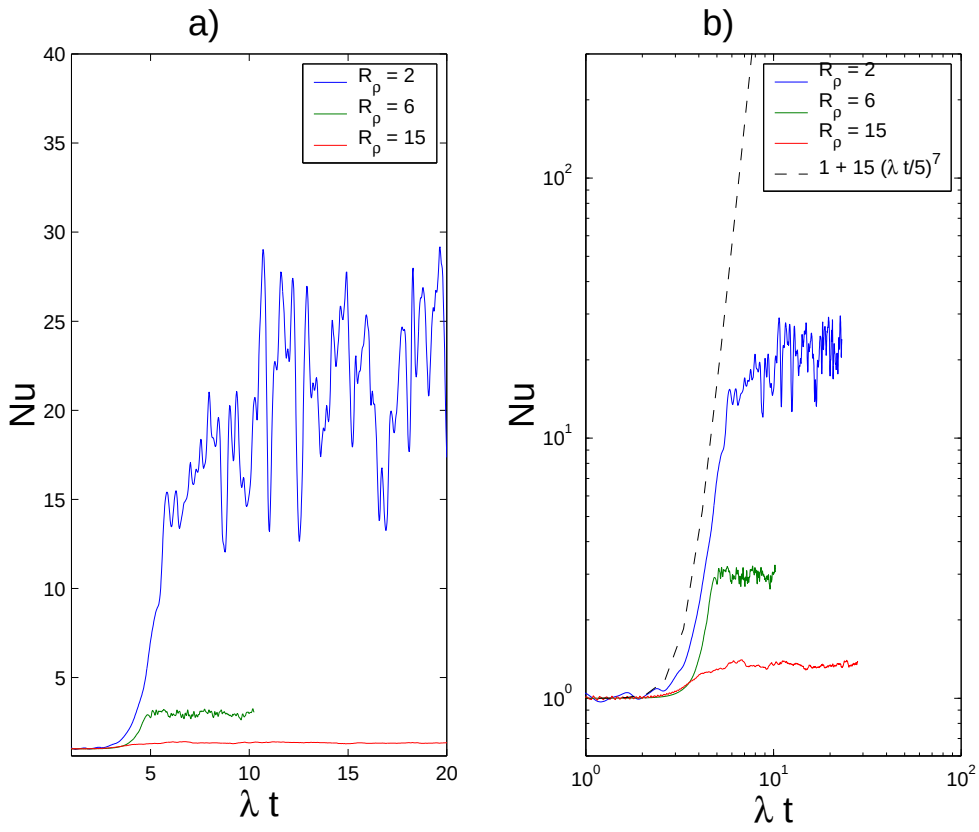

Figure 6.2: The normalized T flux Nu, due to salt fingers plotted against time normalized by the initial exponential growth rate λ plotted on linear and logarithmic axes; data from the numerical simulations of Merryfield & Grinder (2001).

t^7 power law which equilibrates after 5 e-folding periods

$$Nu(t) = \begin{cases} 1+(Nu^*(R_\rho)-1)(\lambda t/5)^7 & \text{if } t < 5/\lambda \\ Nu^*(R_\rho) & \text{if } t > 5/\lambda, \end{cases} \tag{6.2}$$

where Nu^* is the equilibrium value. The exact functional form of (6.2) will be shown to be relatively unimportant. The time dependent parameterization of (6.2) is plotted in figure 6.3 (a). The initial growth rate λ is a strongly decreasing function of R_ρ (as shown in figure 6.1) so that for higher R_ρ Nu takes longer to reach the equilibrium values Nu^*. The dimensionless S flux is $Nu_S = \gamma^{-1}Nu$, where γ is the flux ratio.

The time average of $Nu(t)$ over a time Δt, beginning at the time of zero salt finger amplitudes, is given by

$$\overline{Nu} = 1/\Delta t \int_0^{\Delta t} Nu(t)dt, \tag{6.3}$$

where the over-bar denotes a time averaged quantity. The instantaneous and time-averaged fluxes (6.2, 6.3) are plotted in figure 6.3. The instantaneous Nu reaches the equilibrium value Nu^* at 5 e-folding periods, while $\overline{Nu}$ reaches half Nu^* at around 9 e-folding periods. Virtually the same result for $\overline{Nu}$ would occur if we used a step function to describe (6.2) rather than assuming a polynomial growth. For the case of a step function, the time average value would reach half the equilibrium value at 10 e-folding periods. This means that as long as there is a steep growth in Nu the exact details of the functional form are not important for the time-averaged $\overline{Nu}$; only the time taken for the salt fingers to equilibrate and the equilibrium value of Nu^* are important.

The important point of figure 6.3 (b) is that $\overline{Nu}$ can be considered as a time-average over many cycles of disruptive events. If turbulence disrupts salt fingers every 5 e-folding periods, then $\overline{Nu}$ is only 10% of Nu^*. If turbulence disrupts salt fingers every 9 e-folding periods, then $\overline{Nu}$ will be half the equilibrium values. Only in the limit of very long times between turbulent events will $\overline{Nu} = Nu^*$. This indicates that the time-averaged fluxes of salt fingers are very sensitive to the time between intermittent turbulent events and will be greatly reduced if turbulence occurs frequently.

6.2.2 Turbulent fluxes

Observations of turbulence in stratified flows have found that the buoyancy flux due to the turbulence is suppressed after one buoyancy period (Itsweire *et al.* 1986; Hughes 1996). On timescales much greater than one buoyancy period ($t \gg 2\pi/N$) we can consider a turbulent stirring event to be an instantaneous event. The time-averaged flux will then scale with the time Δt between turbulent events.

If the time-averaged flux due to the turbulent event over the period $2\pi/N$ has the value F_{Turb} and the time between turbulent events is Δt then the time-averaged flux will scale as

$$\overline{F}_{Turb} = \frac{2\pi}{N\Delta t} F_{Turb} \tag{6.4}$$

where N is the buoyancy frequency. If turbulence is highly intermittent, the time-average

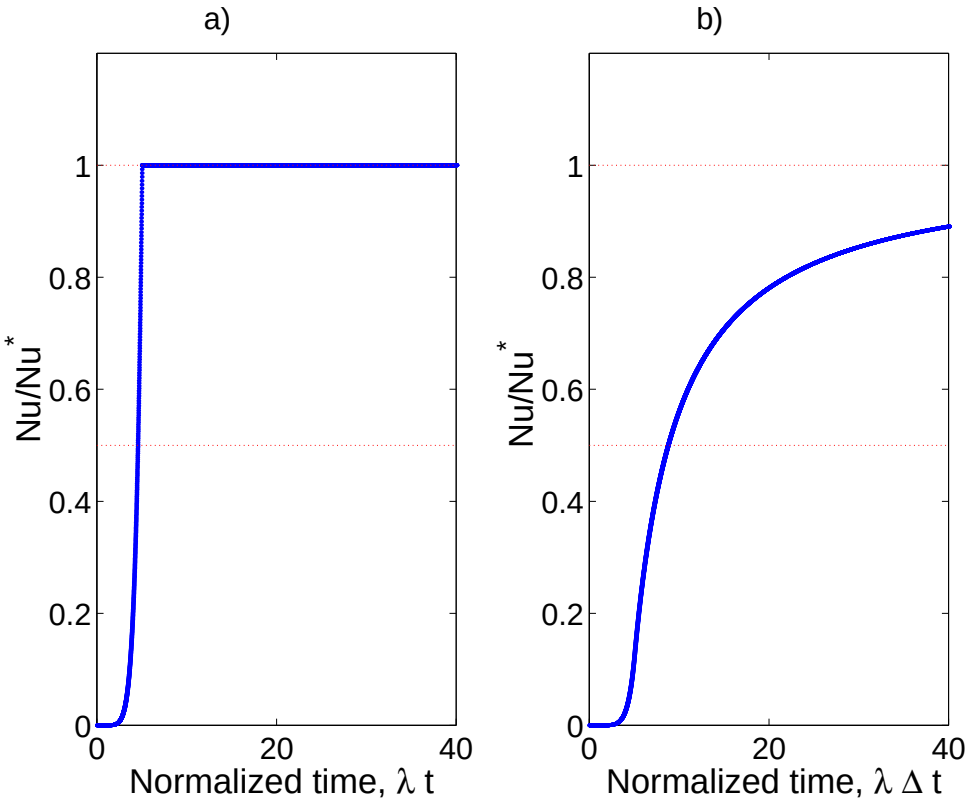

Figure 6.3: a) A plot of the evolution of the salt finger flux Nu, defined by (6.2), against time: b) The evolution of the time-averaged salt finger flux $\overline{Nu}$, defined by (6.3), against the time between stirring events Δt, time normalized by λ.

turbulent flux, $\overline{F}_{Turb}$, is much less than the turbulent flux F_{Turb} during a turbulent event. The same $\overline{F}_{Turb}$ can result from strong but infrequent turbulence (large F_{Turb} and large Δt) as for weak but frequent turbulence (small F_{Turb} and small Δt). In the laboratory the time between turbulent events Δt and the magnitude of F_{Turb} are constant; in the ocean average values of Δt and F_{Turb} would have to be used.

The assumption that $\overline{F}_{Turb}$ scales linearly with the time between events for a given F_{Turb} will only hold if the density gradient remains essentially linear so that the buoyancy flux is uniform through the depth of the tank. The growth of low-gradient boundary layers at the top and bottom places one restriction on how large the buoyancy flux due to turbulence can be. Density staircase structure can also occur if stirring is near Richardson numbers of unity (Ruddick *et al.* 1989; Park *et al.* 1994 and Holford & Linden 1999).

6.2.3 Addition of salt fingers and turbulence

On large timescales ($t \gg \Delta t \gg 2\pi/N$) the time-averaged buoyancy fluxes due to the combined presence of both salt fingers and turbulence is determined by addition of (6.3) and (6.4). These equations have taken into account the disruption of salt finger fluxes by turbulence and represent average fluxes over many cycles of turbulence and growing salt finger fluxes. The buoyancy flux due to both processes is

$$\overline{B} = g(\alpha\overline{F}_T + \beta\overline{F}_S), \tag{6.5}$$

and will be negative when salt fingers dominate and positive when turbulence dominates.

At large Reynolds numbers turbulence T and S are transported with the density gradient so that $\alpha\overline{F}_{T\ Turb} = R_\rho\beta\overline{F}_{S\ Turb}$. The time-averaged fluxes of T and S are

$$\begin{aligned} \beta\overline{F_S} &= \beta\,\overline{F}_{S\ Finger} + \beta\,\overline{F}_{S\ Turb}, \\ \alpha\overline{F_T} &= \gamma\,\beta\,\overline{F}_{S\ Finger} + R_\rho\beta\overline{F}_{S\ Turb}, \end{aligned} \tag{6.6}$$

where γ is the salt finger flux ratio, $\overline{F}_{S\ Finger}$ is defined by (6.3) and $\overline{F}_{S\ Turb}$ is defined by (6.4). The assumption that the total flux (6.6) is the sum of the salt finger and turbulent fluxes was also made by Walsh & Ruddick (1998); the important difference is that now the time dependence of the salt finger fluxes is considered.

The ratio of the time-averaged T and S fluxes in (6.6) is

$$\gamma_{eff} = \frac{\alpha\overline{F_T}}{\beta\overline{F_S}} = \frac{\gamma\overline{F}_{S\ Finger} + R_\rho\overline{F}_{S\ Turb}}{\overline{F}_{S\ Finger} + \overline{F}_{S\ Turb}}. \tag{6.7}$$

This had been previously described as the "effective flux ratio" by Walsh & Ruddick (1995b) and defined in terms of eddy diffusivities of T and S. When time-averaged salt fingering fluxes are large, $\gamma_{eff} = \gamma$ and the buoyancy flux is 'up gradient'. When the time-averaged turbulence dominates, $\gamma_{eff} = R_\rho$ and the flux of density is 'down gradient'. For a given R_ρ and γ, the flux ratio γ_{eff} is a function of the time between turbulent events Δt. $\overline{F_S}_{Finger}$ increases with increasing Δt by (6.3), while $\overline{F}_{Turb}$ decreases with increasing Δt by (6.4).

An example of the dependence of γ_{eff} upon the normalized time between turbulent events $\lambda\Delta t$ is plotted in figure 6.4, where we have used a value of $\gamma = 0.9$ and $R_\rho = 1.25$ representative

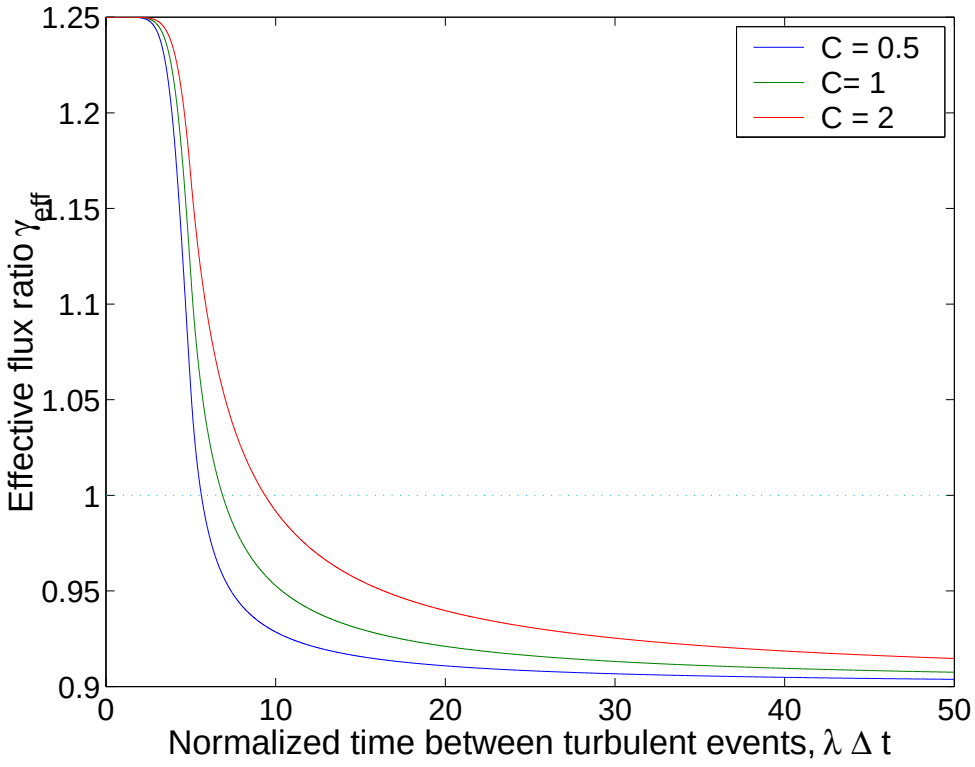

Figure 6.4: The ratio of T and S fluxes (6.7) plotted against the time between turbulent events Δt, normalized by the salt finger growth rate λ. In this figure R_ρ = 1.25 and γ = 0.9, typical of laboratory sugar/salt experiments.

of laboratory sugar/salt fingers. We define C as the ratio of average turbulent flux (evaluated at $\lambda\Delta t = 1$) to the equilibrium salt finger flux

$$C = \frac{\lambda\, 2\pi F_{S\ Turb}}{N\, F^*_{S\ Finger}}. \tag{6.8}$$

Values of C = 0.5, 1 and 2 are plotted in figure 6.4. These values of C are consistent with later laboratory experiments, detailed below in §6.3.2. The transition from an 'up gradient' flux of buoyancy ($\gamma_{eff} < 1$) to the 'down gradient' flux of buoyancy ($\gamma_{eff} > 1$) occurs when the time between turbulent events is $\lambda\Delta t = 7$, for $C = 1$. When $\gamma_{eff} = 1$ there is no buoyancy flux. When $C = 2$ the transition occurs at $\lambda\Delta t \approx 10$ and when C = 0.5 the transition occurs at $\lambda\Delta t \approx 6$. The important feature of figure 6.4 is that when turbulence is frequent compared to salt finger e-folding times (small $\lambda\Delta t$) the turbulence fluxes are large and salt finger fluxes are weak, so that the total flux is dominated by turbulence and $\gamma_{eff} = R_\rho$. When turbulence

is infrequent compared to salt finger *e*-folding times (large $\lambda\Delta t$) the turbulent fluxes are small and salt finger fluxes can reach equilibrium values and dominate the total buoyancy flux, so that $\gamma_{eff} = \gamma$.

6.3 Experiments with intermittent turbulence and salt fingers

To determine how salt fingers fluxes are disrupted by intermittent turbulence, a series of experiments was conducted where the time between turbulent events, Δt, was systematically varied relative to the *e*-folding period of the salt fingers. A comparison of the average buoyancy fluxes from different experiments then allows a determination of the minimum time between stirring events, Δt, necessary for the salt fingers to reach equilibrium fluxes. Two sets of experiments were conducted with different N and R_ρ. The growth rate λ is a function of both N and R_ρ (from figure 6.1) so is varied between the experiments.

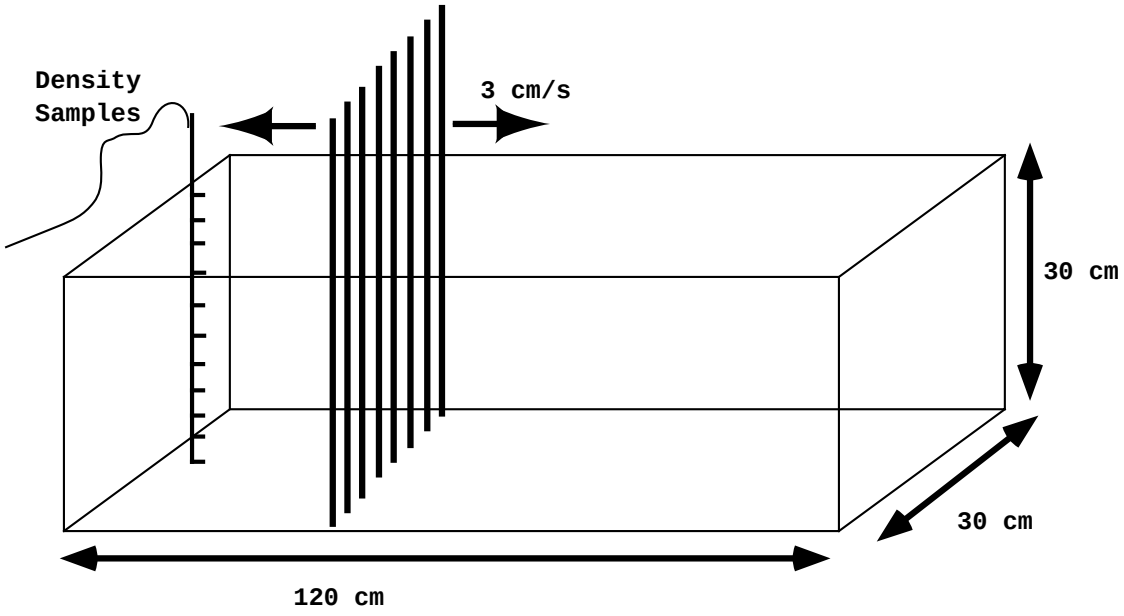

Figure 6.5: The apparatus used in initial experiments.

The first set of experiments were conducted in a long tank of dimensions 30 cm $\times$ 30 cm $\times$ 120 cm, as sketched in figure 6.5. Turbulent stirring was conducted by horizontally towing a vertical comb of 8 rods at a constant velocity through the fluid. The rods had diameter 1.2 cm, and were separated by 3.6 cm, so that the solidity of the comb of rods is 30%, similar to that

used by Holford & Linden (1999). The tow speed and stirring frequency were controlled from a computer using a LABVIEW routine. In the experiments we use a tow speed of 3 cms^{-1} . The time between stirring events, Δt, was varied by changing the time the rods paused at the end of the tank before they changed direction. In typical experiments the tank was stirred up to 20 times during the course of measurements.

A second set of experiments was conducted in a deeper tank of depth 50 cm and area 30 cm $\times$ 30 cm. The first experimental tank was abandoned after seven experimental runs due to difficulties with insulating the large surface area and the presence of long internal waves induced by the stirring. The second tank had half the volume of the first tank and a smaller surface area so that internal waves decay more rapidly (McEwan, 1971). A comb of six vertical rods of diameter 1.2 cm separated by 3.4 cm was used so that the solidity of the comb of rods was again around 30%. In this new experiment we used hollow stainless steel rods of small mass which vibrated less at the start and end of a traverse. In the second set of experiments we again used a traversal speed of 3 cm s^{-1}. Insulation was provided by a sliding plastic cover on the tank.

Using heat/salt fingers is problematic in the laboratory due to the difficulty of maintaining good insulation when using high temperature gradients. The large buoyancy fluxes in the heat/salt system also mean that the T and S gradients change quickly. For these reasons the present experiments were conducted using the sugar/salt analogue. Linear concentration gradient were created using the standard double bucket system. To create "crossed" T and S gradients, favourable for salt finger, one bucket had a salt solution of density $\rho = 1.07$ g cm^{-3} and the other a sugar solution of density $\rho = 1.06$ g cm^{-3}. This gave an initial $R_\rho = 1.13$ and $N = 0.55$ s^{-1}. In the second experiments we used slightly higher salt concentration to give $R_\rho = 1.25$ and the deeper tank meant a lower $N = 0.39$ s^{-1}. Using the equations of Schmitt (1979a) to determine the maximum growth rate, the e-folding period of the salt fingers for the first experiments was $1/\lambda = 25$ s and for the second experiments was $1/\lambda = 60$ s.

The Richardson number of the towed rods is defined as

$$Ri = \frac{N^2}{(U/D)^2}, \tag{6.9}$$

where D is the diameter of rods (1.2 cm), U is the traversal speed (3 cm s^{-1}) and N is the

buoyancy frequency. In the first experiment $Ri = 0.11$ and in the second experiment $Ri = 0.06$. A comparison to previous stirring experiments of Ruddick *et al.* (1989), Park *et al.* (1994) and Holford & Linden (1999) indicates that we are not in the high Richardson number regime where steps would form in the density gradient, as can happen if $Ri \geq 1$.

6.3.1 Experimental determinations of buoyancy flux

We measured the density profile by taking 10 vertically spaced samples of fluid after a number of stirring events, so that a time integrated measure of the buoyancy flux is obtained from the rate of change of density gradient, calculated using (5.21). The samples were spaced more closely near the top and bottom of the tank where the density gradient changes most rapidly due to the presence of the horizontal boundaries. The density of the samples are measured using an Anton Paar densitometer (model DMA 602).

The maximum duration of an experiment was set by the growth of the top and bottom boundary layers due to the no-flux condition. If only turbulence were present these boundaries would be regions of low density gradient. As these grow inwards we can no longer assume that the tank has a uniform buoyancy flux. When only salt fingers are present there is an 'up gradient' flux so boundary layers of increased density gradient are produced along with an increase in R_ρ that acts to reduce buoyancy fluxes through the interior. The time scale for the growth of either of these boundary layers to a thickness h is given by

$$t = h^2/\overline{K_S} \tag{6.10}$$

as discussed in §1.2.4. In the present experiments both turbulent and salt finger diffusivities are $\overline{K_S} = 10^{-2} - 10^{-3}$ cm^2 s^{-1}. The time scale for the boundary layer to grow to 20% of the depth of the tank was of the order of 1-2 hours for the first shallow tank and 7-9 hours in the deeper tank.

The time scale (6.10) constrains how slowly the tank could be filled using the double bucket system. Slow filling is preferable to minimize mixing and create a linear concentration gradient. However as the boundary layers grow the value of R_ρ in the tank increases above the initial value. As a compromise we filled the tank over a 10 minute period. This avoided unnecessary mixing during the filling process and was still less than times implied by (6.10), so

that repeatable gradients can easily be made using the sugar/salt system. This problem could not be avoided in the experiments of Taylor (1991), where the high T and S fluxes of heat/salt fingers meant that the run down time scale was of the order of several minutes - comparable to the time it took to fill his tank.

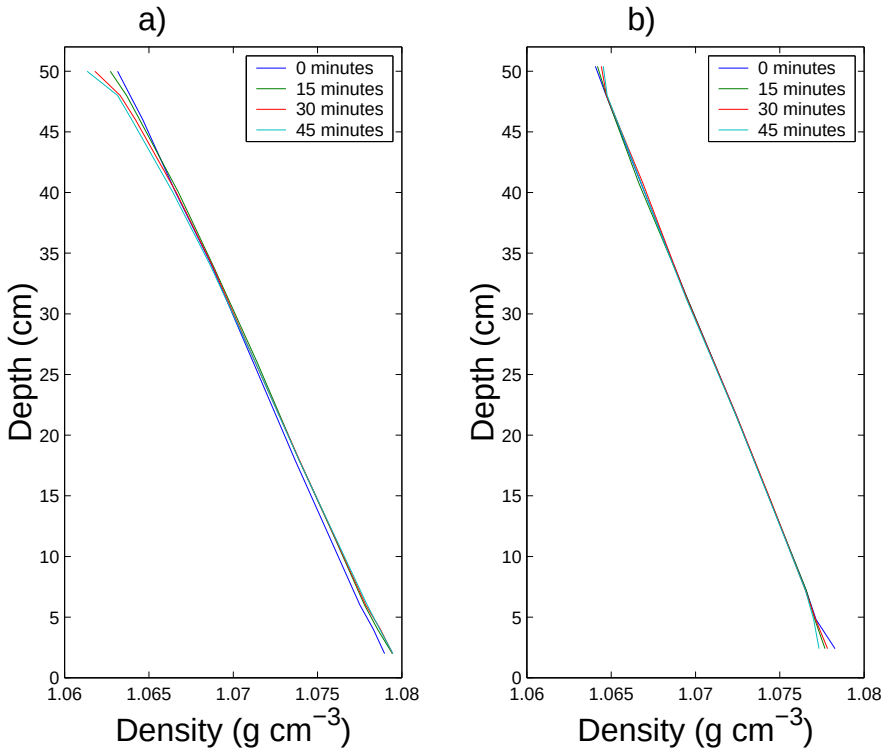

Figure 6.6: Experimental density profiles showing the change in density gradient with time: in a) only salt-sugar fingers are present, in b) only intermittent turbulence is present.

6.3.2 Experimental results

The buoyancy fluxes were calculated from the rate of change of density profiles, using data similar to that shown in figure 6.6. The two cases shown are for experiments where only salt fingers or only turbulence was present. These two experiments had the same initial buoyancy frequency. These density profiles show the difference between the 'up gradient' flux of buoyancy due to salt fingers (figure 6.6 a), that steepen the density gradient with time, and the 'down gradient' flux of buoyancy due to turbulence (figure 6.6 b) that weaken the density gradient with time.

The normalized buoyancy flux is defined as

$$Nu_B = \frac{-B\rho o}{g\kappa_T \alpha T_z}. \tag{6.11}$$

where B is calculated using (5.21) from data such as that shown in figure 6.6. Experimental measurements of depth averaged buoyancy fluxes $\overline{Nu_B}$ are plotted in figure 6.7 for different times Δt between stirring events. As the time between the sampling is greater than the time between turbulent events we have measured the time averaged buoyancy flux. The measured buoyancy flux changes from 'down gradient' to 'up gradient' when $\Delta t \approx 150$ s in the first experiment and when $\Delta t \approx 300$ s in the second experiment. In these figures we also plot the expected turbulent buoyancy flux (6.4) and the equilibrium salt fingering buoyancy flux. Measurements of the density profile were made several times during a typical experiment so as to calculate average values of the rate of change of potential energy. The large error bars in figures 6.7 and 6.8 represent the difficulty in calculating the buoyancy flux using a small number of density samples when the changes in the density gradient are small, as shown in figure 6.6. To determine the equilibrium salt finger buoyancy fluxes two experiments were conducted for R_ρ = 1.13 (not shown) and R_ρ = 1.25 (figure 6.6 a) with no stirring present and buoyancy fluxes again calculated from changes in density gradient with time using (5.21). The average turbulent buoyancy flux was measured for five stirring events for two cases with the same buoyancy frequencies as the salt fingers experiments. The data from one experiment is shown in figure 6.6 (b).

In order to determine the time averaged buoyancy flux of salt fingers, the time averaged buoyancy flux due to turbulence (6.4) was subtracted from the total buoyancy flux. In figure 6.8 the time averaged buoyancy flux due to salt fingers is plotted against $\lambda\Delta t$. The equilibrium and half equilibrium buoyancy flux are plotted in figure 6.8 as horizontal lines. If the instantaneous salt finger buoyancy flux evolves steeply to the equilibrium value then the time averaged salt finger buoyancy flux will reach half the equilibrium buoyancy flux in twice the time it takes the instantaneous buoyancy flux to equilibrate. In these experiments the time averaged buoyancy flux due to salt fingers was seen to reach half the maximum value between 6-15 *e*-folding periods when $R_\rho = 1.13$ and at 10-20 *e*-folding periods when $R_\rho = 1.25$. This implies that the instantaneous flux equilibrated at between 6-10 *e*-folding periods when $R_\rho = 1.13$ and 5-

10 *e*-folding periods when $R_\rho = 1.25$. This time scale is in the same range as the timescales for fluxes to equilibrate in the experimental work of Taylor (1991) and in the numerical work by Shen (1995), Radko & Stern (1999) and Merryfield & Grinder (2001). This agreement of timescales indicates that it was a reasonable assumption in (6.5) to describe the total buoyancy flux as the sum of the time averaged fluxes of turbulence and salt fingers. It would require much more detailed data to determine the functional form of the instantaneous salt finger flux from these time averaged measurements, as the large error bars mean that the curves shown in figure 6.8 cannot be accurately differentiated to infer the instantaneous diffusivity. However it is not important to know the instantaneous fluxes as the time averaged fluxes are not sensitive to its functional form.

a)

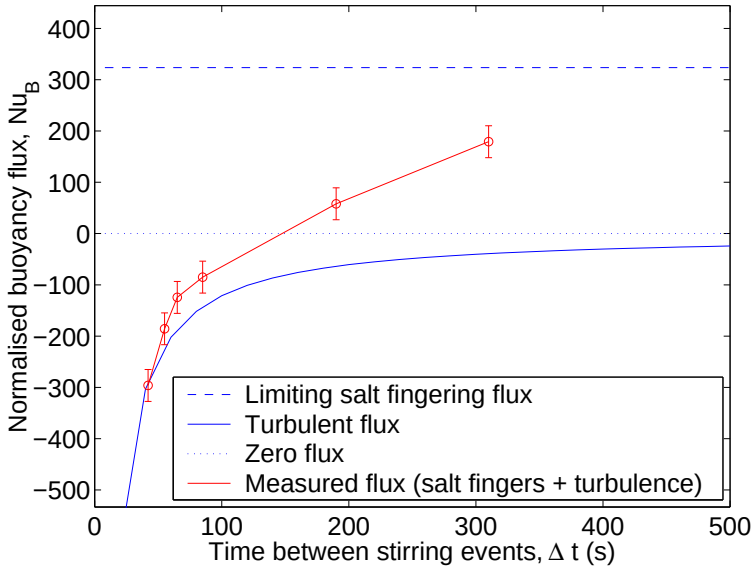

b)

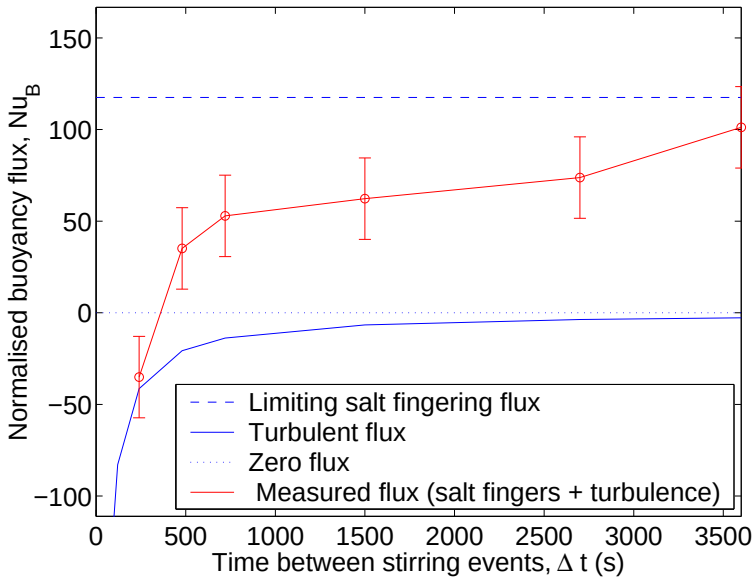

Figure 6.7: Experimentally measured buoyancy fluxes for a) R_ρ = 1.13 and b) R_ρ = 1.25, when a salt fingering gradient was stirred at intervals of Δt. Note the difference in time axis.

a)

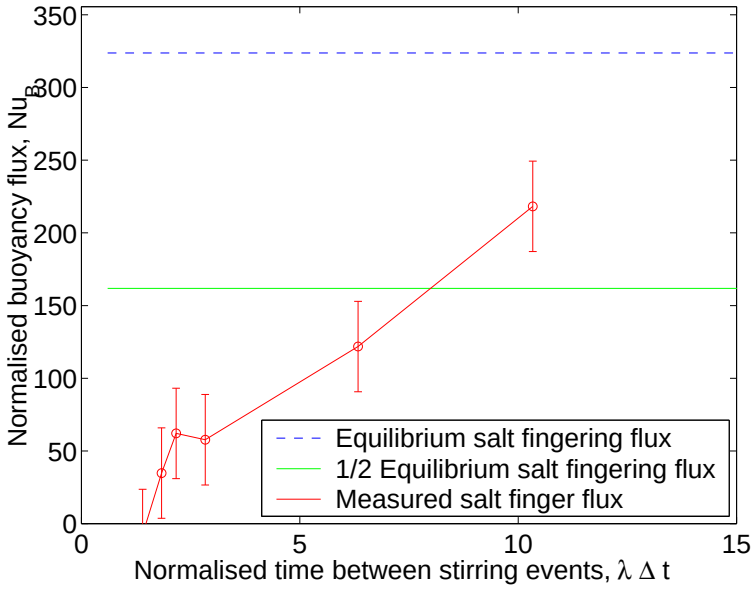

b)

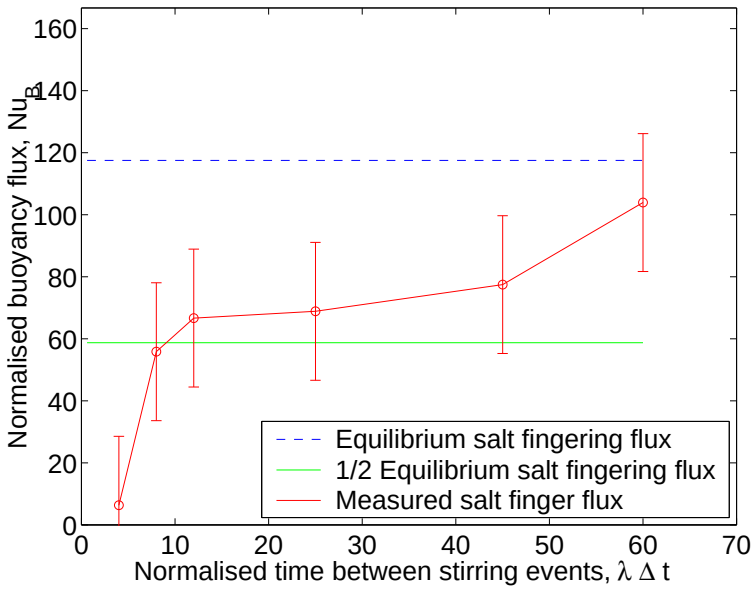

Figure 6.8: Experimentally determined buoyancy fluxes due to the salt fingers for a) R_ρ = 1.13 and b) R_ρ = 1.25. This was found by subtracting the time averaged buoyancy flux of the turbulence (6.4) from the total measured flux shown in figure 6.7. Note the difference in time axis.

6.4 Oceanographic application

We now discuss a parameterization of eddy diffusivities $\overline{K_T}$ and $\overline{K_S}$, due to intermittent turbulence and salt fingers for spatial and temporal scales much larger than those of the intermittent turbulence or salt fingering. We assume that the main effect of turbulence is to reduce salt finger fluxes rather than lead to the overturning convecting layers discussed in chapter 5. The eddy diffusivity $\overline{K_S}$ is then compared with the *ad hoc* parameterization of Schmitt (1981), defined below by (6.14).

The assumptions that we use to derive a time averaged eddy diffusivity of salt $\overline{K_S}$ as a function of $(\Delta t, R_\rho)$ when both salt fingers and intermittent turbulence are present are that:

- A turbulent event totally disrupts salt fingers.
- Salt fingers then grow to reach equilibrium fluxes after 3-7 *e*-folding periods.
- The evolution of the fluxes of T and S grows sharply, with the parameterization defined in (6.2)
- The growth rate λ of salt fingers is a decreasing function of R_ρ and can be described by (1.12). In this calculation we used $g = 980\text{cm s}^{-2}$, $\nu = 1.32\times10^{-2}\text{cm}^2\text{ s}^{-1}$, $\kappa_T = 1.4\times10^{-3}\text{cm}^2\text{ s}^{-1}$ and $\kappa_S = 1.5\times10^{-5}\text{cm}^2\text{ s}^{-1}$.
- The equilibrium diffusivity of salt K_S^* due to salt fingers is a decreasing function of R_ρ and can be described by results from the numerical simulations of Shen (1995) or Merryfield & Grinder (2001)
$$K_S^* = 0.15\frac{1-R_\rho\tau}{R_\rho-\gamma}, \tag{6.12}$$
where we have used $\tau = 0.01$ and $\gamma = 0.6$, typical of heat/salt.
- Turbulence has a well defined intermittency with turbulent events every Δt and a time averaged diffusivity $\overline{K}_{Turb}$.
- Due to the difference in timescales of salt finger growth and turbulence collapse we can add the fluxes of the two time averaged processes, as in (6.6).

We will use observations of oceanic turbulence to determine the time between turbulent events by assuming that turbulent events only persist for one buoyancy period so that

$$\Delta t = \frac{2\pi}{N}\frac{1-I}{I} \tag{6.13}$$

where the intermittence, I, is the proportion of a record over which turbulence is observed.

Measurements by Kunze *et al.* (1990) from a neutrally buoyant float found that there was strong correlation of wave breaking events with the passing of inertial waves which gave $Ri < 1/4$. Turbulence was present in 2% of their record. In other work Alford & Pinkel (2000b) found, using a 9 day continuous record of velocity and density structure collected by R/V Flip, that an average of 3.06% of the water column had actively overturning turbulence. Measurements made by Polzin *et al.* (2001) using a free falling profiler at the NATRE site, indicate that at any time about 5% of the water column was actively overturning due to turbulent events. We therefore discuss intermittencies in the range $1\% < I < 10\%$ to cover the typical range of values of oceanic turbulent intermittence far from topography. With this range (6.13) implies $N\Delta t/2\pi \sim 10 - 100$.

With the assumptions listed above the time averaged diffusivity of salt fingers $\overline{K_{SFinger}}$ is plotted in figures 6.9 and 6.10 using equations (1.12), (6.3), (6.2), (6.12) and (6.13). In figure 6.9 we have fixed the time salt fingers take to equilibrate to 5 *e*-folding periods and change the intermittence from I = 1 % to 10 %. When I = 1% or 2 %, $\overline{K_{SFinger}}$ is little changed from K^*, and there is only a gradual reduction in salt finger diffusivity with increasing R_ρ. When I = 6% or 10%, $\overline{K_{SFinger}}$ is reduced to almost zero at high R_ρ where the *e*-folding timescales are very large. The reduction in salt finger fluxes when $I > 6\%$ and $R_\rho > 2.5$ is mainly due to the rapidly decreasing functional forms of K_S^* and λ with R_ρ. In figure 6.10 we have fixed the intermittence at $I = 6\%$ and show the effect of changing the time salt fingers take to equilibrate. When salt fingers equilibrate in 3 *e*-folding periods, the time averaged diffusivities are closer to K_S^*. When salt fingers take 5 or 7 *e*-folding periods to equilibrate, time averaged diffusivities are reduced below K_S^*, particularly at $R_\rho > 2$.

The important result of the parameterization of the time averaged eddy diffusivity due to salt fingers $\overline{K}_{S\ Finger}$ (shown in figures 6.9 and 6.10) is if turbulence is intermittently present in more than 2% of the water column, only salt fingers with $R_\rho < 2.5$ have growth rates high

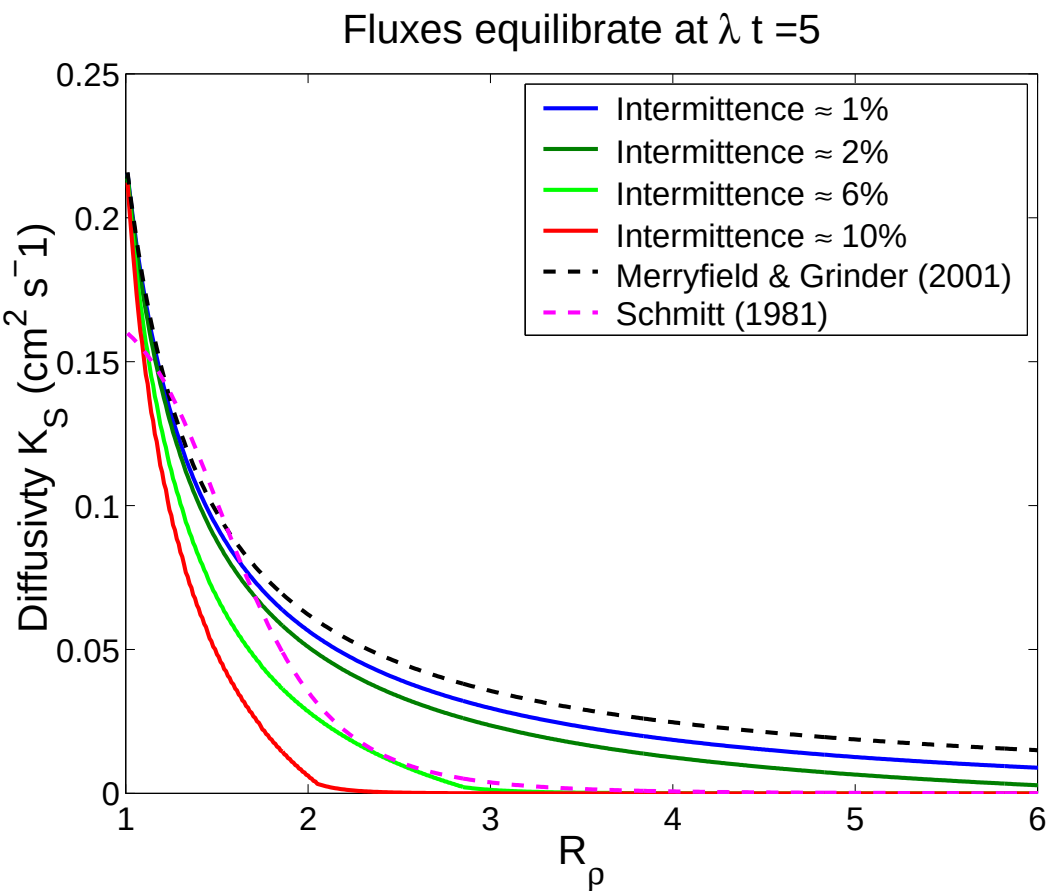

Figure 6.9: A plot of the time averaged diffusivity of salt due to salt fingers for typical oceanographic conditions. Salt finger fluxes take 5 *e*-folding periods to equilibrate. The time between turbulent events Δt varies from 60 to 600 N^{-1} equivalent to intermittencies in the range $1\% < I < 10\%$. Also plotted are the equilibrium diffusivity $K_S^\star$ (defined by 6.12) when there is no turbulence and the *ad hoc* parameterization of salt finger diffusivities, defined by (6.14).

enough to contribute a large equilibrium flux. This strong dependence of the diffusivities upon the time between turbulent events means that if the turbulence in the ocean is characterized by frequent small turbulent events the flux of T and S by salt fingers would be suppressed more dramatically than if there were only a few large but infrequent turbulent events. Changing the number of *e*-folding periods that salt fingers take to reach equilibrium eddy diffusivities $K_S^\star$ is also important in determining $\overline{K}_{S\ Finger}$, but appears to have less effect than changing the intermittency.

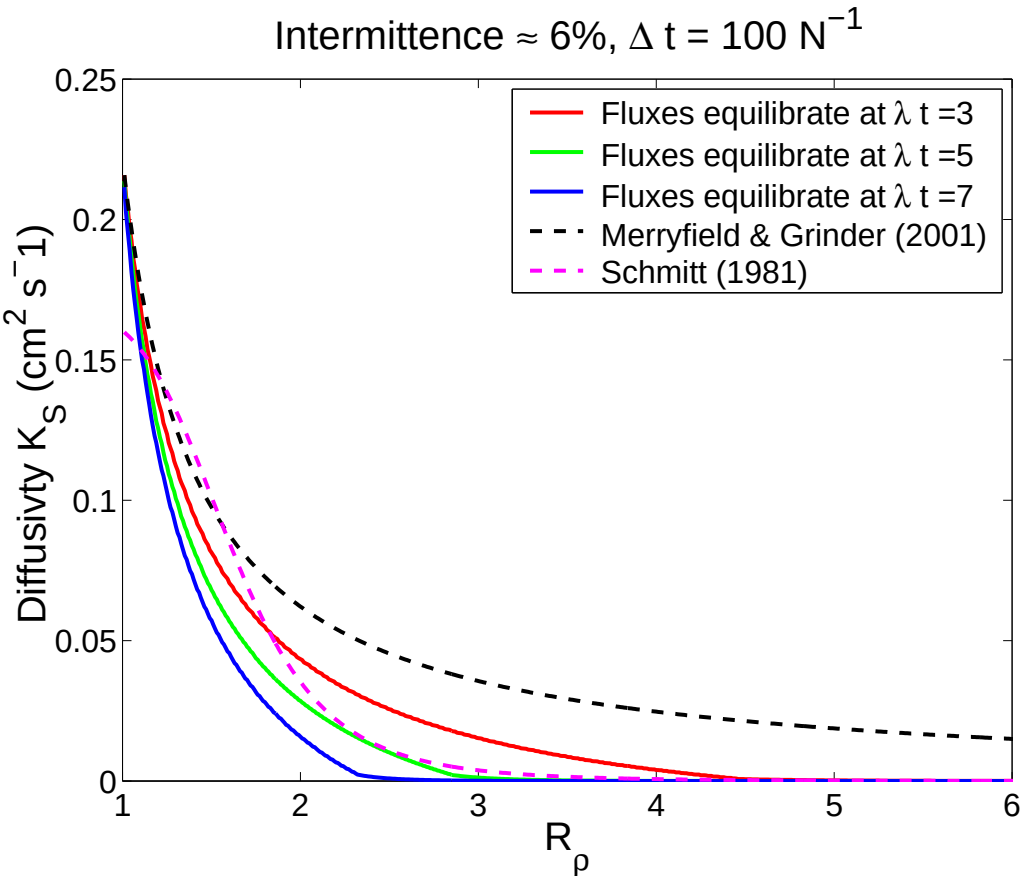

Figure 6.10: A plot of the time averaged diffusivity of salt due to salt fingers for typical oceanographic conditions. Turbulence occurs intermittently with $I \approx 6\%$ ($\Delta t = 100N^{-1}$) and we plot cases where fluxes equilibrate at 3,5 and 7 *e*-folding times. Also plotted are the equilibrium diffusivity $K_S^\star$ (defined by 6.12) when there is no turbulence and the *ad hoc* parameterization of salt finger diffusivities, defined by (6.14)

6.4.1 Previous parameterization of salt finger eddy diffusivities

The *ad hoc* parameterization of salt finger eddy diffusivities of Schmitt (1981) has been used in two recent ocean circulation models of Zhang *et al.* (1998) and Merryfield *et al.* (1999). The functional form of the parameterization for the combined effects of salt fingers and intermittent turbulence was

$$K_S = \frac{K_S^\#}{1+(R_\rho/R_c)^n} + \overline{K}_{Turb} \tag{6.14}$$

$$K_T = \frac{\gamma K_S^{\#}}{R_\rho 1 + \left(R_\rho / R_c\right)^n} + \overline{K}_{Turb}, \tag{6.15}$$

where $K_S^{\#}$ is the maximum salt finger salt diffusivity at low R_ρ, $\overline{K}_{Turb}$ is a constant background turbulent diffusivity and R_c is the critical value of R_ρ at which finger fluxes are assumed to decrease. An exponent of $n = 6$ and $R_c = 1.6$ was used by Zhang *et al.* (1998) and Merryfield *et al.* (1999), so that the salt finger diffusivity rapidly decreases to zero when $R_\rho > R_c$ so the background turbulent values dominate the diffusivity at high R_ρ. Originally a value of $K_S^{\#} = 10$ cm^2 s^{-1} had been used by Schmitt (1981). In light of observations from the C-SALT experiment, a more modest range of values of $K_S^{\#} = 0.5 - 1$ cm^2 s^{-1} was used by Zhang *e*t al. (1998). The study of Merryfield *et al.* (1999) used values in the range $K_S^{\#} = 1 - 10$ cm^2 s^{-1}. The recent observations from the NATRE experiment by St. Laurent & Schmitt (1999) suggest that salt finger diffusivities are in the range of $0.1 - 1$ cm^2 s^{-1} when $1.5 < R_\rho < 2.5$. For comparison with results of Merryfield & Grinder (2001) we assume $K_S^{\#} = 0.17$ cm^2 s^{-1}. The resulting diffusivity due to salt fingers, using (6.14) with $K_{Turb} = 0$, is plotted in figures 6.9 and 6.10. The low values of K_S predicted by (6.14) for $R_\rho \gg 2$ are consistent with the new parameterization in figure 6.9 when salt fingers interact with intermittent turbulence occurring in 6% to 10% of the water column. When turbulence is present in only 1% to 2% of the water column, (6.14) predicts much lower values of the diffusivity at high R_ρ than the equilibrium values of K^* found by Merryfield & Grinder (2001). The important difference between (6.14) and the new parameterization plotted in figures 6.9 and 6.10 is that the degree of the reduction in $\overline{K}_{S\ Finger}$ at large R_ρ varies with Δt and must therefore be estimated for the particular oceanographic site that is to be modeled.

6.4.2 Flux ratio

The effective flux ratio (6.7) can be written in terms of eddy diffusivities as

$$\gamma_{eff} = \frac{\gamma \overline{K}_{S\ Finger} + R_\rho \overline{K}_{Turb}}{\overline{K}_{S\ Finger} + \overline{K}_{Turb}}. \tag{6.16}$$

An example of how γ_{eff} depends upon R_ρ for realistic oceanic values of Δt is plotted in figure 6.11, where we use the time averaged diffusivity of salt fingers $\overline{K_{S Finger}}$ and assume that

salt finger fluxes equilibrate after 5 e folding periods, as plotted in figure 6.10. We use $\gamma = 0.6$ and a constant $\overline{K}_{Turb} = 0.1$ cm^2 s^{-1}, typical of values of turbulent diffusivity in much of the thermocline (Ledwell, 1993). In figure 6.11 there is an 'up gradient' flux of buoyancy, $\gamma_{eff} < 1$, only for $R_\rho < 2$. For the case of constant turbulence ($\Delta t = 0$) salt fingers are totally disrupted so that $\gamma_{eff} = R_\rho$. Increasing $\overline{K}_{Turb}$ would mean that $\gamma_{eff} < 1$ only at $R_\rho \approx 1$. A reduction in $\overline{K}_{Turb}$ would mean that $\gamma_{eff} < R_\rho$ even at large R_ρ.

The form of γ_{eff} plotted in figure 6.11 is qualitatively similar to that used by Walsh & Ruddick (2000) to describe the growth of double diffusive interleaving in the presence of salt fingers and turbulent fluxes. The important difference in (6.16) is that we have assumed γ is constant rather than a decreasing function of R_ρ and, more importantly, we assume that $\overline{K}_{Turb}/K_{S\ finger}$ rapidly increases with R_ρ rather being constant as assumed by Walsh & Ruddick (2000). This difference means that γ_{eff} always increases with R_ρ in our model. Thus the "UV" instability of Walsh & Ruddick (2000), whereby the growth rates of the horizontal intrusions increase without bound for high frequency wave numbers, would not occur when using the salt finger diffusivities plotted in figure 6.10. A negative slope of γ_{eff} only occurs when γ decreases more rapidly with R_ρ than does $\overline{K}_S$ with R_ρ.

6.4.3 Further considerations

There are three effects that we have neglected in the parameterization of $\overline{K_S}$ that may be important in the ocean. The first is that the internal shears caused by the collapse of isolated turbulent events may further reduce the salt finger buoyancy flux by the Linden (1971) mechanism. In the present experiment the turbulence is spatially uniform. Experiments by Thorpe (1982) show that there will be intrusions as the turbulence collapses but that these will not have very large shear associated with them. The consequences of a spatially non-uniform shear were discussed in chapter 3 where we found that density structure can be produced by the salt fingers, resulting due to flux divergences from a strongly spatially varying shear.

If intermittent turbulence occurs in spatially isolated patches then there is the possibility that subsequent salt finger convection may lead to breakdown into a series of convecting layers, by the mechanism discussed in chapter 4. In this case the time averaged fluxes will not be the sum of the time averaged salt finger and turbulent fluxes and the system may converge to a series of sharp interfaces. This may occur in the ocean when $R_\rho \approx 1$. For $R_\rho \gg 1$ we

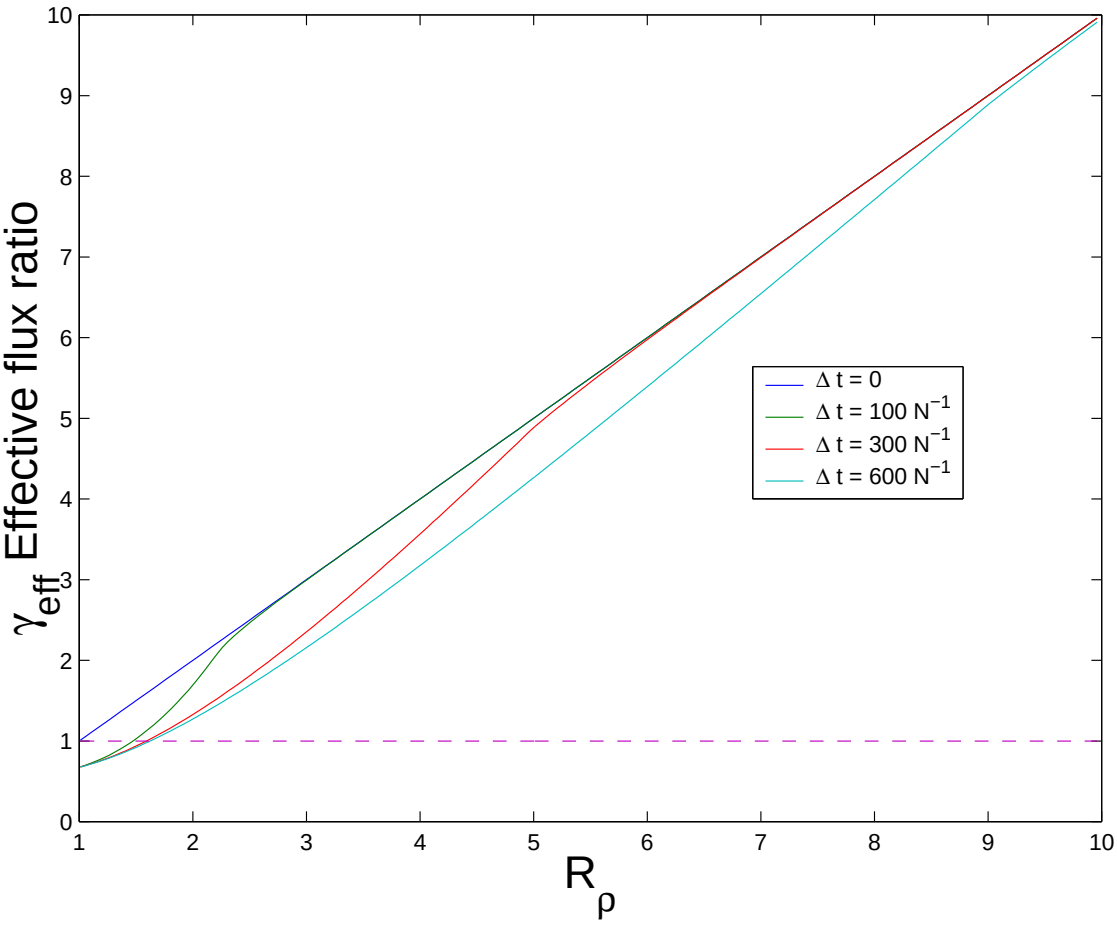

Figure 6.11: The effective flux ratio γ_{eff} that results from salt fingers in intermittent turbulence (6.16), plotted for different values of the time between turbulent events.

showed in chapter 4 that the required patch thicknesses were unlikely to occur under typical oceanographic situations, and we expect the results shown in figures 6.9 and 6.10 to apply.

Another possibility not explored in this experiment and its interpretation, was discussed by Gargett (1987) and in numerical simulations of Merryfield *et al.* (1998), whereby low Reynolds number turbulence may be affected by the molecular diffusivities of the two stratifying components. This is predicted to lead to enhanced transport of T over S and hence the effective flux ratio (6.16) may have $\gamma_{eff} > R_\rho$. This may also be possible in the present experiments when Δt was small and salt fingers were not able to form. In sugar/salt experiments it would be difficult to quantify this effect, as $\kappa_{Salt}/\kappa_{Sugar} = 3$, and at low R_ρ there would only be very small differences in S and T fluxes. For heat/salt, $\kappa_{Heat}/\kappa_{Salt} = 100$ and the effect may be important in oceanographic situations where salt finger fluxes are very small and approach

molecular values (at high R_ρ).

6.5 Conclusions

When gradients are salt-finger favourable and turbulence is intermittent, the total buoyancy flux is strongly dependent upon the time between the turbulent events compared to the growth rate of salt fingers. In the present experiment intermittent turbulence is provided by a comb of vertical rods that are periodically towed through a continuous density gradient favourable to salt fingers. We argue that the total buoyancy flux can be described by assuming 1) that the salt finger fluxes are limited by the time they can grow between turbulent events and 2) that the time averaged flux of salt fingers adds linearly with the time averaged flux of intermittent turbulence. Our experimental results indicate that salt finger buoyancy fluxes reach a limiting flux after 4-10 *e*-folding periods. This is consistent with laboratory observations of Taylor (1991) and numerical observations of Shen (1995) and Merryfield & Grinder (2001).

When we extrapolate our theory of salt fingers in intermittent turbulence to an oceanographic parameterization, we find that the resulting eddy diffusivity of salt $\overline{K}_S$ depends strongly the intermittence of turbulence relative to salt finger growth rates (shown in figure 6.10). When intermittence turbulence is present in more than 6% of the time, our present parameterization has a similar reduction in salt finger fluxes for $R_\rho > 2$ to that of the *ad hoc* parameterization of salt finger fluxes used by Schmitt(1981), Zhang *et al.* (1998) and Merryfield *et al.* (1999) for modeling large scale processes in the ocean. If intermittent turbulence is present less than 2% of the time then $\overline{K}_S$ will not be dramatically reduced below equilibrium values for $R_\rho > 2$ and salt fingers may still contribute significant diapycnal fluxes.

A further implication of time dependent salt fingers interacting with intermittent turbulence is that most of the time the amplitude of salt fingers will be very small; a large amplitude signal only occurs after the fingers have had time to equilibrate. For example, if salt fingers take 5 *e*-folding periods to reach equilibrium fluxes and turbulence occurs every 5.5 *e*-folding periods then only 10 % of a micro-structure record might show strong dissipation due to equilibrium salt fingers even though R_ρ could be strongly finger favourable. Field experiments of Mack & Schoeberlien (1993) found that in a region of the Sargasso sea where there were large regions of low R_ρ, that only a 2% volume average of micro-structure record could be attributed to

salt fingers while an 8% volume average of their micro-structure record could be attributed to turbulence. Similar results were found by St. Laurent &Schmitt (1999) in the NATRE Site. Salt fingers were expected to form as the measured density ratio was in the range $1.5 < R_\rho < 2.5$, but only a 1-10% volume average of their micro-structure record could be attributed to salt fingers while a 5-10% volume average of their micro-structure record could be attributed to turbulence.

Chapter 7

Conclusions

The main results of this thesis are that:

• When distributed and isolated buoyancy fluxes are applied at the same horizontal boundary of a confined fluid, a mixed layer and a stratified region can result. The distributed flux produces a well mixed layer, which reaches a constant depth owing to the vertical advection of the stable density gradient produced by the localized plume buoyancy flux. The depth of the convective layer increases as the distributed flux is increased relative to the plume flux. The whole tank becomes well mixed when the distributed buoyancy flux is approximately equal to the plume buoyancy flux.

• When distributed and isolated buoyancy fluxes are applied from opposite horizontal boundaries of a confined region, a mixed layer and a stratified region again result. The outflow of the plume source is well mixed and, when the distributed flux is small, occupies 1/4 of the tank depth. As the distributed buoyancy flux is increased the strength of the stratification decreases. This results in the depth of the outflow of the plume increasing. The whole tank becomes well mixed when the distributed buoyancy flux is approximately equal to the plume buoyancy flux.

• When surface cooling is applied over a confined volume of fluid consisting of a distinct deep and shallow region, a gravity current forms and flows the shallow region to the deep region. This can then stratify the deep region and force a general upwelling of cold dense fluid. Away from the shallow region the surface cooling leads to a convecting layer above the deeper stratified region. The steady depth of the convecting layer is dependent upon the relative surface areas of the deep and shallow regions. When more than half of the surface area is occupied by a shallow sidearm, then the convecting layer in the deep region occupies less than half of the total depth.

• Observations of winter stratification in the Chaffey reservoir by Dr. Brad Sherman can now be explained in terms of the bathymetry of the reservoir. During the winters of 1995 and 1996 this reservoir had a large shallow sidearm. The surface cooling led to the formation of a gravity current in the sidearm, which was able to stratify the deep region and limit the depth of the surface convecting layer. The observed depth of the surface convecting layer over both winters was in good agreement with the laboratory models presented in this thesis.

• The interaction of salt finger convection and a spatially varying shear can lead to the formation of density fine structure. Tilting of fingers leads to reduced buoyancy fluxes, hence a vertical varying shear leads to buoyancy flux divergences. Where the shear is greatest, the resulting density gradient is weakest and shear instability can occur. This is a new mechanism for the formation of well mixed layers, and the vertical scale is set by the wavelength of the shear rather than a characteristic scale of the salt finger length.

• Salt finger convection in smooth density gradients can break down and drive overturning convection if subjected to localized turbulent mixing. This transition to overturning convection will occur only if; a) the initial R_ρ is near one, b) if the turbulence results in a nearly well-mixed patch and c) if the patch thickness exceeds a critical thickness. Subsequently the thickness of the overturning layer will increase by the entrainment of fluid from the smooth density gradients. The patch thickness h increases in time t, with $h = Ct^{1/2}$. The constant C was shown in chapter 5 to depend on a mixing efficiency of the entrainment as well as on the buoyancy flux of the salt fingers. This is another new mechanism for the formation of a well-mixed layer, and the vertical length scale is set by the size of the isolated mixed patches rather than by the characteristic scales of salt fingers.

• The buoyancy flux due to salt finger convection and intermittent turbulence, when averaged over large times, was shown in chapter 6 to be a strong function of the time between turbulence events relative to the *e*-folding timescale of salt fingers. The salt fingers are disrupted by turbulence but rapidly grow back over several *e*-folding timescales. Thus salt fingers can contribute a large buoyancy flux only if the time between turbulent events is at least 5 to 10 *e*-folding periods. The *e*-folding period is an increasing function of R_ρ (Schmitt, 1979a), so if turbulence occurs more than 5% of the time in the ocean only regions where $R_\rho < 2$ will have significant buoyancy fluxes due to salt fingers. If turbulence occurs infrequently, less than 2% of the time, then salt fingers can contribute significant diapycnal fluxes at $R_\rho > 2$.

7.1 Future work

7.1.1 Circulation and stratification due to cooling in reservoirs

The theoretical and laboratory models of chapters 2 and 3 agreed well with the observations of stratification in Chaffey reservoir. In order to predict whether similar dynamics will apply in other reservoirs during periods of winter cooling, there are two important questions that need to be addressed, namely

- How does the circulation change for different 3-D bathymetries?
- How important is wind-driven mixing in determining the depth of the surface mixed layer?

The first question could be addressed through further laboratory modeling of simple cases, but the geometries that could be studied are numerous and perhaps should be constrained by particular field cases, as discussed below. The second question can addressed theoretically with existing knowledge of wind driven mixed layers and turbulent entrainment, as amplified in § 7.1.1.2.

7.1.1.1 Different bathymetries

In figure 7.1 (a) to (c) we sketch some of the possible bathymetries a reservoir may have. The theory developed in chapter 3 assumed a geometry that had distinct shallow and deep regions, as sketched in 7.1 (a). However the bathymetry of Chaffey reservoir is closer to 7.1 (b) for which the histogram of depths is still bimodal but the sloping regions now occupy a large fraction of the reservoir. A third possibility is that all of the reservoir is a triangular wedge, and no longer has a distinct shallow and deep region, as sketched in 7.1 (c). In this case the resulting circulation is still in the same sense as sketched in figure 3.1, with the important difference that in this case is there is no longer a well mixed surface layer or a strong gravity current. This circulation has been described by Horsch & Stephen (1988). It is not clear when a strong gravity current will fail to form as the bathymetry changes between that shown in figures 7.1 (b) and (c). It would be interesting to perform a series of laboratory experiments to determine where this transition occurs. In a field study a difference might be seen between reservoirs with different bathymetries by making repeated Acoustic Doppler Current Profiler (ADCP) transects in conjunction with moored temperature profilers.

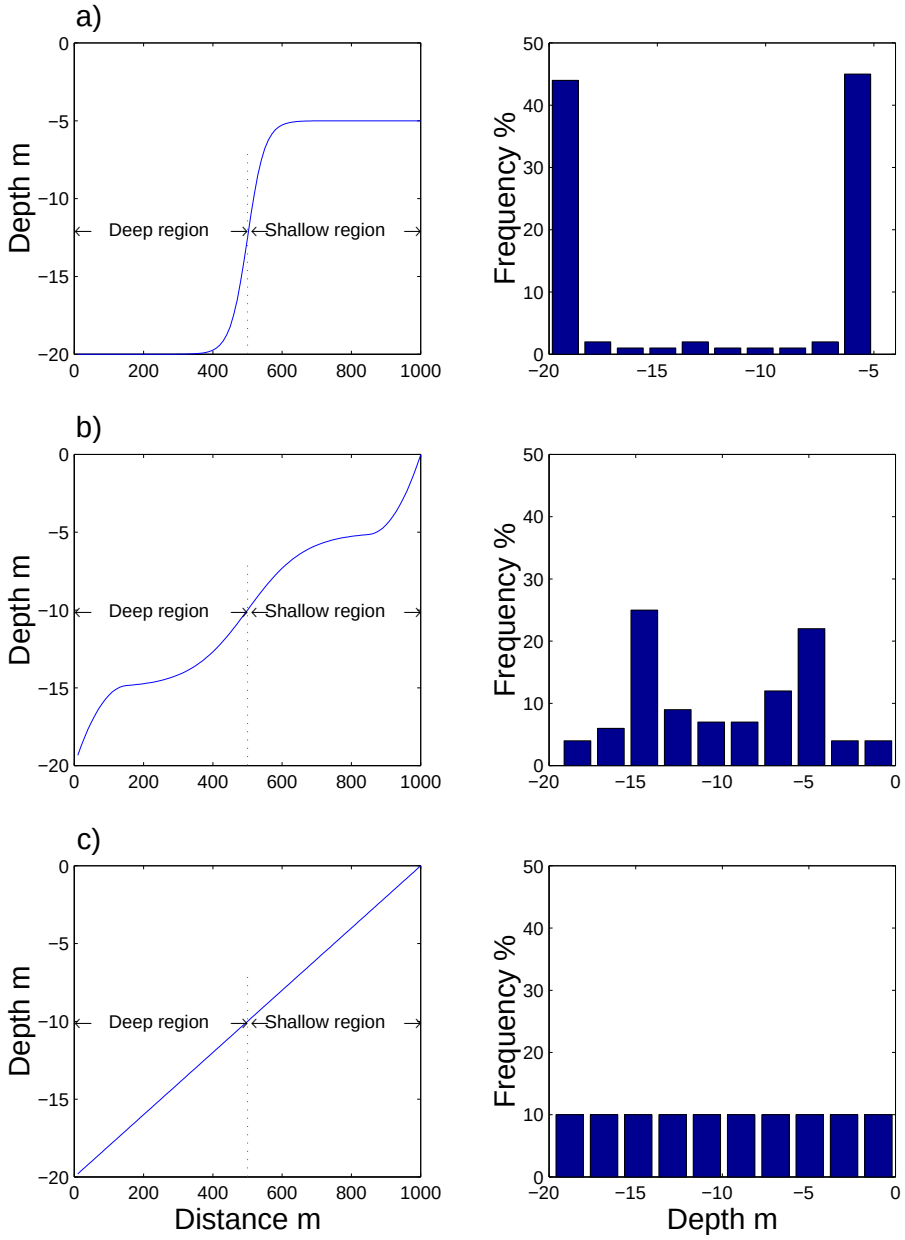

Figure 7.1: A sketch of different possible bathymetries and the associated depth histograms.

7.1.1.2 Wind driven mixing

The theoretical model and laboratory experiments developed in chapters 2 and 3 did not include the effect of wind-driven mixing in determining the steady mixed layer depth. If wind was present in addition to surface cooling, the rate of surface layer deepening would increase. A steady state should occur when the rate at which the gravity current forces upwelling balances the rate at which the mixed layer deepens. The resulting depth of the mixed layer would then be greater than for the case of buoyancy forcing alone.

The effect of additional wind driven mixing could easily be included by replacing equation (2.2) with the one dimensional mixing model of Kraus & Turner (1967). This would result in a more complicated functional form for the steady mixed layer depth than (3.6), with the steady mixed layer depth being a function of mechanical energy available from wind-driven mixing and the magnitude of surface cooling, as well as the depths and areas of the deep and shallow regions.

7.1.2 Salt finger convection

7.1.2.1 Laboratory

All the results from chapters 4, 5 and 6 were either obtained from flow visualization or by taking discrete fluid samples to calculate density profiles. The quantitative results of these experiments could be improved with new equipment and techniques. Some suggestions for future work are:

• Flow visualization - If very fine particles or a fluorescene dye could be seeded into a salt finger field then the velocities of the fingers could be determined. Chapters 4, 5 and 6 all made assumptions about the salt finger velocities that could be checked only by observations from the shadowgraph. The use of micro-scale particle imaging velocimetry would allow the predicted scaling of finger velocities (4.20) to be quantified in greater detail.

• A probe to measure refractive index or optical rotation - Advances in laser and optic-fiber technology mean that a traversing probe could be developed of similar dimensions to commercially available conductivity and thermistor probes. If profiles of optical rotation, refractive index and conductivity could be made, then using the polynomials of Ruddick & Shirtcliffe (1979), profiles of sugar and salt could easily be determined for laboratory experiments.

• Heat/salt experiments - With the exception of the work by Taylor (1991, 1993) there have been very few experiments using "crossed " heat/salt gradients due to the inherent technical difficulties of insulating a tank. Future experiments might try to test the numerical results of Merryfield & Grinder (2001). It would also be interesting to repeat the shearing and intermittent turbulence experiments of chapters 4, 5 and 6 using heat/salt and see whether any new behaviour emerges.

7.1.2.2 Numerical simulations

Direct numerical simulations of salt fingers could be used to further test and quantify some of the predictions of chapter 4, 5 and 6. Some suggestions for future work are:

• Model the effect of an imposed velocity gradient upon equilibrium salt finger fluxes. The results could be used to quantify how fluxes are reduced by shear and test whether fluxes decrease like $\cos\theta$ at large θ.

• Investigate the timescale for salt finger fluxes to equilibrate after being disrupted by a turbulent event. This could be done by changing the magnitude and spectral signature (changing the initial "white noise") of perturbations that are used to seed the T, S and vorticity fields. These different initial conditions could mimic those present after a turbulent event.

• Determine when salt finger fluxes scale with $\Delta S^{4/3}$ (where ΔS is an imposed S difference over a distance d) and when the fluxes scale linearly with S_z. This could be done in a series of numerical experiments by progressively increasing the size of the computational domain d for a constant ΔS, determining when F_S decreases like $\Delta S/d$.

7.1.2.3 Field work

The interaction of salt fingers with shear (in chapter 4) and with isolated turbulent patches (in chapter 5), both resulted in layered density structure. There are many regions of the ocean where R_ρ is favourable to salt finger convection and any salt fingers that form are likely do so in the presence of shear and turbulence. The fine-scale structure predicted in chapters 4 and 5 would be observable in a vertical cast using a CTD probe and the use of a micro-structure probe would allow the detection of any salt fingers present. However, it may be difficult to distinguish any observed fine-scale structure from other processes such as frontal intrusions.

The best way to determine if the processes described in chapters 4 and 5 are occurring in the ocean would be to take a "slice" through a region where R_ρ is close to one. Such a field experiment was performed by Mack (1989), who towed a vertical chain of conductivity probes and thermistors through a region of the Sargasso sea where $1 < R_\rho < 3$. If an ADCP is used in conjunction with the vertical chain, then regions of high shear or turbulence interacting with salt fingers might be identified. Subsequent transects might then look at the time evolution of the fine-scale structure and determine whether the density fine-structure takes the same vertical scale and is coherent with the horizontal shears.

In chapter 6 it was shown that the time-averaged buoyancy flux due to salt fingers depended sensitively on the time between turbulent events. Observations of turbulence in the ocean are usually reported in terms of the percentage of a record that contained turbulence. It would be interesting to re-examine such records and determine the average time between turbulent events. If intermittent turbulence is isolated in both space and time then the theory used in equation (6.13) will be adequate. The same intermittence of turbulence could also occur if turbulence occurs in isolated regions but has a continued input of mechanical energy. This would result in very different times between turbulent events, so that the time averaged buoyancy flux would be different to that described in chapter 6. Hopefully future field work will be able to determine the form of turbulence in the large regions of the ocean where $1 < R_\rho < 2$.

Bibliography

ADRIAN, R. J., FERREIRA, R. T. D. S. & BOBERG, T. 1986 Turbulent thermal convection in wide horizontal fluid layers. *Exp. Fluids*, **4**, 121-141.

ALFORD, A. & PINKEL, R. 2000a Observations of overturning in the thermocline: the context of ocean mixing. *J. Phys. Oceanogr.*, **30**, 805-832.

ALFORD, A. & PINKEL, R. 2000b Patterns of turbulent and double-diffusive phenomena: observations from a rapid-profiling micro-conductivity probe. *J. Phys. Oceanogr.*, **30**, 833-854.

ALTMAN, D. B. & GARGETT, A. E. 1987 Differential property transport due to incomplete mixing in a stratified flow, in paper presented at the Third Int. Symp. on Stratified Flows, Calif. Inst. of Technol., Pasadena, USA.

ARMI, L. 1986 The hydraulics of two flowing layers of different densities. *J. Fluid. Mech.*, **163** 27-58.

ARNOLD T. N. & OLDHAM, C. E. 1997 Trace-element contamination of a shallow wetland. *Western Australia. Mar. Freshwater Res.*, **48**, 531-539.

BAINES, W. D. & TURNER, J. S. 1969 Turbulent buoyant convection from a source in a confined region. *J. Fluid. Mech.*, **37**, 51-80.

BARNETT, S. 1991 The dynamics of buoyant releases in confined spaces. PhD Thesis, Cambridge University.

BLOOMFIELD, L. J. & KERR, R. C. 1998 Turbulent fountains in a stratified fluid. *J. Fluid. Mech.*, **358**, 335-356.

DEARDORF, J. W., WILLIS, G. E. & STOCKTOM, B. H. 1980 Laboratory studies of the entrainment zone of a convectively mixed layer. *J. Fluid. Mech.*, **100**, 41-64.

DENTON, R. A. & WOOD, I. R. 1981 Penetrative convection at low Peclet number. *J. Fluid. Mech.*, **113**, 1-21.

DE SILVA, I. P. D. & FERNANDO, H. J. S. 1992 Some aspects of mixing in a stratified turbulent patch. *J. Fluid. Mech.,* **240**, 601-625.

ELLIOTT, A. J., HOWE, M. R. & TAIT, R. I. 1974 The lateral coherence of a system of thermohaline layers in the deep ocean. *Deep-Sea Res.,* **21**, 95-107.

ELLISON, T. H., & TURNER, J. S. 1959 Turbulent Entrainment in stratified flows. *J. Fluid. Mech*., **6**, 423-448.

FEARN, D. R., LOPER, P. E. & ROBERTS,P. 1981 Structure of the Earth's inner core. *Nature,* **292**, 232-233.

FEARN, D. R. & LOPER, P. E. 1981 Compositional convection and stratification of the Earth's core. *Nature*, **289**, 393-394.

FER, I., LEMMIN, U. & THORPE, S. A. 2000 The winter cold slope boundary layer, in paper presented at the Fifth Int. Symp. on Stratified Flows, University of British Columbia, Vancouver, Canada.

FIGUEROA, H. A. 1996 World ocean density ratios. *J. Phys. Oceanogr.,* **26**, 267-275.

FINNIGAN, T. D. & IVEY, G. N. 1999 Sub-maximal exchange between a convectively forced basin and a large reservoir. *J. Fluid. Mech.,* **378**, 357-378.

FINNIGAN, T. D. & IVEY, G. N. 2000 Convectively driven exchange flow in a stratified sill-enclosed basin. *J. Fluid. Mech.,* **418**, 313-338.

FISCHER, H. B., LIST, E. J., KOH, R. C. Y., IMBERGER, J. & BROOKS, N. H. 1979 *Mixing in Inland and Coastal Waters,* Academic Press.

GARGETT, A. 1987 Reynolds number effects on turbulence in the presence of stable stratification *Small-scale turbulence and mixing in the ocean*, Elsevier Oceanogr. series.

GARGETT, A. E. & SCHMITT R. W. 1982 Observations of salt fingers in the central waters of the eastern North Pacific. *J. Geophys. Res.*, **87**, 8017-8029.

GARGETT, A. E. & HOLLOWAY, G. 1992 Sensitivity of the GFDL ocean model to different diffusivities for heat and salt. *J. Phys. Oceanogr.,* **22**, 1158-1177.

GARGETT, A. E. & FERRON, G. 1996 The effects of differential vertical diffusion of T and S in a box model of thermohaline circulation. *J. Mar. Res.,* **54**, 827-866.

GREGG, M. C. 1987 Diapycnal mixing in the thermocline: A review. *J. Geophys. Res., 92*, 5249-5286.

GRIFFITHS, R. W. & RUDDICK, B. R. 1980 Accurate fluxes across a salt-sugar finger interface deduced from direct density measurements. *J. Fluid. Mech., 99*, 85-95.

GRIMM. T. & MAXWORTHY, T. 1999 Buoyancy-driven mean flow in a long channel with a hydraulically constrained exit condition. *J. Fluid. Mech.,* **398**, 155-180.

HOLFORD,J. M. & LINDEN, P. F. 1999 Turbulent mixing in a stratified fluid. *Dyn. Atmos. Ocean.,* **30**, 173-198.

HOLYER, J. Y. 1984 The stability of long, steady two-dimensional salt fingers. *J. Fluid. Mech.,* **147**, 169-185.

HOLYER, J. Y. 1985 The stability of long steady three-dimensional salt fingers to long wavelength perturbations. *J. Fluid. Mech.,* **156**, 495-503.

HORSCH G. M. & STEFAN, H. G. 1988 Convective circulation in littoral water due to surface cooling. *J. Limnol. Oceanogr.,* **33**, 1068-1083.

HOWARD, L. N. & VERONIS, G. 1987 The salt-finger zone. *J. Fluid. Mech.,* **183**,1-23.

HUGHES, G. O. 1996 Some aspects of mixing a stratified patch. PhD Thesis, Cambridge University.

ITSWEIRE. E. C HELLAND,K. N & VAN ATTA,C. W. 1986 The evolution of grid-generated turbulence in a stably stratified fluid. *J. Fluid. Mech.,* **162**, 299-338.

IVEY, G. & IMBERGER, J. 1990 On the nature of turbulence in a stratified fluid. Part 1: The energetics of mixing. *J. Phys. Oceanogr.* **21**, 650-658.

JAMES W. F. & BARKO, J. W. 1991 Estimation of phosphorus exchange between littoral and pelagic zones during night time convective circulation. *J. Limnol. Oceanogr.,* **36**, 179-187.

KAYE, G. W. C. & LABY, T. H. 1973 *Table of Phys. and Chemical Constants*, 14th Edn. Longman.

KILLWORTH, P. D. & TURNER, J. S. 1982 Plumes with time-varying buoyancy in a confined region. *Geophys. Astrophys. Fluid Dyn.,* **20**, 265-291.

KRAUS, E. B. & TURNER, J. S. 1967 A one-dimensional of the seasonal thermocline. II The general theory and its consequences. *Tellus,* **19** 98-106.

KUNZE, E. 1987 Limits on growing, finite length salt fingers: A Richardson number constraint. *J. Mar. Res., 45*, 533-556.

KUNZE, E. 1990 The evolution of salt fingers in inertial wave shear. *J. Mar. Res.,* **48**, 471-504.

KUNZE, E. 1994 A proposed flux constraint for salt fingers in shear. *J. Mar. Res.,* **52**, 999-1016.

KUNZE, E., WILLIAMS III, A. J. & SCHMITT, R. W. 1987 Optical micro structure in the thermohaline staircase east of Barbados. *Deep-Sea Res.,* **34**, 1697-1704.

KUNZE, E., WILLIAMS III, A. J. & BRISCOE, M. G. 1990 Observations of shear and vertical stability from a neutrally-buoyant float. *J. Geophys. Res.,* **95**, 18127-18142.

LAMBERT, R. B. & DEMENKOW, J. W. 1972 On the vertical transport due to fingers in double diffusive convection. *J. Fluid. Mech.,* **54**, 627-640.

LAMBERT, R. B. & STURGES, W. 1977 A thermohaline staircase and vertical mixing in the thermocline. *Deep-Sea Res.,* **24**, 211-222.

LEDWELL, J. R. WATSON, A. J. & LAW, C. S. 1993 Evidence of slow mixing across the pycnocline from an open-ocean tracer release experiment. *Nature,* **364**, 701-703.

LEVITUS, S. 1987 *Climatological atlas of the world ocean.* Rockville. Md. NOAA.

LIDE, D. R. 1985 *CRC Handbook of chemistry and Physics* 72nd Edn, CRC press.

LINDEN, P. F. 1971 Salt fingers in the presence of grid-generated turbulence. *J. Fluid. Mech.,* **49**, 611-624.

LINDEN, P. F. 1974 Salt fingers in a steady shear flow. *Geophys. Fluid Dyn.,* **6**, 1-27.

LINDEN, P. F. 1976 The formation and destruction of fine structure by double-diffusive processes. *Deep-Sea Res.,* **23**, 895-908.

LINDEN, P. F. 1978 The formation of banded salt finger structure. *J. Geophys. Res.,* **83**, 2902-2912.

LINDEN, P. F. 1979 Mixing in stratified Fluids. *Geophys. Astrophys. Fluid Dyn.,* **13**, 3-30.

LINDEN, P. F. 1980 Mixing across a density interface produced by grid turbulence. *J. Fluid. Mech.,* **100**, 691-703.

LIU, W. T., KATSAROS, K. B. & BUSINGER, J. A. 1979 Bulk parameterization of the air-sea exchange of heat and water vapor including the molecular constraints at the interface. *J. Atmos. Sci.,* **36**, 1722-1735.

MACK, S. A. 1989 Towed-chain measurements of ocean micro structure. *J. Phys. Oceanogr.,* **19**, 1108-1129.

MACK, S. A. & SCHOEBERLIEN, H. C. 1993. Discriminating salt fingering from turbulence-induced micro structure: analysis of towed temperature-conductivity chain data. *J. Phys. Oceanogr.,* **23**, 2073-106.

MAGNELL, B. 1976 Salt fingers observed in the Mediterranean outflow region (34 degrees N, 11 degrees W) using a towed sensor. *J. Phys. Oceanogr.,* **6**, 511-523.

MANINS, P. C. 1979 Turbulent buoyant convection from a source in a confined region. *J. Fluid. Mech.,* **91**, 765-781.

MANINS, P. C. & TURNER, J. S. 1977 The relation between the flux ratio and energy ratio in a convectively mixed layer. *Q. J. R. Met. Soc.,* **104**, 39-44.

MARMORINO, G. O. 1990 "Turbulent mixing" in a salt-finger staircase. *J. Geophys. Res.,* **95**, 12,983-12,994.

MAXWORTHY, T. 1997 A frictionally and hydraulically constrained model of the convectively driven mean flow in partially enclosed seas. *Deep-Sea Res.,* **44**, 1339-1354.

MCDOUGALL, T. 1983 Double diffusive plumes. *J. Fluid. Mech.,* **133**, 321-343.

MCDOUGALL, T. J. & RUDDICK, B. R. 1992 The use of ocean micro structure to quantify both turbulent mixing and salt fingering. *Deep-Sea Res.,* **39**, 1931-1952.

MCDOUGALL, T. J. & TAYLOR, J. R. 1984 Flux measurements across a finger interface at low values of the stability ratio. *J. Mar. Res.,* **42**, 1-14.

MCEWAN, A. D. 1971 Degeneration of resonantly-excited standing internal gravity waves. *J. Fluid. Mech.,* **50**, 431-448.

MERRYFIELD, W. J. 2000 Origin of thermohaline staircases. *J. Phys. Oceanogr.,* **30**, 1046-1068.

MERRYFIELD, W. J., HOLLOWAY, G. & GARGETT, A. 1998 Differential transport of heat and salt by weak stratified turbulence. *Geophys. Res. Lett.,* **25**, 2773-2776.

MERRYFIELD, W. J., HOLLOWAY, G. & GARGETT, A. 1999. A global ocean model with double-diffusive mixing. *J. Phys. Oceanogr.,* **29**, 1124-1142.

MERRYFIELD, W. J. & GRINDER,M. 2001 Salt fingering fluxes from numerical simulations. *J. Phys. Oceanogr.,* (in press).

MONISMITH, S. G., IMBERGER, J. & MORISON, M. L. 1990 Convective motions in the sidearm of a small reservoir. *J. Limnol. Oceanogr.* **35**, 1676-1702.

MOLCARD, R. & TAIT, R. I. 1977 The steady state of the step structure in the Tyrrhenian Sea. in *A Voyage of Discovery*, George Deacon 70th Anniversary Volume, M. V. Angel (Ed.), Suppl. to. *Deep-Sea Res.,* **38**, 221-233.

OAKEY, N. 1985 Statistics of mixing parameters in the upper ocean during JASIN Phase 2. *J. Phys. Oceanogr.,* **15**, 1662-1675.

OSBORN, T. & COX, C. S. 1972 Oceanic fine structure. *Geophys. Fluid Dyn.,* **3**, 321-345.

PARK, Y., WHITEHEAD, J. A. & GNANADESKIAN, A. 1994 Turbulent mixing in stratified fluids: layer formation and energetics. *J. Fluid. Mech.,* **279**, 279-311.

PIERCE, D. W. & RHINES, P. B. 1996 Convective building of a pycnocline: Laboratory experiments *J. Phys. Oceanogr.,* **26**, 176-190.

POLZIN, K. L., KUNZE, E., TOOLE, J. M. & SCHMITT, R. W. 2001 The partition of fine-scale energy into internal waves and geostrophic motions. *J. Phys. Oceanogr.,* (under review).

RADKO, T. & STERN, M. E. 1999 Salt fingers in three dimensions. *J. Mar. Res.,* **57**, 471-502.

RADKO, T. & STERN, M. E. 2000 Finite amplitude salt fingers in a vertically bounded layer. *J. Fluid. Mech.,* **425**, 133-160.

RUDDICK, B. 1992 Intrusive mixing in a Mediterranean salt lens - intrusion slopes and dynamic mechanisms. *J. Phys. Oceanogr.*, **22**, 1274-1285.

RUDDICK, B. R., MCDOUGALL, T. J. & TURNER, J. S. 1979 The formation of layers in a uniformly stirred density gradient. *Deep-Sea Res.,* **36**, 903-913.

RUDDICK, B. R. & SHIRTCLIFFE, T. G. L. 1979 Data for double diffusers: Phys. properties of aqueous salt-sugar solutions. *Deep-Sea Res.,* **26**, 775-787.

RUDDICK, B. R. & TURNER, J. S. 1979 The vertical length scale of double-diffusive intrusions. *Deep-Sea Res.,* **26**, 903-913.

RUDDICK, B. & WALSH, D. 1995 Observations of the density perturbations which drive thermohaline intrusions. in *Double Diffusive Convection, Geophys. Monogr. Ser.*, vol 94, edited by A. Brandt and H. J. S. Fernando, pp. 329-334, A. G. U., Washington, D. C.

RUDDICK, B. R., WALSH, D. & OAKEY, N. 1998 Variations in apparent mixing efficiency in the North Atlantic central water. *J. Phys. Oceanogr.,* **27**, 2589-2605.

ST. LAURENT, L. & SCHMITT, R. W. 1999 The contribution of salt fingers to vertical mixing in the north atlantic tracer release experiment. *J. Phys. Oceanogr.,* **29**, 1404-1424.

SCHMITT, R. W. 1979a The growth rate of super-critical salt fingers. *Deep-Sea Res.,* **26**, 23-40.

SCHMITT, R. W. 1979b Flux measurements on salt fingers at an interface. *J. Mar. Res.,* **37**, 419-436.

SCHMITT, R. W. 1981 Form of temperature-salinity relationship in the central water: evidence for double-diffusive mixing. *J. Phys. Oceanogr.,* **11**, 1015-1026.

SCHMITT, R. W. 1990 On the density ratio balance in the Central Water. *J. Phys. Oceanogr.,* **20**, 900-906.

SCHMITT, R. W. 1994 Double Diffusion in Oceanogr. *Ann. Rev. Fluid. Mech.* **26**, 255-285.

SCHMITT, R. W. & D. L. EVANS, 1978 An estimate of the vertical mixing due to salt fingers based on observations in the North Atlantic Central Water. *J. Geophys. Res.* **83**, 2913-2919.

SCHMITT, R. W., PERKINS,H., BOYD, J. D. & STALCUP, M. C. 1987 C-SALT: an investigation of the thermohaline staircase in the western tropical North Atlantic. *Deep-Sea Res.,* **34**, 1697-1704.

SHEN, C. Y. 1995 Equilibrium salt-fingering. *Phys. Fluids A,* **1**, 829-844.

SHERMAN, B. S., FORD, P., HATTON, P., WHITTINGTON, J., GREEN, D., BALDWIN, D., OLIVER, R., VANBERKEL, J., BECKETT, R., GREY, L. & MAHER, W. 2000 The Chaffey Dam Story. Final report for Cooperative Research Centre for Freshwater Ecology projects B. 202 and B. 203. Canberra.

STERN, M. E. 1969 Collective instability of salt fingers. *J. Fluid. Mech.,* **35**, 209-218.

STERN, M. E. 1975 *Ocean Circulation Physics*, Academic Press.

STERN, M. E. & RADKO, T. 1998 The salt finger amplitude in unbounded. *T-S* gradient layers. *J. Mar. Res.,* **56**, 157-196.

STERN, M. E. & TURNER, J. S. 1969 Salt fingers and convecting layers. *Deep-Sea Res.,* **16**, 497-511.

STOMMEL, H. M., ARONS, A. B. & BLANCHARD, D. 1956 An oceanographic curiosity: the perpetual salt fountain. *Deep-Sea Res.,* **3**, 152-153.

STURMAN, J. J. & IVEY, G. N. 1998 Unsteady convective exchange flows in cavities. *J. Fluid. Mech.,* **368**, 127-153.

STURMAN, J. J., OLDHAM, C. E. & IVEY, G. N. 1999 Steady convective exchange flows down slopes. *Aquatic Sciences*, **61**, 1-19.

TAYLOR, J. 1991 Laboratory experiments on the formation of salt fingers after the decay of turbulence. *J. Geophys. Res.,* **96**, 12497-12510.

TAYLOR, J. 1993 Anisotropy of salt fingers. *J. Phys. Oceanogr.,* **23**, 554-565.

TAYLOR, J. & BUCENS, P. 1989 Laboratory experiments on the structure of salt fingers. *Deep-Sea Res.,* **36**, 1675-1704.

TAYLOR, J. & VERONIS, G. 1986 Experiments on salt fingers in a Hele Shaw cell. *Science, 231*, 39-41.

THORPE, J. S. 1982 On the layers produced by rapidly oscillating vertical grid in a uniformly stratified fluid. *J. Fluid. Mech.,* **124**, 391-409.

TURNER, J. S. 1967 Salt fingers across a density interface. *Deep-Sea Res.,* **14**, 599-611.

TURNER, J. S. 1968 The behaviour of a stable salinity gradient heated from below. *J. Fluid. Mech.* **33**, 183-200.

TURNER, J.S. 1973 *Buoyancy Effects in Fluids*. Cambridge University Press.

TURNER, J. S. 1986 Turbulent Entrainment: the development of the entrainment assumption and its application to geophysical flows. *J. Fluid. Mech.,* **173**, 431-471.

TURNER, J. S. & CHEN, C. F. 1974 Two-dimensional effects in double diffusive convection. *J. Fluid. Mech., 63*, 577-592.

VERONIS, G. 1987 The role of the buoyancy layer in determining the structure of salt fingers. *J. Fluid. Mech.,* **180**, 327-342.

WALSH, D. & RUDDICK, B. R. 1995 Double-diffusive interleaving: the influence of non-constant diffusivities. *J. Phys. Oceanogr.,* **25**, 348-358.

WALSH, D. & RUDDICK, B. 1995 An investigation of Kunze's salt finger flux laws: Are they stable? in. *Double Diffusive Convection, Geophys. Monogr. Ser.*, vol 94, edited by A. Brandt and H. J. S. Fernando, pp. 321-328, A. G. U., Washington, D. C.

WALSH, D. & RUDDICK, B. R. 1998 Nonlinear evolution of thermohaline intrusions. *J. Phys. Oceanogr.*, **28**, 1043-1070.

WALSH, D. & RUDDICK, B. 2000 Double-diffusive interleaving in the presence of turbulence-the effect of a non-constant flux ratio. *J. Phys. Oceanogr.*, **30**, 2231-2245.

WELLS, M. G., GRIFFITHS, R. W. & TURNER, J. S. 1999 Competition between distributed and localized buoyancy fluxes in a confined region. *J. Fluid. Mech.,* **391**, 319-336.

WELLS, M. G., GRIFFITHS, R. W. & TURNER, J. S. 2001 Generation of density fine structure by salt fingers in a spatially periodic shear. *J. Geophys. Res.*, (in press)

WELLS, M. G. & SHERMAN 2001 Stratification produced by surface cooling in lakes with significant shallow regions *J. Limnol. Oceanogr.*, (under review).

WHALER, K. A. 1980 Does the whole of the Earth's outer core convect? *Nature,* **287**, 528-530.

WINTERS, K. B., LOMBARD, P. N., RILEY, J. J. & D'ASARO, E. A. 1995 Available potential energy and mixing in density stratified fluids. *J. Fluid. Mech.,* **289**, 115-128.

WILLIAMS, A. J. 1975 Images of ocean micro structure. *Deep-Sea Res.,* **22**, 811-829.

WONG, A. B. D., GRIFFITHS, R. W. & HUGHES, G. O. 2001 Shear layers driven by turbulent plumes. *J. Fluid. Mech.,* (in press).

WORSTER, M. G. & HUPPERT, H. E 1983 Time dependent density profiles in a filling box. *J. Fluid. Mech.,* **132**, 457-466.

ZHANG, J., SCHMITT, R. W. & HUANG, R. X. 1998 Sensitivity of the GFDL Modular Ocean Model to the parameterization of double-diffusive processes. *J. Phys. Oceanogr.,* **28,** 589-605.

ZHURBAS, V. M., KUZIMINA, N. P. & KULSHA, Y. 1987 Step like stratification of the oceanic thermocline from transformation associated with thermohaline salt finger intrusions (numerical experiment). *Oceanology,* **27**, 277-281.